ABSTRACT

Title of dissertation: BOSE EINSTEIN CONDENSATES IN DYNAMICALLY CONTROLLED OPTICAL LATTICES

Zachary Schutz Smith
Doctor of Philosophy, 2019

Dissertation directed by: Professor Steven L. Rolston
Joint Quantum Institute (JQI),
National Institute of Standards and Technology (NIST),
Department of Physics, University of Maryland

Ultracold atomic gases are often used as quantum simulators, where the ability to precisely control and modulate the potential landscape allows many model Hamiltonians to be realized. Recently, dynamic control over these potentials has been leveraged to extend the kinds of systems that can be explored. Our lab has constructed an optical lattice generator capable of dynamically altering the spacing, phase, and amplitude of an optical lattice at RF timescales. The rapid timescales allows the construction of a time-averaged disordered potential from individual flashes of optical lattice, producing layered system exhibiting a Griffiths phase. A future experiment where the optical lattice is periodically expanded and contracted is proposed, and a numerical treatment is presented suggesting interesting structure in the tunneling dynamics.

BOSE EINSTEIN CONDENSATES IN DYNAMICALLY CONTROLLED OPTICAL LATTICES

by

Zachary Schutz Smith

Dissertation submitted to the Faculty of the Graduate School of the
University of Maryland, College Park in partial fulfillment
of the requirements for the degree of
Doctor of Philosophy
2019

Advisory Committee:

Professor Steven L. Rolston: *Advisor, Chair*
Professor Mario Dagenais: *Dean's Representative*
Professor Gretchen Campbell
Professor Trey Porto
Professor Norbert Linke

Preface

Git was used for version control throughout the preparation of this thesis. For the purposes of identifying this version in relation to any other, the following information is provided. This document was produced from LaTeX source corresponding to commit v2.0.2, which was checked in at 2019-08-21 16:43:55 -0400. This commit's full hash is d9949906e8700229784d9de942323ddaf8932604.

Dedication

To my darling wife:

These pages are my second-greatest accomplishment in graduate school. The first, by far, was marrying you.

Acknowledgments

I may have spent the last 10 years in graduate school, but the journey began long before then. I had many fantastic science teachers during my secondary education, including Mr. Terrell, Mr. Mohler, and Dr. Crawford. In particular my high school physics teacher Shane Foglesong encouraged me to pursue physics going forward.

The entire physics and astronomy department at Calvin College provided a really great environment to learn and grow in. The whole faculty showed true commitment to helping the students along, and I wouldn't be half the physicist I am without their help. I was privileged enough to do research there throughout my time, working with Prof. Haan for four years. I learned a lot about how research is done and what passion for learning looked like from him. I also got to do research with Prof. Walhout, with whom I had my first forays into atomic physics, and learned the nitty-gritty of turning data into Data. The physics majors there banded together at every opportunity to get everyone up to speed. Without their help, I'd still be an undergrad.

Graduate students don't stand alone, and they certainly don't get results alone. When I joined the lab they were just wrapping up a project, and the journey from that point to this work was filled with many twists and turns. My fellow graduate student Matt Reed was my partner through all of this, from diagnosing vacuum spiders to aligning and naming the HiBAL. Aftaab Dewan joined in part way through, and he'll be the one carrying the lab forward. We were joined at various points by some excellent undergraduates, Paul King and Aaron Stahl. My advisor Steve

Rolston worked to impose order on the chaos of our lab.

Further, the support of the faculty, staff, and graduate students of the JQI is what keeps things going. Alessandro Restelli in particular shows endless curiosity and endless willingness to help improve whatever electronics project you may be working on. When (and long after) I joined, the senior grad students, in particular Creston Herold, Kevin Twedt, and Dan Campbell, answered my unceasing smart and stupid questions with equal amounts of patience. I've strived to follow their example. The longer I've been here the more people I thought of as senior graduate student left, and all the others banded together for mutual support. In particular, Dan Barker, Ryan Price, Varun Vaidya, Ben Reschovsky, and Neal Pisenti joined up around when I did, and without them I'd never have made it. Many other students joined as the years stretched on, and each of them brought something along with them. There isn't space to list them all here, but every one of them are appreciated and will be missed.

The breathing lattice project in particular was helped along by Victor Galitski and his graduate student Efim Rozenbaum, who provided a lot help early on when I was still getting my bearings. In particular, Efim answered many e-mails about chaos and level statistics that, although none of that made it into this work, were very helpful and appreciated.

I was blessed with excellent friends during my time in grad school. Housemates Trystan, John, Dan, Steve, Rodney, and others provided a relief valve when necessary, be it through food, video games, or chatting across a windowless basement office. Ryan, Lora, and their dog Baxter were always down for Mario Kart, although Baxter's

technique needs some work. I will forever be grateful for Lora's encouragement, without which I may never have worked up the courage to ask out my wife. Ris has supported me ever since that first lunch in high school.

My family has supported me throughout everything. Mom, Dad, and my sisters may be more excited than I am that I'm finally done with school, and have been consistently encouraging about this whole process. Finally, my wife Megan remains the best part of grad school. Her encouragement on bad lab days, and celebration on good ones kept me going. The most exciting part of finishing this thesis has been looking forward to life with her on the other side.

Table of Contents

Preface ii

Dedication iii

Acknowledgments iv

List of Tables ix

List of Figures x

List of Abbreviations and Symbols xii

1 Introduction 1
- 1.1 Bose Einstein Condensation . . . 2
- 1.2 Berezinskii-Kosterlitz-Thouless Transition . . . 3
- 1.3 Thesis Outline . . . 5

2 Rubidium Cooling, Trapping, and Imaging 6
- 2.1 Cooling and Trapping Techniques . . . 6
- 2.2 Optical Properties of Rubidium 87 . . . 12
- 2.3 Absorption Imaging . . . 13

3 Experimental Apparatus 16
- 3.1 Vacuum System . . . 17
- 3.2 Laser Systems . . . 22
- 3.3 Magnetic Field . . . 25
- 3.4 Imaging . . . 39
- 3.5 RF and Microwaves . . . 41
- 3.6 Optical Lattice . . . 42
- 3.7 Computer Control . . . 50

4 Disorder Layered Systems 52
- 4.1 Lattice RF Generation . . . 56
- 4.2 Single Particle Simulations . . . 58
- 4.3 Conclusions . . . 60

5 Breathing Lattice 61
5.1 Periodic Hamiltonians . . . 63
5.2 Time-dependent Unitary Transformations . . . 73
5.3 Breathing Hamiltonian . . . 75
5.4 Effective Hamiltonian . . . 78
5.5 Floquet Approach . . . 84
5.6 Numerics . . . 89
5.7 Results . . . 95
5.8 Future Directions . . . 101

6 Summary 103

A Essential Parts Lists 104

B Publication: Griffiths Physics in an Ultracold Bose Gas 109
B.1 Abstract . . . 109
B.2 Introduction . . . 109
B.3 Experimental Approach . . . 112
B.4 Analysis . . . 115
B.5 Conclusion . . . 125

C Breathing Lattice Fourier Components 127
C.1 Power Series in Cosines . . . 127
C.2 Power Series for Lattice Drive . . . 129
C.3 Fourier Components . . . 131

D SetList Feedback 134
D.1 NI Service Locator . . . 134
D.2 Protocol . . . 135

Bibliography 139

List of Tables

3.1 Zeeman slower electrical and mechanical parameters 26
3.2 Characteristic rise and fall times for levitation coil 36
3.3 Times to cross current thresholds during safety cutoff operations . . . 37

A.1 Essential components for constructing the vacuum system 105
A.2 Essential electrical parts for constructing the Zeeman slower and its current controls 105
A.3 Essential components for construction the quadrupole field coils and their controlling electronics. 106
A.4 Lasers used in the apparatus. 106
A.5 Essential parts for microwave and radio frequency (RF) generation. . 107
A.6 Essential parts for the imaging systems used in the apparatus. 107
A.7 Essential parts for the main and cross dipole traps. 108
A.8 Essential parts for computer control in the apparatus. 108

List of Figures

2.1 Two beam configurations and the potentials they generate 11

3.1 A labeled photograph of the atomic source section 17
3.2 A labeled photograph of the main chamber. 20
3.3 A technical drawing of the bucket window, included by permission of the Special Techniques Group. 20
3.4 A labeled photograph of the vicinity of the cell. 22
3.5 Electrical schematic for running a single Zeeman slower coil 26
3.6 Schematic of passive charging circuitry and current discharge control 33
3.7 Plots of the coil current and control signal for a typical current pulse. 35
3.8 Density plot demonstrating repeatability of coil rise and fall times . . 37
3.9 Traces of circuit behavior during safety cutoff operation for a typical operation 38
3.10 A schematic diagram of the opticas and beam paths for out optical lattice generator 45
3.11 A schematic representation and engineering drawings of the Mach-Zehnder interferometer 46

4.1 Normalized $p, -p$ correlations β for both lattice depths 54

5.1 Band structure diagrams for sinusoidal lattices 67
5.2 Wannier states for sinusoidal lattices 68
5.3 The Fourier transform of the time-averaged breathing lattice potential 77
5.4 The ratio of the critical drive frequency Ω_c to the external trap frequency ω_T for a given breathing amplitude γ. 83
5.5 The magnitudes of the Fourier components of the breathing lattice Hamiltonian 85
5.6 The scaling of the higher-order Fourier components for a cancelled time-averaged harmonic trap 86
5.7 A comparison of the two methods of computing the root mean squared deviations from 1. 93
5.8 Energy and quasienergy levels for two simulated lattices as γ is varied. 95
5.9 The onsite occupation amplitudes for the breathing lattice's eigenstates 96

5.10 Momentum and site-occupations probability densities for the breathing lattice's eigenstates . . . 98
5.11 The effective Hamiltonian for the breathing lattice . . . 99
5.12 The tunneling coefficients from the effective breathing lattice Hamiltonian . . . 99

B.1 A diagram of the superfluid pancakes in the generated disordered layered optical potential . . . 113
B.2 An example image from the experiment, along with its $n_\perp$ and $n_\parallel$ distributions . . . 116
B.3 The fraction of atoms in the Thomas-Fermi distribution as a function of temperature . . . 116
B.4 A random sampling of images at a few temperature ranges in our 2.8 kHz lattice . . . 118
B.5 The average density profile for the coldest temperatures together with $\overline{n}_\perp$ . . . 118
B.6 The mean fluctuation correlations of the momentum $\overline{\alpha}(p_a, p_b, T)$ . . . 119
B.7 Normalized $p, -p$ correlations β . . . 121
B.8 Squared fluctuations $\overline{\alpha}(p, p)$ . . . 124

List of Abbreviations and Symbols

1D	one dimensional
2D	two dimensional
3D	three dimensional
AI	analog input
AO	analog output
AOD	acousto-optic deflector
AOM	acousto-optic modulator
API	application programming interface
AR	anti-reflection
AWG	arbitrary waveform generator
AWG	American wire gauge
BEC	Bose Einstein condensate
BKT	Berezinskii-Kosterlitz-Thouless
CF	ConFlat® Flange
CW	continuous wave
DDS	direct digital synthesis
DO	digital output
DVR	discrete variable representation
EOM	electro-optic modulator
FIFO	first-in first-out
FOV	field of view
GPM	gallons per minute
HWP	half-wave plate
IP	Internet Protocol
JQI	Joint Quantum Institute
JSON	JavaScript object notation
MOSFET	metal-oxide-semiconductor field-effect transistor

MOT	Magneto-Optical Trap
NEG	Non Evaporable Getter
NIST	National Institute of Standards and Technology
NPBSC	non-polarizing beam-splitter cube
PBSC	polarizing beam-splitter cube
PCI	Peripheral Component Interconnect
PLL	phase locked loop
PVC	polyvinyl chloride
QWP	quarter-wave plate
RF	radio frequency
RMS	root mean square
SE	Schrodinger equation
TCP	Transmission Control Protocol
TDSE	time-dependent Schrodinger equation
TEC	thermo-electric cooler
Ti:sapph	titanium-sapphire laser
TOF	time of flight
TSP	titanium sublimation pump
TTL	transistor-transistor logic
USB	Universal Serial Bus

Chapter 1: Introduction

Since the initial realization of the rubidium Bose Einstein condensates (BECs)[1, 2], ultracold atomic gases have gradually transitioned from objects of fundamental research to tools for studying other quantum systems. Some experiments use them as sensors or physical standards, *e.g.* atomic clocks, while others utilize the atoms as quantum simulators. By taking advantage of the exquisite control available, clean versions of various condensed-matter systems can be studied.

This thesis contains works performed in a research group setting, and as such many people have made contributions. This and the following chapter (Chapters 1 and 2) are background research. My specific contributions to the physical apparatus were made during the rebuild, and other components are specifically mentioned in the relevant sections. The work in Chapter 4 was performed by our group, and my specific contribution are discussed in more detail there. The theory work done in Chapter 5 is entirely my own.

In the remainder of this chapter we will briefly cover the kinds of phases encountered in bosonic two dimensional (2D) and three dimensional (3D) ultracold gases before outlining the remainder of the thesis.

1.1 Bose Einstein Condensation

A BEC is a useful tool for quantum simulation. It exists only at very low temperatures, when the mean inter-particle spacing becomes comparable to the thermal deBroglie wavelength λ_{dB}[3]. At high temperatures a diffuse atomic gas is well-described by Maxwell-Boltzmann statistics, which gives the mean occupation number of a single-particle state with energy ϵ for a gas at temperature T with chemical potential μ. As the temperature of the gas is lowered, its behavior measurably diverges, now following Bose statistics[1]

$$f_B(\epsilon) = \frac{1}{e^{(\epsilon-\mu)/(k_B T)} - 1}. \tag{1.1}$$

At these temperatures, the wavefunctions of adjacent particles begin to overlap. This is conveniently parameterized by the phase space density

$$D = n\lambda_{\mathrm{dB}}^3 \gtrsim 1 \tag{1.2}$$

where n is the usual number density. Mean field theory predicts a BEC forms when $D \geq 2.612$ in a uniform 3D Bose gas. Once this condition is met, atoms begin collecting in the ground state of the system, forming the condensate. This is evident when considering that the ground state energy ϵ_0 sets an upper bound on the chemical potential, otherwise the ground state would apparently have negative

[1] Bose statistics reduce to Maxwell-Boltzmann statistics in the high-temperature limit.

occupation. The density of states for the free particle is

$$g(\epsilon) \propto \epsilon^{d/2-1} \tag{1.3}$$

where d is the dimensional of the system. It vanishes as we approach the ground state energy from above in 3D. So then, totaling the occupation of all excited states N_e by integrating the product of $g(\epsilon)$ and the Bose distribution in the limit $\mu \to \epsilon_0$ we may find for low enough temperatures that $N_e < N$. The remaining $(N - N_e)$ particles must be in the ground state, forming the BEC. We then describe them collectively with a single wavefunction, but now the macroscopic population allows its behavior to be observed above the background of the thermal atoms not in the condensate.

1.2 Berezinskii-Kosterlitz-Thouless Transition

The physics is rather different in 2D systems. There the density of states Eq. (1.3) is a constant, even for vanishingly small ϵ. There is therefore no upper bound on the number of particles that can be accommodated in the excited states, and thus no true condensation occurs in a homogeneous system. This is related to the Mermin-Wagner theorem[4], shown originally in the context of magnetization in the Heisenberg model,[2]

However this results applies only in the thermodynamic limit, and for finite size

[2] 2D ultracold atom systems map onto the Heisenberg model, along with other XY model systems, so the result applies here as well.

systems condensation may still occur[5, 6]. This was emphasized by Bramwell and Holdsworth, who stated "With [magnetization] $M(N, T_{\mathrm{KT}}) \lesssim 0.01$ as a reasonable estimate for the thermodynamic limit, the sample would need to be bigger than the state of Texas for the Mermin-Wagner theorem to be relevant!"[7]

Nonetheless the Berezinskii-Kosterlitz-Thouless (BKT) transition occurs in both infinite and finite systems, and is characterized by algebraic decay of correlations[8–12], in contrast with the observed exponential decay in thermal systems and infinite-range correlations in condensates. Below the transition temperature, vortices exist only in bound vortex-antivortex pairs. Since they induce opposite flows, far from the center of the pair the effect becomes vanishingly small, allowing for long range order to exist. Above the critical temperature it is energetically favorable for the pairs to unbind, and vortices quickly proliferate throughout the system, destroying any long range order.

BKT systems have been studied in a range of ultracold atom experiments[9, 11, 13–17]. These usually feature quasi-2D confinement, where a very anisotropic 3D harmonic trap confines the atoms to function effectively in only two dimensions. This is achieve by "freezing out" the out-of-plane dynamics, using atoms cold enough that thermal energy scale is much smaller than the harmonic energy spacing in the tight dimension, so that dynamics in this direction can be ignored.

1.3 Thesis Outline

In the remainder of this work we will discuss how we generate and manipulate these ultracold states of matter, covering the theory of the techniques in Chapter 2 and its implementation in our lab in Chapter 3. We will then cover two studies enabled by our particular optical lattice generation system; a experiment in 2D layered systems in Chapter 4, and a theoretical treatment of a breathing lattice in Chapter 5. Finally, a brief summary of the thesis will be provided in Chapter 6.

Chapter 2: Rubidium Cooling, Trapping, and Imaging

The physics we'll be studying in later chapters requires a source of atoms at very low temperature (10-100s of nK). Standard techniques to achieve this within a vacuum system have been developed. An overview of those techniques relevant to this thesis are presented within this chapter. They are presented roughly in the order they are encountered during an experimental cycle, beginning with slowing thermal beams of atoms, then methods of cooling them, and then various way to trap them. After the discussion of cooling and trapping techniques we will briefly mention relevant atomic properties in anticipation of their use discussing the imaging technique used in our lab.

2.1 Cooling and Trapping Techniques

Laser cooling and trapping is a ubiquitous technique in the study of ultracold atomic gases[18–21]. In this section I will provide an overview of the general principles in the standard techniques, and explain how those principles are combined at each stage of the experiment.

If a laser beam tuned to resonance is incident on an atom it will absorb and re-emit photons. The absorption will always provide a momentum kick in the same

direction, while the emitted photon goes into a random direction. Repeated over many absorption-emission cycles, this averages out to a force

$$F_{\text{scatt}} = \hbar k \frac{\Gamma}{2} \frac{I/I_{\text{sat}}}{1 + I/I_{\text{sat}} + 4\delta^2/\Gamma^2}, \tag{2.1}$$

where $\hbar k$ is the momentum carried by a single photon, Γ and I_{sat} are the spontaneous decay rate and saturation intensity for the transition, respectively, I is the intensity of the beam, and δ is the detuning of the beam from resonance. As the atom continues to scatter photons it will accelerate, eventually acquiring a Doppler shift that increases δ until the scattering force vanishes. Other methods to shift the transition frequency can bring the beam back into resonance. For instance, the Zeeman effect causes an energy shift proportional to the magnitude of the magnetic field.

To slow an atomic beam we arrange for the Zeeman effect to counteract the Doppler shift due to the decelerating atoms. This arrangement, called a Zeeman slower, as was first demonstrated in [22]. Many variations on this design exist, some replacing solenoids with arrangements of permanent magnets.

A pair of counter-propagating beams paired with a constant magnetic field gradient provides a restorative force towards the center of a cloud of atoms. Each beam is detuned from resonance at the field zero, and the polarization are chosen to be σ^+ and σ^- so they address spin states with opposite magnetic moments. Consider an atom within these beams near the zero-crossing of the field gradient; at exact center each beam has the same detuning, so it experiences a balanced force between

them. If it shifts to either side the magnetic field tunes one beam towards resonance while simultaneously detuning the other away from resonance. This provides a restorative force towards the zero crossing of the field, forming a trap in that vicinity. Repeating this configuration with two additional pairs of beams and a quadrupole magnetic field forms a Magneto-Optical Trap (MOT), first demonstrated in [23], following initial demonstrations with one beam in [24].

In addition to the restoring force, a MOT also provides a damping force. An atom moving towards one beam will see that beam Doppler-shifted towards resonance, and the opposing beam Doppler shifted away from resonance. This again unbalances the scattering rate, tending to slow atoms down, and does not require the presence of the magnetic field gradient. Removing the magnetic field removes the restoring force, but the damping force remains. This forms an optical molasses as demonstrated in [25]. Assuming a two-level atom, an optical molasses can only damp the velocity down to the Doppler cooling limit[26, 27], caused by the random momentum kicks from spontaneous emission and the fluctuations in the number of photons absorbed from the beams in any given time interval. This results in a random spread of velocities and is thus described by a temperature via the equipartition theorem. This lower-bound on the reachable temperature in a molasses is the Doppler temperature

$$T_D = \frac{\hbar\Gamma}{2k_b}. \tag{2.2}$$

T_D is not the fundamental limit for scattering-based optical cooling methods. Polarization gradient cooling (also known as Sisyphus cooling) allows sub-Doppler

cooling[28, 29]. In brief, if the atoms move in a polarization gradient (generated for instance from counter-propagating linearly polarized beams), their dressed state's energy depends on the local polarization. If near the peak they become optically pumped back to the other state, a net loss of energy occurs. This mechanism requires already cooled atoms to work, as the timescale for motion through the polarization must match the timescale between optical pumping events.

Without the light present, a magnetic field gradient is still useful for trapping, first observed in [30]. As noted above, the Zeeman effect causes an magnetic field dependent energy shift for atoms residing in it. Provided the atom moves slowly enough, the magnetic moment will follow the field. A local minimum of the field thus forms a local minimum of the potential the atoms sees, and can act as a trap. The gradient of the field provides a restoring force towards the center of the trap. A quadrupole field provides a local field minimum at its center, and can utilize the same coils already present to generate a MOT.

Magnetic traps provide no damping force. Instead evaporative cooling can be employed to lower the temperature of the trapped atoms. This method removes high-energy atoms from the trap, lowering the mean energy per atoms of those that remain[31]. One method used to remove the atoms is RF evaporation[32, 33]. Here radio waves are used to resonantly induce spin flips in the trapped atoms. A spin flip changes the sign of the magnetic potential and quickly ejects the atoms from the trap. The magnetic field provides a spatially-dependent detuning, allowing properly tuned RF to eject atoms at certain distances from the center. Atoms further from the center are in higher potential regions and thus necessarily have higher energy, so

selectively ejecting those atoms performs the evaporative cooling.

An alternate method of evaporative cooling is lowering the edges of the confining potential. It is possible in both a magnetic trap[34–36] and an optical dipole trap (first in [37] and later [38–41]). Again, only high-energy atoms can ever reach the edges of the trap, so as the barrier is lowered and these atoms escape, the average energy per remaining atoms decreases.

Thus far all the light discussed has been near-resonance light at low or moderate intensities. Far off-resonant light can form an optical dipole trap as was first observed in [42], but is now a common tool[17, 40, 43]. The electric field of an incident laser E induces an electric dipole moment $p \propto E$ for the atom. The atom interacts with the electric field E through this dipole moment as $V_{\text{dip}} \propto pE$. Recalling that the intensity $I \propto E^2$ this gives

$$V_{\text{dip}} \propto I \quad \rightarrow \quad F_{\text{dip}} \propto \nabla V_{\text{dip}} = \nabla I. \tag{2.3}$$

The sign of this term depends on the sign of the detuning with red- (blue-) detuned light providing attractive (repulsive) forces. A focused, red-detuned beam can thus trap atoms without any magnetic fields. Because the depth of the trap is proportional to the intensity, the above optical evaporation functions by slowly lowering the beam's power.

The dipole force allows any intensity pattern to generate a potential landscape for atoms. One common implementation is an optical lattice[17, 44–47], which uses interference of multiple light fields to generate periodic intensity patterns. The

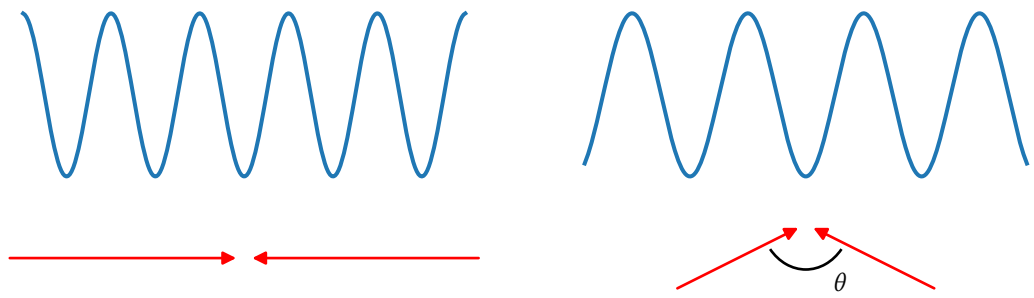

Figure 2.1: Shown are the beam configurations and generated potentials for (left) a retroreflected and (right) a shallow angle lattice. The spatial period of the lattice increases as the angle between the beams decreases.

simplest of these is a retroreflected one dimensional (1D) lattice. Here a single beam, reflected to retrace its original path, forms a standing wave pattern with itself as shown in Fig. 2.1. The resulting potential forms sheet or pancake-shaped potential wells, which along the laser-propagation direction varies as

$$V_{\text{latt}}(x) = V_0 \cos^2(k_l x) = \frac{V_0}{2}\left[1 + \cos(2k_L x)\right] \tag{2.4}$$

where $k_L = 2\pi/\lambda$ is the wavevector of the light with wavelength λ. Trivially the spacing between adjacent minima is $d = \lambda/2$. Additional retroreflected beams added in transverse directions would generate tubes in a 2D configuration, or a cubic grid in 3D. More complicated beam arrangement can generate other patterns of minima and maxima, providing a large variety of optical potentials to investigate.

Even for a 1D lattice the beams do not need to be counter-propagating to form a lattice. A pair of beams meeting at some angle θ still forms a standing wave pattern in space, but instead of homogeneous amplitude beating, there is a traveling component transverse to the lattice direction. The spacing d of adjacent minima of

the lattice formed by this configuration is

$$d = \frac{\lambda}{2\sin(\theta/2)}, \tag{2.5}$$

which in the $\theta = \pi$ limit for anti-propagating beams results in the expected spacing of $\lambda/2$. For limit of $\theta = 0$, d approaches infinity, which is the expected limit of co-propagating beams.

2.2 Optical Properties of Rubidium 87

Our experiment uses the D_2 line from $^2S_{1/2}$ to $^2P_{3/2}$ at 780.241 nm (Steck has collected from the literature many relevant parameters)[48]. The ground state has an F=1 and F=2 manifold separated by 6.8 GHz, and the excited state has F=0 to 3 manifolds. We work typically from the F=1 m_F=-1 state, a field sensitive state that is thus both magnetically trappable. It is also magnetically leviatable; by providing a uniform magnetitic field gradient parallel to gravity, an equal and opposite force can be applied, allowing the atoms to expand in-place during time of flight measurements.

For the following section we will need the optical scattering cross-section σ. The on-resonance cross section only depends on parameters of the transition itself

$$\sigma_0 = \frac{\hbar\omega\Gamma}{2I_{\text{sat}}}, \tag{2.6}$$

and decreases as the detuning or intensity increases

$$\sigma = \frac{\sigma_0}{1 + 4\left(\frac{\delta}{\Gamma}\right)^2 + \frac{I}{I_{\text{sat}}}}. \tag{2.7}$$

The additional level structure necessitates the inclusion of repumpers in any experiment, as the laser cooling and trapping processes discussed earlier in the chapter assume many photon scattering events. However, once they are in the excited state they not only decay to the original ground state, but may branch to other parts of the ground state manifold. If they end up in one of these other states, they are out of resonance with the cooling/trapping light and scatter no more photons. Atoms collected in these "dark states" are removed by adding a repumper laser. This resonantly excites atoms back into the excited state. From there they can again interact with the cooling/trapping light.

2.3 Absorption Imaging

Ultimately, the data we collect in our experiments comes from images of the spatial distribution of atoms. Many different imaging techniques are available, including some nondestructive options[49–52], but in our experiments we choose to use absorption imaging. This technique relies on detecting the shadow cast by the atoms in a beam of light to infer their distribution in space.

Beer's law relates the intensity of a beam to its initial intensity and a property of the medium is passes through called the optical depth τ. Simultaneously, the amount of light scattered depends on their density and the absorption cross section

σ from Eq. (2.7). Combined this is

$$I = I_0 e^{-\tau} = I_0 e^{-n\sigma}, \tag{2.8}$$

which establishes a relation between the density of the atomic sample and the darkness of the cast shadow.

To calculate the density, three images are captured for identical durations, as closely spaced in time as is technically feasible. For the first two images a probe beam briefly flashes on, and in the last, "dark," frame no flash occurs. The first image has atoms present and is the "atom" frame; the second waits until the atoms have left the field of view of the camera to expose the "reference" or "probe" frame. We will use F_{atom}, F_{probe}, and F_{dark} to reference these objects below, given in counts/pixel.

F_{dark} contains the signal from sources unrelated to either the atoms or the probe. This is typically dominated[1] by a camera-specific pattern caused by thermal effects in the sensor. The pattern has a consistent mean with small shot-to-shot fluctuations, and we subtract this background signal from the other frames to retrieve the portions that correspond to the intensity of the impinging light. Under the assumption that the illumination from the laser does not change between shots[2], the only difference between these adjusted frames is due to the absorption from the atoms.

[1] In principle other sources such as stray light are possible, but the imaging time is so brief that any signal from those sources is easily lost in the noise of the thermal counts.

[2] The validity of this assumption depends heavily on the experiment. However it is often possible to reconstruct the probe by referencing the unobscured portion of the cloud to some library of probe images

So far we have discussed the image only as measured by pixel counts. The conversion factor between counts and intensity before the atoms depends on the magnification of the imaging system; the quantum efficiency of the camera, which specifies what fraction of incident photons are converted to electrons; the gain setting of the conversion electronics internal to the camera, the duration of the imaging pulse, and the physical size of the light-sensitive area of the camera pixels. Appropriately combined these for a conversion coefficient β with units of intensity/count. The optical depth is then

$$\tau = \ln\left(\frac{F_{\text{probe}} - F_{\text{dark}}}{F_{\text{atom}} - F_{\text{dark}}}\right), \tag{2.9}$$

which combined with Eq. (2.8) recovers the column density of atoms for that pixel. Although in this form β is cancelled, higher order corrections involve the intensity directly.

Chapter 3: Experimental Apparatus

This chapter will discuss the apparatus built to perform dynamic lattice experiments. We will work our way through the lab category by category, beginning with the vacuum system, and proceeding through light and magnetic field generation, imaging, and RF and microwave generation. We will then detail our very flexible, phase-stabilized 1D lattice generation system, and close the chapter briefly covering our computer control system.

The current manifestation of our lab is an overhauled version of what is described in earlier theses from our group [53–55], so additional details about some aspects of the apparatus may be found there. The circumstances and design of the reconstruction are discussed in Matthew Reed's more recent thesis [56]. Additionally, other labs in the Joint Quantum Institute (JQI) were in their building phases around the time we began the overhaul, and many parts of this apparatus are adapted from their designs. Specifically, early theses from the RbYb mixtures group[57, 58] and the Sr group [59] contain relevant content.

The realities of building a lab in the United States mean that some parts are built and specified in inches, so throughout this chapter the units used will correspond to those used by the manufacturer and/or standard.

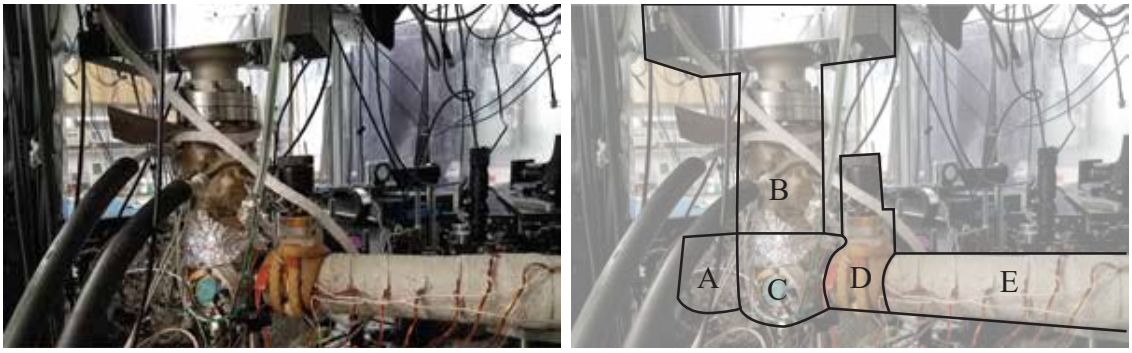

Figure 3.1: A photograph of the atomic source part of the apparatus (left), together with labeled outlines of particular components (right). From left to right, A: (behind the hoses, wrapped in foil) the atomic oven, B: pumping stack, C: cold plate/collimation chamber, D: manual gate valve and E: Zeeman slower.

Important parts will have part numbers provided where available, but common or interchangeable parts (e.g. standard wire or tubing) will only mention any relevant parameters. To improve both readability and usefulness of this chapter, a parts list for each major component is included as App. A. When mentioned in the the text, the appropriate line of the appropriate table is referenced, typeset as a superscript. For example, the slower current supply is referenced like this[A.2.2] in the section below.

3.1 Vacuum System

Atom Source

A photograph of the source section of our apparatus is shown in Fig. 3.1. Our atomic source can be divided into several sections: Zeeman slower, oven, cold plate/collimation chamber, and pumping. The pumping section is a 55 L/s[1] ion pump[A.1.3] mounted at the end of an 20 cm long 4½ inch ConFlat® Flange (CF)

[1]This pumping speed is not critical; historically we have also had 20 or 30 L/s ion pumps here.

extension tube. The pump sits at this distance to prevent stray fields from the magnets from degrading the slower's performance. It provides all the pumping for the source section.

The pumping section connects to the top of the spherical cube[A.1.7] that forms the cold plate/collimation chamber. The bottom contains a pair of mechanical vacuum feedthroughs. One is fixed and used as a heat pipe for the in-vacuum cold plate. A thermo-electric cooler (TEC) cools the in-atmophere side to temperature below 0 °C. The cold plate is a large copper disc with a small central aperture. A collimated beam of atoms from the oven can pass through the central portion, but diffuse spray (or the outer fringe of the beam) strikes and adheres to the cold plate. This helps keep the overall vapor pressure on the source low.

The other feedthrough is rotatable. It attaches to a small sphere with a hole drilled through it. In the past it functioned as an atom shutter, blocking the atomic beam from traveling into the chamber, but now it serves merely as a further collimating aperture for the atomic beam. Just behind the sphere is a short 8 cm long, ⅜ inch diameter aluminum tube used to provide differential pumping between the source and the main chamber.

A right-angle all-metal valve is attaches to one side, and provides access for an external turbo pump when necessary. The opposite face has a vacuum window that allows a camera view of the cold plate for alignment purposes.

The oven is build from a 1⅓ inch CF tee, blanked on one end, with a flexible bellows attached to the perpendicular port. The side that connects the cold plate chamber also houses a copper slug, drilled through to form the oven's nozzle. The

bottom of the bellows is blanked off as well. The bellows and the tee are each wrapped with their own heater tapes connected to individual temperature controllers. This allows the nozzle to be heated to 155 °C while the bellows is at only 85 °C. To load the oven, we remove the bellows and insert a small glass ampule containing a few grams of rubidium. Once reattached, the bellows and the source side are baked out, the ampule can be broken by careful flexing of the bellows.

Opposite the oven a manual gate valve[A.1.6] sits, allowing isolation of the source from the slower and the main chamber. This allows, for example, the rubidium source replacement without requiring a bake-out of the main chamber. Just past this valve is the Zeeman slower. A 14 inch long vacuum tube forms the vacuum portion of the slower (the electric portion is covered in Section 3.3). The far end attaches directly to the main chamber. Combined with the distance between the gate valve's flange and valve body, this provides approximately 36 cm of length for the slower coils.

Chamber

Our loading chamber is a spherical octagon[A.1.1] with 8 2¾ inch CF flanges along one circumference, and larger 6-inch CF for the top and bottom. Figure 3.2 gives a photograph of it and the attached vacuum pumps, windows, and other components. The larger flanges house two recessed window allowing close proximity of magnetic coils to the atoms. These recessed windows are custom parts ordered from the Special Techniques Group at the Culham Centre for Fusion Energy, and are shown

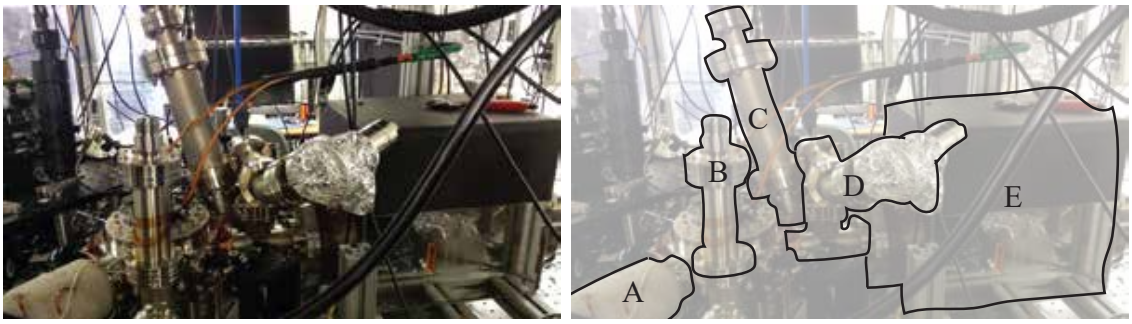

Figure 3.2: A photograph of the main chamber part of the apparatus (left), together with labeled outlines of particular components (right). From left to right, A: the Zeeman slower, B: NEG, C: TSP, D: all metal valve and ion gauge, and E: ion pump.

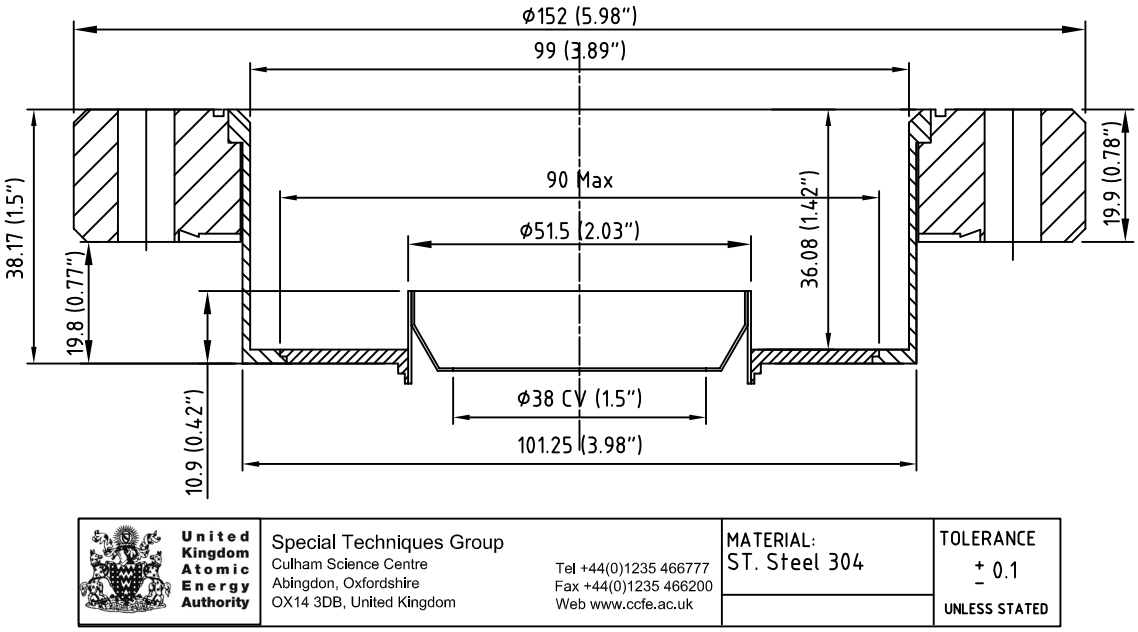

Figure 3.3: A technical drawing of the bucket window, included by permission of the Special Techniques Group.

in technical drawings as Fig. 3.3. Of the eight remaining 2¾ inch CF locations, five hold windows (two with intermediate CF tees), one attaches to the Zeeman slower discussed above, one to the cell (discussed below), and the remaining opening hosts the attachments to our main pumping section.

Three of the windows provide MOT beam access, and have corresponding anti-reflection (AR) coating at 780 nm. They are positioned 90° from each other and the pumping section. One of these windows connects through an intermediate CF tee that branches to an Non Evaporable Getter (NEG) vacuum pump, shown as Fig. 3.2B. A fourth window, located 45° from the pumping section shares this coating and handles Zeeman slower beams. It sits at the end of a 2¾ inch CF tee which branches to a titanium sublimation pump (TSP), shown as Fig. 3.2C. The remaining window fills the other 45° position from the pumping station. It is the exit port for our main dipole trapping beam, carrying the corresponding 1550 nm AR coating.

The NEG is a chemical getter.[A.1.4] Together with the TSP it provides very high pumping rates for chemically reactive vacuum contaminants. Neither can collect noble gases, but these are handled by the ion pump, a double-ended 150 L/s ion pump[A.1.2] provides much of our pumping. It attaches to the main chamber via the straight connection of a 2¾ inch CF tee-section, as seen in Fig. 3.2E. The remaining port of the ion pump houses the final MOT window. The top port of the above tee connects to an additional tee which houses an all-metal valve for pumping out the chamber on one side, and an ion gauge[A.1.5] to measure the pressure on the other, marked as Fig. 3.2D. This gauge routinely reads 4 nPa in the morning and 13 nPa

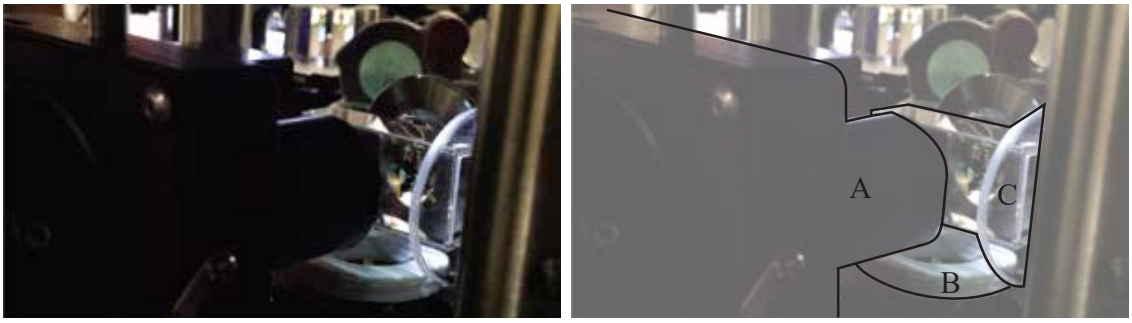

Figure 3.4: A photograph of the vicinity of the cell (left), together with labeled outlines of components of note (right). From left to right, A: the first stage of the horizontal imaging system, B: magnetic levitation coil, and C: glass science cell.

during an typical experimental cycle.

Science Cell

The science cell is an uncoated rectangular quartz cell[A.1.8] with $12.5 \times 22.5 \times 45$ mm exterior dimensions and 1.25 mm thick walls for all but the one open side. The National Institute of Standards and Technology (NIST) glassblower fused it to a glass-to-metal seal to allow attachment to the main chamber. The neck of this seal is a cylinder with approximate length of 4.5 inches and outside diameter of 1 inch. Figure 3.4 shows the cell *in situ*.

3.2 Laser Systems

780 nm Lasers

We have two 780 nm lasers in our lab. One[A.4.3] (the "main") provides the probe, MOT, and Zeeman slower light, while the other is primarily used for generating repumping[A.4.2] light.

A small fraction of main laser light is offset by an acousto-optic modulator (AOM) and directed to a Rb vapor cell. This generates a saturated absorption signal that locks the laser at a known offset from resonance. The bulk of the power is divided, shifted back towards resonance, and fiber coupled to other parts of the experiment. Depending on the downstream application, the shift may bring a beam back to resonance, or to some nearby frequency offset, so this scheme provides flexibility in detunings without requiring the manipulation of the offset frequency for the lock.

The repumper functions similarly but uses a separate vapor cell to generate its lock signal. It provides the repumpers for the MOT and Zeeman slower, and the optical pumping light for imaging.

1550 nm Fiber Laser

All our dipole traps are sourced from a 15 W Erbium-doped fiber laser system.[A.4.1] The output beam passes through an electro-optic modulator (EOM)[A.7.1] paired with a pickoff and photodiode to provide an intensity lock. A subsequent AOM[A.7.2] provides controllable splitting between two beam paths.

One path proceeds through a lens mounted on our air bearing stage.[A.7.3] This path forms the dipole trap in the main chamber, and translates to transport atoms from the main chamber into the science cell. The air stages translates the lens, moving the focal point of the beam from within the main chamber to within the science cell. A final periscope provides the degrees of freedom required to align to

the atoms in the chamber for capture and to place them at the desired location in the cell. The beam also passes through a polarizing beam-splitter cube (PBSC) just before the cell. The primary purpose of this cube is to allow the injection of the cross trap (discussed next), but it also enables the main beam to be picked off as an alignment tool. In additional to the intensity control from the EOM, a small mirror, mounted on the arm of a shutter, diverts the beam when the shutter activates. Because the EOM has a finite extinction ratio and the AOM has finite deflection efficiency, fullly eliminating the dipole trap requires the shutter.

The other, first-order beam path generates the cross trap. This light travels through a photonic band gap fiber[A.7.4] routed onto the cross trap breadboard. Once outcoupled, a pickoff with photodiode provide the lock signal needed for intensity stabilization using the above AOM. The light passes through an additional AOM[A.7.5] that splits it into two beams vertically. Downstream mirrors steer them to be parallel before they pass through a lens that combines them to form a crossed dipole trap. The PBSC mentioned above turns the pair to enter the front face of the cell, allowing the loose axis of the combined trap to be perpendicular to the lattice and horizontal imaging optics,

Titanium-sapphire Laser

A titanium-sapphire laser (Ti:sapph)[A.4.5] provides all the light for our optical lattice. This provides us with the ability to tune the wavelength of the lattice near 780 nm. One choice of wavelength allows direct imaging of the lattice, another choice

a few nm detuned is rejected by the imaging system. This second wavelength is used during experiments, and effects the atoms while avoiding pre-saturation of the camera before absorbption images can be taken. This importantly enables measurement of both lattice and atoms with the same optical setup, removing any possible scale discrepancies between them.

The Ti:sapph's pump laser is a Verdi V-10[A.4.4] at 532 nm. The two lasers share a closed-loop chiller[A.4.6] to provide cooling for both the Verdi head and the Ti:sapph crystal. This provides 2 W of power at the Ti:sapph output at optimal alignment. This light is then fiber-coupled and a small amount is picked off for a wavemeter. The wavemeter provides real-time measurement of the lattice wavelength, and is also logged at 10 s intervals to allow later verification of lattice wavelength during any given experimental cycle. The bulk of the light passes through a shutter and AOM before being fiber coupled to the optical lattice platform (discussed later in this chapter). This AOM together with a photodiode on the lattice platform provides intensity stabilization of the optical lattice.

3.3 Magnetic Field

Slower

The Zeeman slower consists of seven coils wrapped around a aluminum tube placed over a corresponding vacuum tube (see Section 3.1). The coils are made from rectangular-shaped magnet wire with 14 American wire gauge (AWG)-equivalent cross section. Varying both the current and number of turns for each coil set the axial

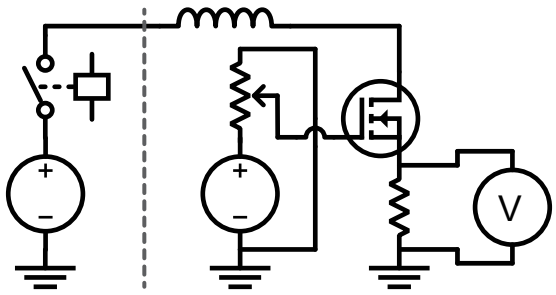

Figure 3.5: Electrical schematic for running a single Zeeman slower coil. The main supply and thermal protection relay left of the dashed line are common to all coils. Current flow through a given coil before reaching a MOSFET. The gate of the MOSFET is fed by a constant voltage from a trimpot, which controls the current through the coil. The final sense resistor after the MOSFET provides a current measurement location for the coil.

	1	2	3	4	5	6	7
Number of coil turns	40	40	40	40	80	120	80
Coil current (A)	8.40	7.00	0.546	1.08	0.548	-1.06	-4.88
Sense resistor voltage (mV)	420	350	27.3	53.8	27.4	-53.1	-194
Control trimpot order	5	3	4	2	6	1	7

Table 3.1: Relevant parameters for each section of the Zeeman slower, numbered consecutively starting nearest the oven and moving towards the main chamber. Positive current generates an axial field pointing towards the main chamber.

field. A constant voltage applied to the gate of a power metal-oxide-semiconductor field-effect transitor (MOSFET)[A.2.1] set the current in the coil. A precision 50 mΩ resistor in series with this coil provides the measurement location for this current. All coils share the same positive and negative supply rail provided by a single adjustable supply.[A.2.2] Figure 3.5 depicts this arrangement for a single coil.

Although an ideal field profile for a Zeeman slower exists, and the field profile of our slower could be calculated, we set the current in each coil through iterative adjustments selected to give the best loading rate in our MOT. Table 3.1 list the settings used for each coil together with the number of turns.

Using the same voltage supply for coils with widely varying current draws

causes some MOSFETs to dissipate tens of Watts of power. This adds thermal management requirements to the system. We use a recirculating chiller[A.2.3] to provide chilled water to a cold plate[A.2.4] to which the MOSFETs are fastened. Distilled water treated with an anti-corrosive agent is the working fluid, and it circulates at a temperature of 16 °C (though the temperature is not critical). To protect the MOSFETs from chiller (or some other loss-of-cooling) failure, the cold plate has an embedded thermistor. A circuit continuously monitors the cold plate temperature and uses a contactor[A.2.5] to disconnect the current supply if it gets too hot.

Quadrupole Coils

The quadrupole coils were wound on a pair of identical coil forms. They include a mounting flange for attachment to the chamber and a series of threaded holes to allow the mounting of optics directly to the form. A single narrow split reduces eddy currents in the form, whose purpose is to decrease the total decay time of the magnetic field to allow fast switching times. A thin piece of kapton film, applied to the entire mating surface, prevents current from shorting through the chamber and back into the coil mount.

The coils themselves are wound with 7 AWG equivalent square profile tubing,[A.3.1] which has a small central void to allow water cooling of each coil. Polyimide tape, wrapped around the circumference at the factory, provides turn-to-turn insulation. The final coil has 4 layers each wound 7 times, for 28 total turns. The tubing exits the forms through a window opposite the cut slot. Providing water-cooling

requires a water-tight connection to this square tubing that also provides an electrical connection. To accomplish this, the ends of the tube are soldered to short lengths of ¼ inch copper tubing for later connection to the plumbing system. Once fully wound, connectorized, and tested, the coil forms are bolted to their brackets and then installed in the bucket windows.

Now in place, they are attached via compression fittings to polyvinyl chloride (PVC)-jacketed ⅜ inch tubing. This provides electrical and cooling connections to the coil while keeping it electrically isolated from everything else on the optical table. The tubing extends over the edge of the table. To provide even cooling to each coil, we connect the water in parallel despite connecting them in series electrically. Each coil connects through a flow meter[A.3.2] and flow switch[A.3.3] to the house chilled water loop. The water it provides is at approximately 15 °C when it enters the lab. The university-supplied loop has a supply pressure 100 psi and return side 85 psi, which does not drive enough flow through the coils to be effective. Consequently we have installed a small booster pump[A.3.4] to provide 200 psi at the supply side, providing enough pressure for 0.3 gallons per minute (GPM) per coil. Because the chilled water is a communal resource, we have installed filters upstream of the booster to ensure the pump and coils are not damaged by any contaminant in the loop. The flow switches provide an interlock signal that disables the power supply output during a cooling failure, and are situated downstream of the coils. This ensures they place a *lower* (and thus safe for the coil) bound on the flow for all but catastrophic leaks.

Electrical connections are made under the optical table, just before the flow switches are inserted. The flow switches connect to the refrigerator tubing via short

sections of plastic tubing using a tee compression fitting. The supply side connecteds similarly. Welding cable lugs[A.3.5] are soldered onto short lengths of ¼ inch solid copper rods and attached to the remaining position on the compression fitting. This allows bolt-on connections to the 4/0 AWG[2] welding cable used to deliver current to the coil. The short between the two coils is similar, using a short section of solid rod *without* the lugs to connect two fittings. This provides an electrical connection while leaving the cooling water as two separate loops.

Together, the quadrupole coils provide a calculated magnetic field gradient of ≈1.15 G A/cm at the center of the pair. The desired magnetic trap gradient is ≈200 G/cm, and requires ≈200 A of current. A power supply[A.3.6] run in constant voltage mode provides this. Its positive rail sits at 8 V, and connects via the welding cable above to the first of the coils, passing through a current sensor along the way. The other cable runs from the second coil back to a common bus bar bridging the source terminals of four MOSFETs.[A.3.7] Four MOSFETs in parallel allow for open-circuit failure of one without causing the other three to leave the safe operating region. The drain terminals are tied together via another bus bar that connects to the ground terminal of the supply through a third welding cable.

The current sensor[A.3.9] provides a current proportional to the current in the coils. This current drops across a precision resistor and used as a feedback signal for a servo controller.[A.3.10] This feedback controller accepts an input signal from our control system and outputs the gate voltage for the MOSFET bank.

The MOSFETs do dissipate significant amounts of power at some points during

[2]Equivalently written as 0000 AWG

the experimental cycle. To provide cooling they are mounted to a water cooling plate like the one used for the slower above. The house water loop, rather than an in lab chiller, provides the cooling here, limited to 1.8 GPM by a similar flow meter with valve.[A.3.11] PVC tubing transports the water, and connections between the flow meter and the cooling block all are compression fittings.

Trim Coils

The main chamber has three mutually perpendicular sets of trim or shim coils available. Each coil is wound from 22 AWG magnet wire. One set was wound around the outside of the quadrupole coils before their insertion into the bucket windows. Each coil in this set has 30 turns. The other two sets are wrapped around the outer diameter of the 2¾ inch CF flanges attached to the chamber, and have 14 turns each.

Each pair of coils is connected in series such that the field they make at the center of the chamber is constant. The current fed to each determines the magnitude and direction of the field. A pair of constant-voltage supplies and a bipolar MOSFET controller provide the current control. A. Restelli and I designed the controller, which combines a push-pull configuration output stage with adjustable cross-conduction. The cross-conduction is adjustable to minimize the cross-over distortion as the output current ramps through zero in either direction. An integrated PI loop and current sensor provides closed loop control of the currents. More recently, Daniel Barker has developed an upgraded version of the current supply[60].

Levitation Coil

This section is adapted from a paper in preparation about the construction and performance of the levitation coil. The mount for the coil is visible below the glass cell in the bottom of Fig. 3.4.

Magnetic field control is an important item in the ultracold atomic gases toolbox. Magnetic field gradients interact with the magnetic dipole moment of individual atoms to provide a force cancelling gravity. Among their many uses are enhancing loading of optical traps[61–63], providing gravity-free expansion into external potentials[64–66], and extending time of flight (TOF) for imaging[1, 67]. Experiments that require a large degree of optical access but need only low duty cycle magnetic fields or gradients can benefit from small field coils.

The power requirements for the current pulses can be instantaneous large (100s of amps at a few volts, i.e. $\sim 1\,\mathrm{kW}$), but the average power requirement over an entire experimental cycle is actually quite low ($\sim 10\,\mathrm{W}$). This makes them well-suited to energy storage techniques using supercapacitors.[68, 69] Indeed, capacitor-based magnetic coil pulsing has been investigated for much larger requirements than those discussed here, such as magnetic resonance imagers (MRIs)[70] and plasma confinement coils in fusion research[71, 72].

In our lab we implement one such supply by integrating a few-amp input supply, discrete power MOSFETs, and a bank of supercapacitors (also known as electrolytic dual layer capacitors or EDLCs) to provide low duty cycle current pulses with 100s of amps for up to 200 ms. The simple overall design lends itself well to the laboratory

environment, enabling simple design tailoring and troubleshooting. The low average power requirements allow prevalent, inexpensive laboratory power supplies to replace high current supplies in these applications.

It also allows the coils, which will never experience to continous high current discharge, to utilize much finer gauge wire than would be otherwise expected. For instance, a 200 ms, 200 A pulse contains enough energy to raise a coil like the one used in our lab by less than 0.2 °C, even (incorrectly) assuming all the power dissapation occurs in the coil loop itself. This small amount of excess energy is easily passively dissapated during the large off time of the duty cycle. This in turn allows the use of a compact coil in locations that would otherwise be impossible due to optical access or mechanical design requirements.

Design

The design layout consists of two separate boards, a "charge board" and "discharge board". The charge board houses the supercapacitor bank and its charging circuitry. The discharge board contains the two power MOSFETs and their corresponding discharge control circuitry. A pair of short, 10-gauge copper wires connect the high current discharge path of the two boards. We chose to separate the two boards by function to allow for easier iteration and supercapacitor bank replacement, but the footprint could be substantially reduced by consolidating the two boards.

On the charge board and as seen in the upper left corner of Fig. 3.6, a high slew-rate op-amp senses the voltage of the supercapacitor bank V_{SC}. When V_{SC}

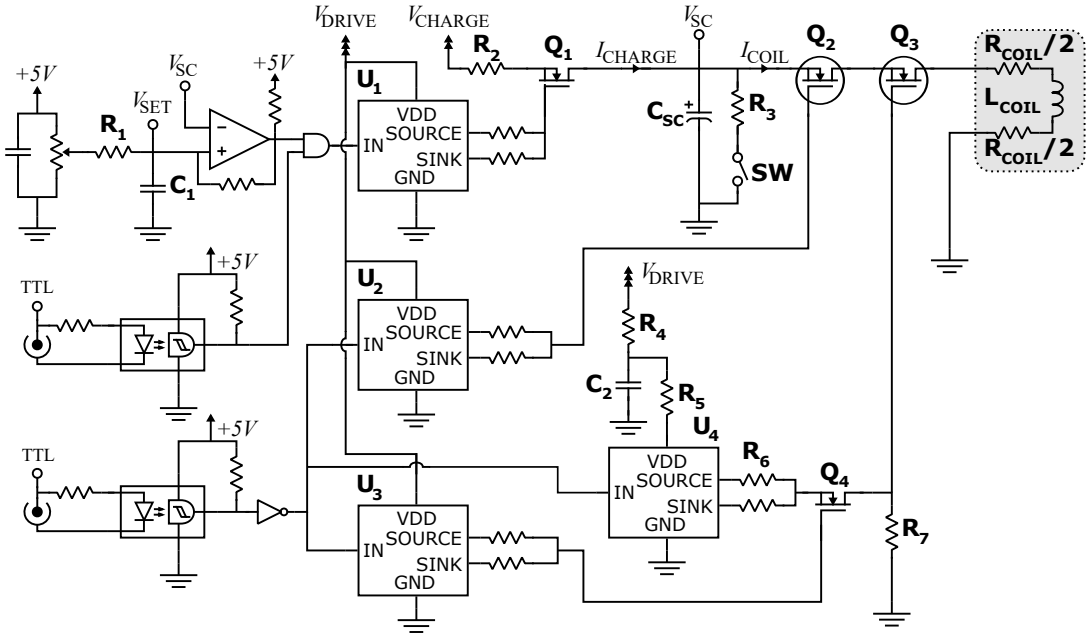

Figure 3.6: Schematic of passive charging circuitry and current discharge control. Schematic of TTL-level control integration. The design is split by function into two circuit boards, one for charging and one for discharging the supercapacitor bank. Both circuit boards receive signals "TTL" to control high current pulsing from a TTL-level pulse generator (PulseBlaster, etc). Two optocouplers, model H11L1M, protect the TTL-level source and invert the signal. On the discharge board, the signal is inverted again and fed to the high-current MOSFET drivers, TC4432, which drive the MOSFET gates using a 12 to 15 V source, V_{DRIVE}. The design minimizes MOSFET heating by limiting time spent in the linear region, driving gate currents at up to 1 A.

drops below the trimpot-controlled voltage V_{SET}, and the circuit is not actively discharging, an AND-gate lets current flow to the super capacitor bank. A separate, isolated power supply, typically set betwween 8 to 10 V charges the supercapacitor bank to V_{SET}, ranging from 0 to 5 V. The feedback resistor on the op amp removes oscillations around V_{SET}.

On the discharge board, two power MOSFETs Q2 and Q3 (model MMIX1F520 N075T2), control the high current discharge. The TTL input triggers MOSFET drivers U2 and U3 (model TC4432), driven by a 16 to 18 V external power source, V_{DRIVE}. Q2 and Q3 are arranged in series to isolate the safety mechanism responsible for limiting pulse duration via Q3. This configuration also offers optional current ramping via Q2 (an off-board amplifier uses a second low voltage signal to drive the gate of Q2). Placing Q2 and Q3 in series also provides redundancy in the event of a MOSFET failure.

The gate of MOSFET Q3 is charged by a capacitor, but simultaneously drained via resistor R7. This configuration provides a hard physical limit on how long current can flow though MOSFET Q3 before it shuts off. The values of R4 to R7 are set so that V_{DRIVE} * R4 / R7 is less than Q3's turn-on voltage of 2.5 V (resistance of R5, R6 are small compared to R4, R7). This ensures negligible current flows if V_{PULSE} is accidentally pulled high for too long. The RC constant for R4 and C2 sets the time taken to recharge, 15 s. This prevents the circuit from exceeding its intended low duty cycle. A consequence of driving the gate of Q3 with a capacitor is that the gate voltage will sag as the capacitor C2 discharges through R7, causing a corresponding drop in the discharge current. In order to keep the discharge current as steady as

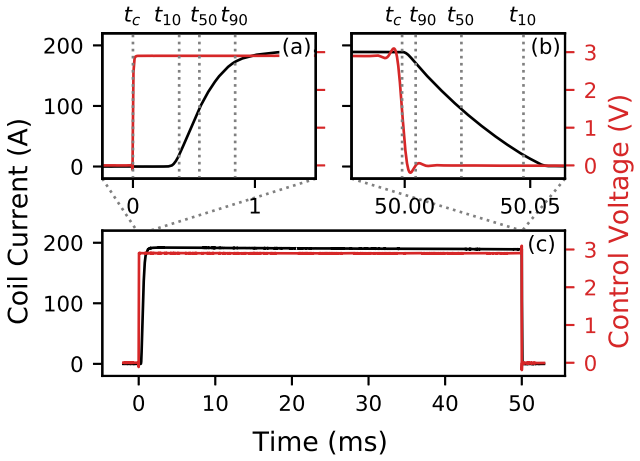

Figure 3.7: Plots of the coil current (black) and control signal (red) for a typical current pulse. Parts (a) and (b) show zoomed versions of the rising and falling edges, respectively. Times when important values occur are marked with dotted gray vertical lines for each. t_c is the 50% level of the control signal, while t_{10}, t_{50}, and t_{90} are the times of the equivalent current levels. Part (c) displays the entire duration of the same pulse as (a) and (b).

possible during the duration of a pulse, we leverage MOSFET pinch-off on Q4 to keep a steady voltage output on the gate of Q3. Figure 3.9 shows the behavior of this scheme.

Performance

To characterize the performance of the coil, we inserted a current transducer (Danfysik Ultrab 867-2001) on one of the leads of the coil. The output of this sensor and the control voltage were both read by a digital sampling oscilloscope, and the recorded data was digitally filtered to the bandwidth of the current sensor (150 kHz). The circuit was then triggered using a pulse generator giving 50 ms pulses every 30 s, which simulates a typical experimental cycle in our lab. An example of one typical pulse is shown in Fig. 3.7. We capture data from 100 consecutive pulses for offline

Edge	Delay (µs)	Jitter (µs)	Transition (µs)
Rising	543.	8.	450. ± 20.
Falling	23.63	0.02^3	43.09 ± 0.06

Table 3.2: Table reporting characteristic timescales for our circuit, extracted from 100 pulses such at the one shown in Fig. 3.7.

analysis.

For each pulse we can identify the times certain thresholds are crossed. Specifically the time the control signal reaches 50% is t_c, and the times the output current reaches 10% (50%, 90%) of its final value is t_{10} (t_{50}, t_{90}). These points are used to calculate the average delay time ($t_d = t_{50} - t_c$), the jitter (σ_{t_d}), and the transition time ($|t_{90} - t_{10}|$) for both edges of a current pulse. These times are displayed in Table 3.2.

We measured the load presented by the coil and its leads *in situ* using both a vector network analyzer and a simple four wire-resistance measurement. This yielded a DC resistance of 16.7 mΩ and an effective inductance of 1.79 µH. The turn-on transition time is thus limited by the load to a lower bound of 235 µs. Comparison with the measured rise time gets agreement to within a factor of 2, so we did not seek to optimize it further.

Because the coil current flows directly from a discharging capacitor, it slowly decreases during the pulse. We are operating in the $t_{\mathrm{PULSE}} \ll \tau_{\mathrm{RC}}$ limit, so the change in current is approximately linear. For our typical parameters, a 200 A pulse of 50 ms duration, this rate is (-61 ± 1) mA/ms. Decreasing this rate is easily accomplished by expanding the supercapacitor bank to raise C_{SC}. Assuming current noise uncorrelated with the measurement noise floor, this noise is (7.5 ± 5.9) mA rms.

Figure 3.8: Density plot for traces of the current for 100 pulses. Parts (a) and (b) correspond to the same regions as Fig. 3.7 (a) and (b). Color scale shows the fraction of traces that pass through that bin.

Current (A)		Time (ms)			Description
$t_{185\mathrm{A}}$	185	179.	$\pm$	1.	Beginning of Turn-off
$t_{100\mathrm{A}}$	100	290.91	$\pm$	0.06	Half of full scale
$t_{10\mathrm{A}}$	10	489.5	$\pm$	0.2	18 AWG wire Ampacity
$t_{1\mathrm{A}}$	1	578.2	$\pm$	0.9	26 AWG wire Ampacity

Table 3.3: Reports when the output current falls below the indicated thresholds during long-pulse pinch off. Values are extracted from 186 pulses such at the one shown in Fig. 3.9. Reasons for selecting each current threshold are given in the text.

This is consistent with the measurement noise of 20 ppm on 200 A from our sensor. We expect the noise from this circuit to be very low, as the supercapacitor will filter out almost all the supply noise, and the only active components on the discharge side are MOSFETs used in saturation. As a result, we expect the dominant noise source to be the channel noise in the MOSFETs. A worst-case estimate for this noise (within the sensor bandwidth) in our system bounds it to <6.3 mA rms.

To demonstrate the repeatability of this device we show a density plot in Fig. 3.8, where the region of the plot is divided into an array of bins whose contents are the fraction of pulses that cross them. The rising edge in part (a) shows a few deviations to faster rise times, while the falling edge in (b) is very consistent from pulse to pulse.

This particular combination of high current pulses for short times also allows the

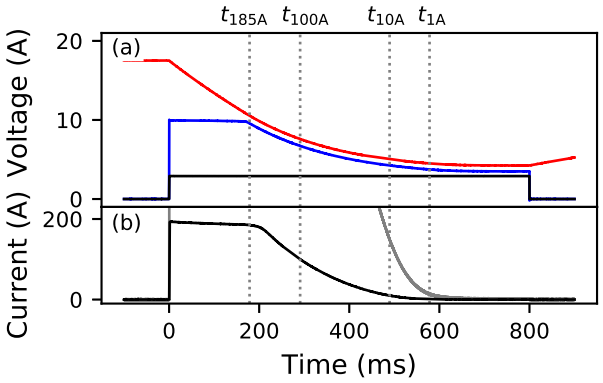

Figure 3.9: Traces of circuit behavior during safety cutoff operation for a typical operation. Part (a) shows three voltages: the control voltage (black) which pulses on for 800 ms, the MOSFET gate voltage (blue), and the RC timer voltage (red). The corresponding output current is show in Part (b) in black. A 15× magnification of that trace is shown in grey. Positions of current threshold crossings are marked with vertical dotted lines, and are listed in Table 3.3.

use of magnetic coils that are smaller than would be possible at DC. This necessarily means inadvertently long pulses have the possibility to damage (or destroy) the coil. Figure Fig. 3.9 demonstrates the cutoff of the current pulse during a longer-than-desired current pulse. The control signal is pulsed high for 800 ms, however the current is almost entirely cut off by 600 ms. This is accomplished by driving the gate of the second MOSFET Q_3 with an RC circuit as described above. As the voltage falls towards the supercapacitor bank's charge level, the current begins to pinch off. The current crosses several thresholds as the circuit continues to discharge. The values and times of these crossings are presented in Table 3.3.

The onset of cutoff is is certainly noticeable in these pulses at a current of 185 A, and occurs at 179 ms, setting an upper bound on the undisturbed pulse time. By 291 ms the current has already fallen to half of its maximum value. Two other relevant currents are determined by the possible choices for the wire of the coil. We

would like the current in the coil to fall below the steady-state ampacity of the wire before a fusing time given by the Onderdonk equation is reached. For a 32 ms (1 s) fusing time the corresponding wire size is 26 (18) AWG, whose ampacity is >1 A (10 A). The times to fall below these thresholds are 578 and 490 ms respectively.

3.4 Imaging

The apparatus has several imaging systems available. Each is primarily used for absorption imaging (see Section 2.3), though occassionally fluorescence imaging assists in finding proper focus. We describe each below.

Chamber

The main chamber possesses an imaging system with a net magnification of 0.35×. It uses the same beam path as the ion-axis of the MOT, but uses the opposite circular polarization of the MOT beams. The probe light combines with the MOT light at a PBSC before the quarter-wave plate (QWP), giving this polarization relationship automatically. This allows the imaging light to be split using a PBSC after the QWP on the far side. The QWP is already necessary for MOT operation, so only the PBSC and a half-wave plate (HWP) have been added to accommodate the probe.

Unfortunately, the MOT-probe splitting is not perfect. The probe is off during the MOT-loading phase, so probe light leaking into the retro leads only to a loss of signal. MOT light leaking along the probe path causes a more severe problem.

If allowed to impinge on the camera it will generate electrons faster than they can eliminated, causes the first image to saturate before it is even exposed. A shutter protects the camera from this MOT beam exposure, and it is the settling time of this shutter that sets the lower bound on the time between extinguishing the MOT and capturing an image.

The camera used for this system is the discontinued Flea2.[A.6.1] It features an array of 1384×1032 square pixels with side length $4.65\,\mu\text{m}$.

Vertical

The camera used for the vertical imaging system is a Flea2G,[A.6.2] with a 1288×964 array of $3.75\,\mu\text{m}$ square pixels. It attaches to a $2\times$ magnification imaging system mounted on a three-axis translation stage above the science cell. The vertical range of travel allows it to be set for focal planes coincident with either the *in situ* dipole trap or the location of the atoms after TOF. The achievable spatial resolution in this direction is fundamentally limited by the science cell dimensions, because the fused corners of the top face of the cell limit the optical access.

Horizontal

The horizontal imaging system was primarily designed and implemented by Matt Reed, and he details it in Sec. 3.3 of his thesis[56], so here we will mention only its high-level features. It also utilizes a Flea2G camera partnered with one or both stages of a high-magnification imaging system. The first stage provides a

magnification of 5.7× on its own, providing at least 1.3 µm of resolution. It is visible coming in from the left of Fig. 3.4. The second stage has its own magnification of 4× and is positioned so its object plane coincides with the image plane of the first stage. Together they then provide a magnification of 22.8× The high magnification system contains a long-pass filter[A.6.3] a turning mirror, allowing the rejection of most of the lattice light from the system. A subsequent short-pass filter[A.6.4] blocks much of the remainder. This prevents the thermal saturation problems described for the chamber imaging system, and allows the exposure of images of the atoms with the lattice on.

Calibration

For all systems, except the high-magnification horizontal system, magnification calibration stems from TOF measurements of atom free fall used as a measurement of gravity. The high magnification version of the horizontal cell imaging stack has insufficient field of view (FOV) to allow this, but because the optical lattice shares the same beam path, measurements of the lattice in both the high- and low-magnification configurations connect the low-magnification calibration to the high-magnification one.

3.5 RF and Microwaves

The required RF for evaporation in the magnetic trap is generated by a PulseBlaster[A.5.8] interfaced digitally to the frequency control of a programmable frequency source.[A.5.7] An external analog input on the source provides amplitude

control. A 10 W amplifier[A.5.1] provides the necessary power that our hand-wound loop antenna couples into the chamber. We made only a minimal effort to optimize the broadcast power, so a high-power terminator inserted after the antenna prevents the back-reflection otherwise expected from an open-circuit termination.

We also use microwave sweeps to selectively transfer populations between hyperfine states in the cell. They are built up in a chain starting from a function generator[A.5.2] with externally controlled frequency modulation. It provides the clock for a fractional phase locked loop (PLL) board[A.5.5] that multiplies the frequency to 3.4 GHz, whose output feeds a frequency doubler[A.5.3] and high pass filter.[A.5.4] A preamplifier[A.5.6] and an attentuator brings the power up to the correct input level for the final traveling wave tube amplifier.[A.5.10] After the amplifier a directional coupler and circulator provide measurement locations for outgoing power and back reflections. A stub tuner[A.5.9] provides impedance matching for out final microwave antenna, which couples directly from the waveguide[A.5.11] into free space.

3.6 Optical Lattice

Note: This section is adapted from an in-preparation paper describing the construction and performance of our lattice generation system.

Interference fringe patterns generated by monochromatic light have many uses across a variety of fields. In 3D profilometery projected macroscopic fringes indicate distances by revealing accumulated differential optical path length.[73–76] Ultracold atomic gas experiments use them to create structure in collections of

neutral or ionic atoms via the dipole force the fringes exert. Industry combines these interference fringes with high power pulsed lasers for micromachining[77–79] and laser marking[80].

Efforts to make various parameters of these patterns tunable have been similarly widespread. Shallow-angle lattices formed by injecting parallel beams into a lens are tunable by changing the input spacing between the beams. Many optical arrangements provide this, including: translation [81, 82] or rotation[83, 84] of an optical element, or using an AOM (or acousto-optic deflector (AOD)) to change the angle a beam enters a lens[85, 86]. Alternatively, a partial reflection from an angled surface form one of the beams for the lattice[87–89]. The flexibility of RF drive in the AOM-based approach allows tuning of the period and phase of the fringes by changing the RF drive[90–94].

A rapidly tunable fringe generation system provides the ability to do Fourier synthesis with optical fields. This allows, for example, the creation of unique, configurable disorder patterns. Because the constructed pattern depends on the relative phase of each component fringe pattern, its total shape is sensitive even to common-mode drift of the optical phase. Concretely, a change in optical path length of one beam of a shallow angle lattice changes spatial position of the lattice by an amount proportional to the fringe spacing. This causes each component fringe to translate by a differing amount, changing the shape of the intensity pattern. This affects even two-period lattice systems. For example, in bichromatic lattices[95, 96] the relative lattice phases control the spacing of two species.

We have designed and utilized a system capable of period and phase control of

optical lattices, including the ability to time-average at least seven distinct lattices into an optical potential for an ultracold atomic gas. It includes a phase stabilization technique to ensure the effective potential does not change over an experimental cycle.

Design and Construction

Functionally, the system can be divided into three sections. The first generates the optical lattice, and can function entirely without the other two. Its performance is enhanced by the others. The second measures the phase of the optical lattice. Finally, some components provide the feedback necessary to phase-stabilize the lattice. We present each section in turn below.

Multifrequency Lattice

All components, except for the final lens, are mounted on the same optical platform to provide passive stability for the system. The formation of the lattice begins with ≈ 800 nm light exiting from a single-mode polarization-maintaining optical fiber, as shown in Fig. 3.10(a). The light is intensity-stabilized using a small portion of light picked off after polarization purification. Then the light is split into two equal-power beams via a PBSC and HWP. The polarization is subsequently aligned to the preferred polarization via another HWP in each arm. The first beam proceeds directly through an AOM. The other first reflects from a piezo-actuated mirror (described further in Section 3.6) before passing through its own AOM.

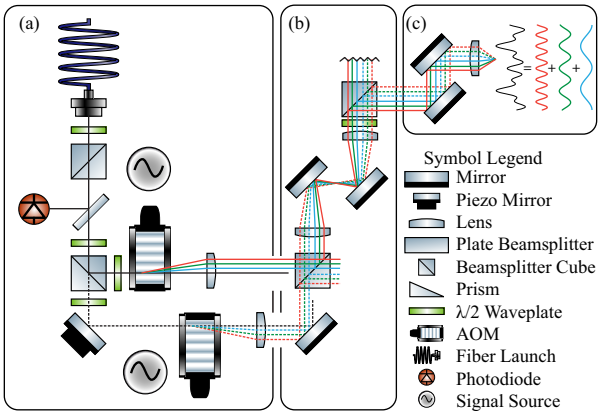

Figure 3.10: A schematic representation of the optics and beam paths for our optical lattice generator. Light enters through an optical fiber at the top of part (a) before splitting into two beams. One beam reflects from a piezo mirror, and beams from this path are rendered with dotted lines. Each beam passes through an AOM and receives one of many possible frequency shifts and angular deflections. Three such shifts are shown here as different line colors. The sets of beams are recombined in part (b) before finally forming a shallow-angle optical lattice in (c). Not shown is the interferometer section at the top of (b), shown instead in more detail in Fig. 3.11. All components except the final lattice-forming lens are mounted on the same optical platform to provide passive stability. More detailed discussion is in Section 3.6 of the text.

Each AOM deflects the beam through an angle determined by its drive frequency. Thus each input's set of all possible beams form a fan with some origin point, which may be a virtual point outside of the AOM. A lens is placed with its back focal point coincident with this origin point. It converts the fan into a set of parallel beams whose lateral position depends on the AOM frequency.

This happens in each arm, with the new beams meeting at a non-polarizing beam-splitter cube (NPBSC) (see Fig. 3.10(b)). The undiffracted beams are clipped here with a pair of beamstops. Hereafter the previously separated beams form a pair traveling entirely through the same optics, making most environmental perturbations on their phases common mode. A set of lenses relay the beams to a second PBSC. A small fraction of the power in each beam enters an interferometer (described below in

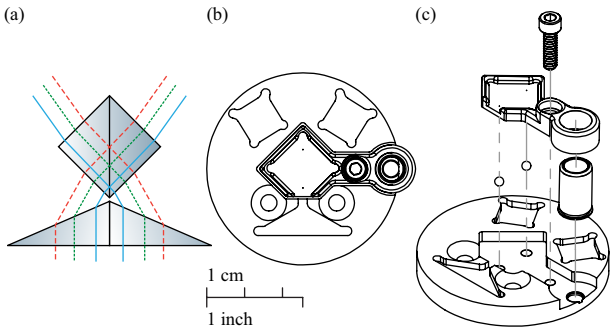

Figure 3.11: A schematic representation of the beam paths (a) together with a top-down drawing (b) and exploded isometric drawing (c) of the Mach-Zehnder interferometer without the optics installed. The solid blue, dotted green, and dashed red lines each represent a pair of beams with the same frequency shift. The beams enter from the bottom of the figure and correspond to those truncated at the top of Fig. 3.10(b). A pair of identical prisms deflect beam pair to cross along one line, enabling a single cube to simultaneously form a Mach-Zehnder configuration for every beam pair.

Section 3.6). The remaining bulk of the power proceeds to a final lens (Fig. 3.10(c)) which focuses them to the same point, overlapped with a cold atomic cloud. This forms a shallow-angle optical lattice.

The separation of the beam pair at the final lens sets the period of the optical lattice. Because the lateral position of the beams stems from the drive frequency of the AOMs, the drive frequency sets the final period. By connecting each AOM with one of a pair of synchronized arbitrary waveform generators, a train of pulses at different frequencies becomes a possibe drive. If sufficiently rapid these pulses form a time-averaged optical potential for appropriately prepared cold atomic clouds. The relative phase of the drive for each pulse sets the phase of the optical lattice in real space.

Interferometer

A Mach-Zehnder style interferometer measures the relative phase of the two arms. It consists of a pair of identical prisms placed back-to-back with a subsequent NPBSC, as show in Fig. 3.11(a). Each prism deflects the beams from one arm towards the center of the interferometer. The NPBSC's reflective surface is coincident with the line formed by the intersection points of the beams. This completes a Mach-Zehnder simultaneously aligned for any possible AOM drive frequency.

This flexibility comes at the cost of extra constraints on alignment. The input face of the prisms must be normal to the propagation direction of every beam, and the centerline of the prisms must bisect the beam pairs. To facilitate this, the interferometer sits on a rotation stage mounted in turn on a translation stage. In addition to these restrictions, the NPBSC may have a very slight rotation about the input beam propagation direction due to assembly from the manufacturer. To overcome this, we provide a top (or twist) degree of freedom for the beamcube relative to the prisms. The required pivot is placed directly below the cube to minimize the undesired translation coupled from the desired rotation of the cube.

We designed and manufactured the interferometer mount, whose drawing is displayed in Fig. 3.11(b-c), in-house. The optics forming the interferometer are referenced to a machined angle and permanently attached using epoxy. Also included are seats for prism mirrors at the output faces of the NPBSC to redirect the beams, a pocket for the insertion of a preload spring for the kinematic arm, and a bushing for a fine-thread adjustment knob. Two ball bearings sit between conical seats to

provide the pivot axis for the NPBSC.

Once properly aligned, a pair of photodiodes captures the output of each arm of the interferometer. The quadrature signals are then fed into an intensity normalization circuit that performs

$$V_{\text{out}} \propto \frac{V_A - V_B}{V_A + V_B} \tag{3.1}$$

where V_A and V_B are the voltages from each photodiode. Because the voltage for each is proportional to the intensity in the arms, and the intensity in one or the other arm is given by $I_0 \sin^2(\Delta_\phi)$ or $I_0 \cos^2(\Delta_\phi)$, this simplifies to

$$V_{\text{out}} \propto \cos(2\Delta_\phi) \tag{3.2}$$

where Δ_ϕ is the phase difference between the two arms, irrespective of the total intensity of the input. This phase-sensitive signal provides the feedback signal for phase stabilization for our lattice.

Phase Control

The phase of the optical potential at the final focus originates from a combination of the optical path length difference between the two arms and the relative RF phase in the AOMs. The AOM phase is a desired experimental parameter; however, the optical path length provides a source of instability. These optical path length changes arise from many possible sources, for example: mechanical expansion,

vibration of optics mounts, or changing air currents. Most of the beams' travel is within common mode optics. For a short distance beam pairs are necessarily traveling different paths, and may acquire differential shifts. The most straightforward correction to these shifts is an equal and opposite adjustment to the optical path of one arm. The piezo-actuated mirror, mentioned above and shown in the lower-left corner of Fig. 3.10, provides such a shift.

The characteristics of the piezo response limit the total bandwidth of the phase-stabilization system. We attempt to push any resonances toward higher frequencies by using the techniques from [97]. The low noise piezo driver from Pisenti et al. [98] provides the required high voltage drive. The low-bandwidth feedback provided by this controller helps extend the locking time by shifting the DC setpoint over time, keeping the high-frequency feedback range centered at longer timescales.

To fully utilize this system, we require a flexible RF generation platform. A pair of 5 W, 300 MHz bandwidth amplifiers boosts whatever signal we provide to the proper level for the AOMs. The signal source we use is a pair of arbitrary waveform generators (AWGs), with 1.024 GHz output frequency. One is configured as the "leader", and provides the output clock for itself and the other "follower", preventing any relative timing drift due to mismatched internal oscillators. The specific device is not critical, and future experiments may replace the AWGs with any other source with suitable output frequencies.

3.7 Computer Control

Two computers working in tandem provide the experimental control and data acquisitions functions for the lab. One computer handles image acquisition and analysis while the other programs the various hardware devices used to interface with the lab equipment.

Software on the acquisition computer is configured to expect some number of images per cycle. It downloads each captured frame from the cameras as they become available. Once it gathers all frames from an experimental cycle, they are bundled and saved to disk. It then signals Igor[99] to perform analysis.

The control computer connects to many devices to provide digital output (DO) and analog output (AO) functionality for the lab. The outputs of these are then routed to whatever object requires a control signal. The primary device is a PulseBlaster,[A.8.3] used to provide 24 DO in addition to controlling timing throughout the experimental cycle. It has 4 ns of timing resolution[4], which is sufficient for all experiments performed in our lab. Some of its outputs are reserved as trigger lines for other devices in the lab; the PulseBlaster sends pulses on these channels to signal connected devices to perform the next programmed action. In this manner the PulseBlaster oversees the timing and synchronization of an experimental cycle. The AO channels used in our lab are provided by a pair of Peripheral Component Interconnect (PCI)[A.8.1] cards and one Universal Serial Bus (USB)[A.8.2] device provided 20 total output channels. The USB device has an additional 48 DO channels as well

[4]This is distinct from its minimum 10 ns pulse time

as 32 analog input (AI) channels.

All these devices are programmed by the SetList[100] software package, written in LabVIEW[101]. It is an object-oriented overhaul of a predecessor program from the NIST Laser Cooling and Trapping Group. The present version was initially written by C. Herold, J. Tiamsuphat, and Z. Siegel, with one of the main design goals being increased portability and extensibility. This was successful, with D. Barker, N. Pisenti, B. Reschovsky, myself, and others significantly expanding the number of devices supported since its initial release. Especially notable features implemented by myself include an external feedback application programming interface (API) (see App. D), control sequences saved to a local Git[102] repository (complete with human-readable *diff* generation), and periodic background auto-saving for possible crash recovery.

SetList's main interface is provided by an expansive text table. Each device under control possesses some number of columns within the table, and each row represents a state (or ramp between states) at a given time during the experimental cycles. Every device is associated with a (possibly shared) trigger line. At the start of a cycle SetList converts this table to programming instruction for every device, programs each device sequentially, and then initiates a cycle by starting the PulseBlaster. SetList then idles until the cycle is complete before checking for any reported errors.

Chapter 4: Disorder Layered Systems

The apparatus detailed in the previous chapters was built to realize especially configurable optical lattices. In this chapter we use that configurability to explore a phase transition in 2D layered systems, which are known to posses Griffiths phases.

The study of 2D systems can be extended to include layered systems, where a series of internally 2D systems are coupled together along the third dimension. Many XY model systems allow this type of coupling, including ultracold atomic superfluids[103], superconductors[104], and layered planar magnets[105], and even lipid-DNA complexes[106]. Including disorder in this third dimension (be it via varying layer thickness, material, interlayer coupling strength, *etc.*) enriches the available physics. Theoretical studies of these systems suggest the emergence of Griffiths phases as the systems are cooled. Eventually the out-of-plane couplings allow full 3D condensation.

Griffiths showed[107] that in dilute Ising models[1] the magnetic susceptibility is non-analytic at zero field, and that the existence of isolated clusters of spins within the system drives this behavior. This mechanism is later identified as causing finite correlations above the spin-glass transition in Ising spin glasses[108], and these

[1] 2D or 3D lattices of spins with nearest-neighbor interactions and sites randomly occupied with some probability < 1

unexpected correlations are a key signature of a Griffiths phase. Specifically the Griffiths phase region occurs when a disordered system is above its own transition temperature, but below the highest transition temperature of a companion system with the same *distribution* but different *instantiation* of disorder[109, 110]. More concretely, for N realization of systems with a given distribution, the ith system will have a transition temperature T_i. Across all systems there will be minimum and maximum transition temperatures $T_{\min}$ and $T_{\max}$. The Griffiths phase for the ith system occurs in the region $T_i < T < T_{\max}$.

In layered systems, the relevant long range correlations are phase stiffness (or bulk magnetization) through the layering direction. This results in a sliding phase, where some order parameter is able to shift between neighboring layers without an energy cost. This was first mentioned in the aforementioned DNA complexes[106], where O'Hern et al. emphasize that *sliding* does not imply *decoupled*. While both mechanisms allow this shifting without energy cost, in the sliding phase long range correlations will still exist.

Our lab worked on identifying a phase transition in a disordered, layered system in 2017-2018. Part of Matthew Reed's thesis [56] discussed that work, and we recently published this work in [111]. Appendix B containes the full text of that publication. The bulk of the details is left in those references, but in summary, we generated a superposition of optical lattices to realize a system of coupled, disordered 2D systems. We measured an overall temperature dependence to the intralayer coherent fraction, through the fraction of atoms in the Thomas-Fermi part of a TOF distribution. This suggests individual planes have begun to cross their critical temperatures

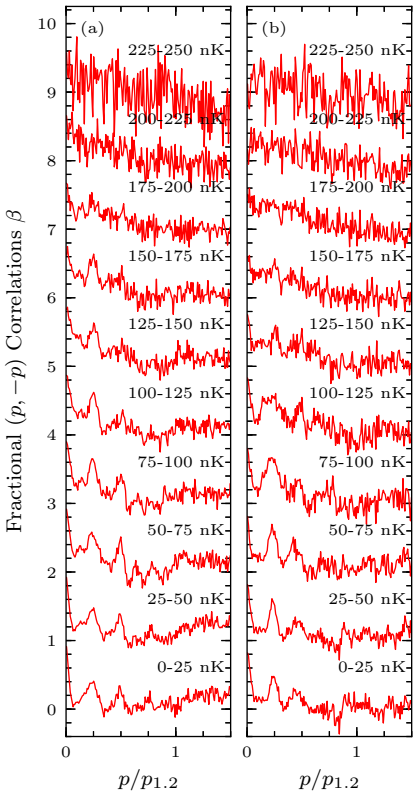

Figure 4.1: Normalized $p, -p$ correlations β for (a) the 2.8-kHz and (b) the deeper 5.6-kHz lattice. In each case fluctuation correlation emerge at lower temperatures than the coherent fraction. Thermal correlations persist to lower temperatures in (b) than (a), despite similar coherent fraction as seen in Fig. B.3. Figure taken from Fig. B.7.

as early as 200 nK. However, momentum fluctuations (shown in Fig. 4.1) in the direction perpendicular to the layers (through the stack) do not emerge until lower temperatures are reached, and $p = 0$ momentum fluctuations are not measurably suppressed until still lower temperatures. This is consistent with moving through the Griffiths phase regions of the phase diagram in that intermediate temperature regime.

As with any experimental publication, this paper was a whole-lab effort to produce and publish. Matt Reed found the original papers that inspired this work. He also designed and assembled the optics portion of the lattice. I conceived of, designed, machined, and assembled the multi-beam interferometer used for phase stabilization, assembled the phase stabilization mirror, designed and assembled the interferometer normalization circuit, and implemented the phase locking loop. I also wrote the computer program used to take a frequency pulse list and program the lattice generation electronics. Matt, Aftaab Dewan, and myself all participated in data taking. Matt did the bulk of the initial analysis, while I provided some single particle lattice simulations. After Matt left I performed a second pass of analysis work. Matt wrote the initial draft of the paper, and all members of the lab participated in editing and refinement.

The remainder of the chapter will discuss further details not covered in the publication itself. Section 3.6 discusses the general RF chain, so we will not discuss it further here. However, the details of the programming for the signal generator depend on the specific application, and thus we present those details below. A final section discusses the single particle simulations mentioned in Sec. B.4.

4.1 Lattice RF Generation

Out lattice generation system outputs synchronized pulses of light at various deflection angles, where the pulses happen quickly enough to form only a time-averaged potential. This presents two difficulties; first, the pulse trains between the AOMs must be synchronized in time, taking into account both electrical and acoustic propagation delays; second, minimizing the effects of the discontinuities of the drive at the boundaries between pulses.

The primary electronic delay occurs in the synchronization of the AWGs. There is a small constant 13 ns delay intrinsic to the follower detecting and acting on incoming clock pulses from the leader. The other possible contribution is differential cable length between the AWGs and their corresponding AOMs. With care this can be eliminated to within a few cm. The speed of light in coaxial cables is $\sim 2/3c$, which corresponds to 50 ps/cm, so the total possible cable delay is much smaller than the jitter of the clock signal itself. Therefore we need only account for the clock propagation delay in the follower.

The acoustic phase delay is due to differing beam positions relative to the AOM's internal transducer-crystal boundary. The density waves propagate at the speed of sound in the medium, which for the longitudinal waves is 4260 m/s, leading to a time delay of ≈230 ns/mm of differential distance from the transducer. For our ∼300 ns pulses this is more than half the total pulse duration, requiring compensation. This also prevents using just the AWG output to calibrate the delay, requiring instead optical measurement.

The total shift from the above affects is offset by cyclically wrapping the pulse program for one of the AWGs. This re-synchronizes the RF that the light sees inside the AOM to within a single clock period of the AWG. In practice, we measure this experimentally by verifying the contrast of a lattice generated by a sequence that is mostly off. By varying the shift to maximize contrast, we find the correct total delay for the system from all sources. A single sequence only synchronizes the system modulo the period of that sequence, but two sequences with incommensurate repetition rates determines fully the delay of the system. This becomes a calibration parameter used for all future pulse programs.

The discontinuity issue is more subtle. Our experiment requires the ability to specify the relative phases of the sublattices, thus discontinuities are necessarily introduced at the pulse edges. Naively, one could select a continuous phase condition for one AOM's drive and apply the phase jumps only to the other. The AWG has no difficulty producing such an output, but the AOMs have mass, and thus their response times are slowed. This "acoustic settling time" will limit the transition time between adjacent pulses. To minimize this effect, the sequences is instead restricted to half-integer multiples of the drive frequency, and the leader and follower each receive half the phase shift applied in different directions. For a sin drive the fixes the magnitude of the phase hop to be the same in each AOM, since

$$\sin(n\pi \pm \phi/2) = \sin(n\pi)\cos(\phi/2) \pm \cos(n\pi)\sin(\phi/2) = \pm\sin(\phi/2). \tag{4.1}$$

4.2 Single Particle Simulations

To verify that the observed effect documented in the paper were due to many-body physics, a simple 1D model generates fluctuations correlations for comparison. Specifically, we experimentally observed correlations at momenta that were not components of the applied optical lattice. If single-particle effects reproduce the observed fluctuations, the sliding phase we claim to observe may not be what is driving them.

The simulation begins by modeling our system as a 1D potential with parameters taken from the measured properties of the lattice and atoms. The sublattice periods and depths are used together with randomly selected phases to generate a disordered potential. The external trapping potential is then added, forming the full 1D potential for the simulation. The discrete variable representation (DVR) method[112] is then used to generate the wavefunctions and eigenenergies for this combined potential.

Having obtained the energies of the bound states of the lattice, we use an iterative procedure to find a self-consistent chemical potential μ for a target total particle number N at a temperature T. We want to include effects from both phase and number fluctuations, so using the mean state populations from the Bose distribution is insufficient. Instead, states are randomly populated using these μ, N, and T with a procedure starting from the related partition function for bosons. This procedure starts from the probability of having n particles in a state with energy ϵ

given the μ and T found earlier,

$$p(n,\epsilon) = \frac{e^{-n(\epsilon-\mu)/k_BT}}{\sum_{n'=0}^{\infty} e^{-n'(\epsilon-\mu)/k_BT}}. \tag{4.2}$$

The cumulative distribution function, *i.e.* the probability that $\leq n$ particles are in the state, is given by summing the this for finite n

$$\mathrm{cdf}(n,\epsilon) = \sum_{n'=0}^{n} p(n',\epsilon). \tag{4.3}$$

Inverting this allow us to draw a random number on $[0,1)$ to select the number of particles in the state following the probability distribution above. This is the mechanism through which number fluctuations are included in the simulation. The inverted distribution is

$$n(p,\epsilon) = \left\lfloor \frac{k_bT}{\epsilon-\mu} \ln\left(\frac{1}{1-p}\right) \right\rfloor, \tag{4.4}$$

where the floor function restricts the occupation to an integer number of particles.

The remainder of the simulation is straightforward. The procedure above populates the states calculated from the DVR before each receives a random phase. The resulting wavefunction is Fourier transformed to obtain the momentum distribution. We repeat this many times before the quantities α and β from App. B are produced for comparison.

4.3 Conclusions

Using both my contributions (above) and those from my colleagues (App. B), we showed evidence that our system exhibited a Griffiths phase region, and that conherence emerges in two transverse directions at different temperatures. These varying temperatures suggest the intermediate phase is a sliding phase, and changing momentum fluctuations agree qualitatively with a proposed mechanism for this phase. These results would greatly benefit from theory collaboration to connect available experimental measurements to prior published theory results.

Chapter 5: Breathing Lattice

In the previous chapter we utilized our apparatus' ability to pulse lattices of many different period to generate disordered layered systems. In this chapter we theoretically explore our ability to continuously varying the amplitude and spacing of the optical lattice. This allows us to generate a "breathing" (or "accordion") lattice. After highlighting our unique ability to realize this system, we will discuss some background before detailing the numerical simulation used to study it. We will then present the results, showing (to our knowledge) the only system where the modulation of a global parameter, the lattice spacing[1], results in a local, site-dependent modulation, in this case a spatial modulation of the tunneling.

Breathing lattices have been used in other ultracold atom experiments[81, 83–89, 113] as a tool for transport or readout, but the spacing changes once as a part of some larger experimental procedure. In contrast, we investigate the breathing optical lattice as the Hamiltonian of interest. Traditional condensed matter systems would have great difficulty producing similar Hamiltonian, as the crystal structures they generate are relatively incompressible. A search of the literature and discussions with colleagues also failed to reveal any existing theoretical or experimental treatment.

[1] As discussed later, there is a modulation of the lattice amplitude, but this serves to fix the depth in units of instantaneous recoil energies, which is the relevant energy scale determining the physics.

Setting up the RF for this system should be quite straightforward, requiring only a power splitter; two frequency sources, one with external amplitude and the other with frequency modulation; and the extant amplifiers. The first frequency source is fixed at the desired breathing frequency, with external computer control setting the amplitude of its output. It connects to the second generator's frequency modulation input. That generator would have its base frequency set to provide the appropriate lattice spacing with external modulation turn off. The periodic modulation from the preceding generator would then cause period modulation of the lattice spacing.

Alternatively, many modern direct digital synthesis (DDS) platforms (including the AD9910 already used at the JQI) allow frequency control via a parallel digital interface. Thus one could easily replace both of the above frequency sources with such a DDS paired with a suitably programmed microcontroller.

There are some subtleties with the geometry of the beams causing nonlinear changes of lattice spacing with frequency, but in the small spacing-drive limit, it can be approximated as linear. In addition, the remainder of the chapter will provide a framework that, although it assumes sinusoidal drive here, can treat the actual form of the drive if necessary. However, we will show that the strong drive amplitude limit requires drive frequencies approaching the natural energy scales of the undriven system, and that will necessarily limit the experimental applicability of that parameter region.

In the remainder of this chapter we will first cover some background on both space- and time-period Hamiltonians. Using that framework we will then discuss the

Hamiltonian for the breathing lattice and the difficulties it presents in solutions in the lab frame. We will then utilize a series of time-dependent unitary transformations to find the effective Hamiltonian in a "co-breathing" coordinate system. In this frame a ficticious anti-trapping term arises, which may partially or fully cancel an external harmonic trap in the time-averaged limit. We then numerically explore this "critical drive" limit within the Floquet formalism presented in Chapter 1, finding the quasi-periodic states and the stroboscopic effective Hamiltonian. Finally future directions both for experimental and theoretical explorations will be suggested.

5.1 Periodic Hamiltonians

When Hamiltonians posses a symmetry, it places restrictions on the possible solutions. For example, Hamiltonians with definite parity have solutions with definite parity. In this section we will first discuss the more familiar case of a Hamiltonian with discrete translational symmetry. Following that discussion we will consider Floquet theory, where the Hamiltonian is periodic in time instead of space.

Spatial Periodicity

Consider a spatially period Hamiltonian, that is

$$H(x) = H(x + a) \tag{5.1}$$

where a is the period. This suggests we introduce the translation operator $\mathcal{R}_a$ that performs such a shift. This operator trivially has the inverse $\mathcal{R}_a^{-1} = \mathcal{R}_{-a}$, commutes

with any other shift by integer multiples of a, and additionally trivially commutes with the Hamiltonian such that

$$[H, \mathcal{R}_a] = 0 \qquad \text{and} \qquad [\mathcal{R}_{na}, \mathcal{R}_{ma}] = 0 \tag{5.2}$$

for integer m, n. This implies that eigenstates of H must simultaneously be eigenstates of $\mathcal{R}_a$. These solutions have the form (in one dimension)

$$\psi(x) = e^{ikx} u_k(x) \tag{5.3}$$

where $u(r)$ has the same period as the Hamiltonian, *i.e.* $u_k(r + a) = u_k(r)$, and k (alternatively q) is the quasimomentum of the Bloch wave. It is worth noting here that the choice of k and $u_k(r)$ corresponding to a Bloch wave are not unique:

$$\psi(x) = e^{ikr}\ e^{imk_a r} e^{-imk_a r}\ u_k(r) = e^{i(k+k_a)r} u_{k+k_a}(r) \tag{5.4}$$

where m in an integer and $k_a = 2\pi/a$. Each pair of k and u_k thus belongs to an infinite class of related k's and u's. A representative of each class can be chosen to such that $-\pi/a \leq k \leq \pi/a$; these form the first Brillouin zone of the lattice. There will be infinitely many solutions with the same quasimomentum, requiring the addition of an additional quantum number, called the "band index" n, to track them.

The preceding holds for a general periodic Hamiltonian, but the sinusoidal

lattice potential is common in experiments

$$H_{\text{latt}} = \left(-\frac{\hbar^2}{2m}\frac{\partial^2}{\partial x^2} + \frac{V_0}{2}\cos(2k_L x) \right) \tag{5.5}$$

For such a potential the Euler's formula suggests we use basis the plane waves as a basis

$$e^{i(k+2jk_L)x} \tag{5.6}$$

where we restrict k to the first Brillouin zone as above. The Hamiltonian with the lattice potential acting on such a state gives

$$H_{\text{latt}} e^{i(k+2jk_l)x} = \frac{\hbar^2(k+2jk_L)^2}{2m} e^{i(k+2jk_l)x} + \frac{V_0}{4}\left(e^{i[k+2(j+1)k_L]x} + e^{i[(k+2(j-1)k_L]x} \right), \tag{5.7}$$

so that the Hamiltonian only couples plane waves differing by multiples of $2k_L$. This form also reveals the natural energy scale for the problem, the recoil energy

$$E_R = \frac{\hbar^2 k_L^2}{2m} = \frac{\hbar^2}{2m}\left(\frac{\pi}{a}\right)^2, \tag{5.8}$$

which is the kinetic energy difference from absorbing one unit of momentum from the lattice. Writing a solution as a superposition of plane waves results in the tridiagonal

matrix equation

$$\begin{bmatrix} \ddots & \ddots & \ddots & & \\ \ddots & (k/k_L+2)^2 & V_{\mathrm{ER}}/4 & 0 & \\ \ddots & V_{\mathrm{ER}}/4 & (k/k_L)^2 & V_{\mathrm{ER}}/4 & \ddots \\ & 0 & V_{\mathrm{ER}}/4 & (k/k_L-2)^2 & \ddots \\ & & \ddots & \ddots & \ddots \end{bmatrix} \begin{bmatrix} \vdots \\ c_{n,1} \\ c_{n,0} \\ c_{n,-1} \\ \vdots \end{bmatrix} = \varepsilon_n \begin{bmatrix} \vdots \\ c_{n,1} \\ c_{n,0} \\ c_{n,-1} \\ \vdots \end{bmatrix} \tag{5.9}$$

where $\varepsilon_n = E_n/E_R$ and E_n is the eigenvalue associated with the state

$$\psi_{n,k} = \sum_j c_{n,j} e^{i(k+2jk_L)x}. \tag{5.10}$$

The set of all $\psi_{n,k}$ forms a complete orthogonal basis set, such that

$$\int \psi^*_{n',k'}(x)\psi_{n,k}(x)dx \propto \delta_{n,n'}\delta_{k,k'} \tag{5.11}$$

and can be normalized over *e.g.* the first Brillouin zone.

The sinusoidal optical lattice Hamiltonian is equivalent to Mathieu's equations[114, Ch. 28] and has solutions known as the Mathieu functions. Their properties are well understood, including asymptotic forms for various limits, so this can be an attractive approach to examining the behavior of these systems. However, the matrix equation can be approximately solved by any standard matrix diagonalization routine by truncating the matrix. Such results are shown in Fig. 5.1.

In the limit $V_{\mathrm{ER}} = 0$ we recover the free-particle solution, which is gapless and

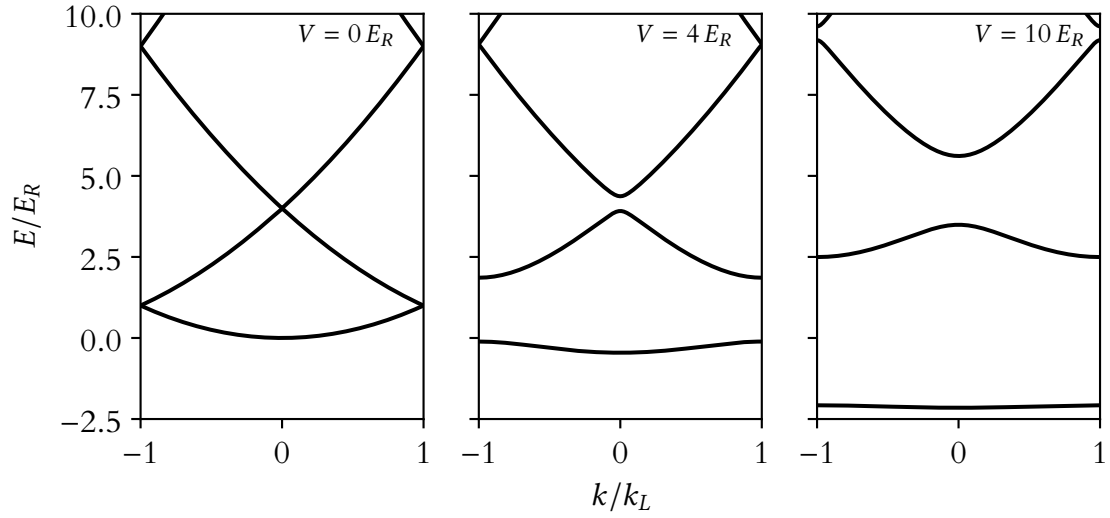

Figure 5.1: Band structure diagrams for a sinusoidal lattice for a few lattice depths. In the free particle limit (left) the system is gapless, but as the depth of the lattice increase to $4E_R$ (middle) and then $10E_R$ (right) gaps open at the band edges.

has the expected quadratic shape for the energy, folded into the Brillouin zone. For small but finite values of V_{ER} gaps begin to open at the band edges, as shown in Fig. 5.1, widening as V_{ER} increases. Now the the meaning of "band index" is plain; it indicates which of these energy bands a state belongs to.

The Bloch wavefunctions are delocalized over the entire lattice, but they can combine to construct the Wannier functions[115–118]. The function for the nth band localized around site j is

$$w_n(x - x_j) = \int_{BZ} u_{n,k} e^{-ikx_j} dk, \tag{5.12}$$

where the integral is over all k in the first Brillouin zone, and care must be taken with the phases of $u_{n,k}$. Kohn showed[116] that for each band the phases can be chosen to construct w_n to be simultaneously real and exponentially localized around

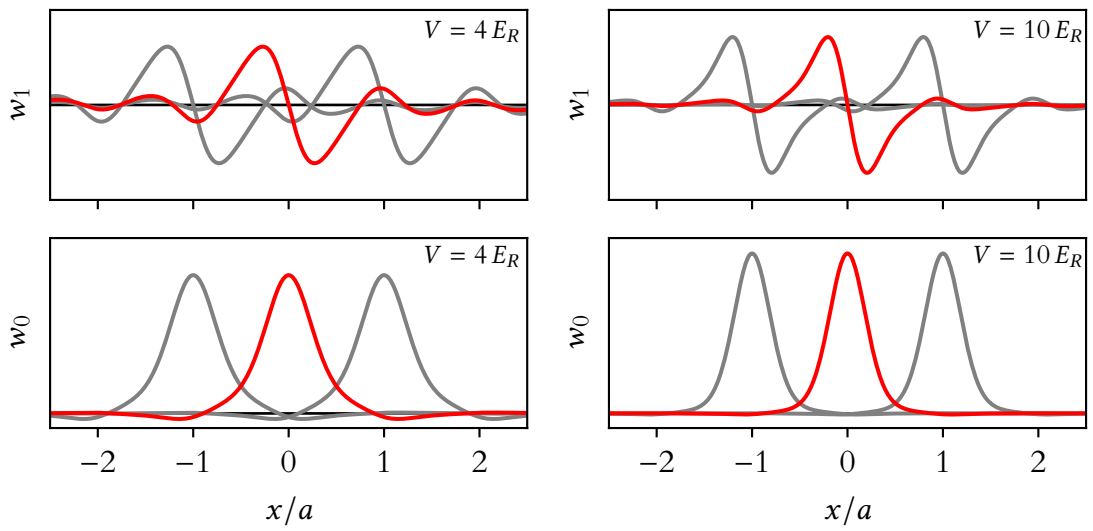

Figure 5.2: Wannier states corresponding to the lattices from Fig. 5.1. The red traces are w_1 (top) and w_0 (bottom) centered on $x = 0$, and the grey traces are those same states centered on adjacent lattice sites.

the appropriate site, and that this choice uniquely maximally localizes the states. Wannier function for the first and second band are shown in Fig. 5.2. The set of Wannier functions at each lattice site in a band form a complete orthonormal basis for that band, implying the set of all Wannier functions in all bands is an orthonormal basis set for all states.

Before moving on, we should point out that despite this discussion's focus on 1D sinusoidal lattice potentials, the matrix technique for finding eigenstates and the existence of both band structure and Wannier functions is easily extensible both to higher dimensions and more complicated periodic potentials. For instance, the plane wave basis can accommodate plane waves in two orthogonal directions to form a basis for a 2D lattice, or the Fourier series expansion of the potential provides additional entries on further diagonals of the matrix.

Since both the Bloch waves and the Wannier functions form orthonormal basis

sets, we now have two equivalent ways to write the original lattice Hamiltonian Eq. (5.5):

$$H_{\text{latt}} = \sum_{n,k \in BZ} E_{n,k} b^{\dagger}_{n,k} b_{n,k} \tag{5.13}$$

$$= -\sum_{n,i,j} J_{i,j} a^{\dagger}_{n,i} a_{n,j} \tag{5.14}$$

where the first line is merely the eigenfuction decomposition expressed in terms of the creation and annihilation operator for a particle for the Bloch functions. The second line's $a^{\dagger}$ and a work in the Wannier basis, and $J_{i,j}$ determines the coupling between sites i and j. Note no interband couplings exist even in the Wannier basis, because the Wannier functions for a band are a complete basis for that band, and the Bloch functions for different bands are orthogonal.

At this point various simplifying assumptions are possible. For sufficiently low temperatures and densities, atoms loaded in the lattice only occupy the lowest band. Thus terms for $n > 0$ may be neglected. Further, for deep lattice the Wannier functions fall off so quickly that only the nearest-neighbor couplings are appreciable, that is $J_{i,j} = J$ for $|i - j| = 1$ and 0 otherwise. Together these form a tight-binding model, described by the Hamiltonian

$$H_{TB} = -J \sum_{\langle i,j \rangle} a^{\dagger}_i a_j \tag{5.15}$$

where $\langle i, j \rangle$ indicates the sum is over all nearest-neighbor pairs.

Temporal Periodicity and Floquet's Theorem

Note: Many sources cover general Floquet theory, and much of the discussion here draws from [119–121]. Because they frequently overlap in content, rather than select citations point by point, we cite a particular reference only when especially relevant.

Consider a time-periodic Hamiltonian, such that $H(t) = H(t+T)$ where T is the period. Floquet's theorem implies that the time-dependent Schrodinger equation (TDSE) with such a Hamiltonian admits quasiperiodic solutions, that is, solutions of the form

$$|\psi_n(t)\rangle = e^{-i\epsilon_n t/\hbar} |u_n(t)\rangle \tag{5.16}$$

where the $|u_n(t)\rangle$ have the same periodicity as the Hamiltonian

$$|u_n(t+T)\rangle = |u_n(t)\rangle \,. \tag{5.17}$$

This has two significant implications; first, the periodic nature of the Hamiltonian does not guarantee periodic behavior of the wavefunction. Indeed, for a superposition of states with irrational ratio of ϵ's will never evolve back to its initial wavefunction. Second, the short-time dynamics decouple from the long-time dynamics, the former determined by the $u_n(t)$ while the latter by the quasienergies ϵ_n. Specifically at stroboscopic times $t = nT$ for integer n, the periodic nature of $u_n(t)$ implies that only the relative dephasing of Floquet states due to differing ϵ_n is apparent. This will be explored mathematically in the following paragraphs.

Substituting Eq. (5.16) into the TDSE gives the result

$$
\begin{aligned}
i\hbar\frac{d}{dt}\left(e^{-i\epsilon_n t/\hbar}\left|u_n\right\rangle\right) &= H\left(e^{-i\epsilon_n t/\hbar}\left|u_n\right\rangle\right) \\
\epsilon_n e^{-i\epsilon_n t/\hbar}\left|u_n\right\rangle + i\hbar e^{-i\epsilon_n t/\hbar}\frac{d}{dt}\left|u_n\right\rangle &= e^{-i\epsilon_n t/\hbar}H\left|u_n\right\rangle \\
\epsilon_n\left|u_n\right\rangle &= \left(H - i\hbar\frac{d}{dt}\right)\left|u_n\right\rangle . \qquad (5.18)
\end{aligned}
$$

Identifying the right side of this expression as

$$
K = H - i\hbar\frac{d}{dt}, \qquad (5.19)
$$

we see that the quasienergy ϵ_n is an eigenvalue of K. Less obviously, these quasienergies are only defined up to multiples of $\hbar\Omega$ (using the usual definition $T = 2\pi/\Omega$. This can be demonstrated by

$$
\begin{aligned}
\left(H - i\hbar\frac{d}{dt}\right)\left(e^{im\Omega t}\left|u_n\right\rangle\right) &= \left[(m\hbar\Omega)e^{im\Omega t}\left|u_n\right\rangle\right] + e^{im\Omega t}\left(H - i\hbar\frac{d}{dt}\right)\left|u_n\right\rangle \\
&= \left[(m\hbar\Omega)e^{im\Omega t}\left|u_n\right\rangle\right] + e^{im\Omega t}\epsilon_n\left|u_n\right\rangle \\
&= (\epsilon_n + m\hbar\Omega)e^{im\Omega t}\left|u_n\right\rangle , \qquad (5.20)
\end{aligned}
$$

which suggests the definition $\epsilon_{nm} = \epsilon_n + m\hbar\Omega$. Taking that together with Eq. (5.16),

one can write

$$\begin{aligned} |\psi_{nm}\rangle &= e^{-i\epsilon_{nm}t/\hbar}\left(e^{im\Omega t}\,|u_n\rangle\right) \\ &= e^{-i\epsilon_n t/\hbar}e^{-im\Omega t}e^{im\Omega t}\,|u_n\rangle \\ &= e^{-i\epsilon_n t/\hbar}\,|u_n\rangle = |\psi_n\rangle\,, \end{aligned} \tag{5.21}$$

that is, $|\psi_{nm}\rangle$ and $|\psi_n\rangle = |\psi_{n0}\rangle$ represent the *same* Floquet state, but their eigenvalues can differ by integer multiples of $\hbar\Omega$.

Returning to the eigenvalue equation from Eq. (5.18), we can consider this in an extended Hilbert space[122, 123] where time is just a coordinate (and not an evolution variable). That is, if $\mathcal{H}$ is the space spanned by the original Hamiltonian and $\mathcal{T}(T)$ is the space of T-periodic square-integrable functions, we can consider the problem the space $\mathcal{F} = \mathcal{H} \otimes \mathcal{T}(T)$. In this space the inner product is

$$\frac{1}{T}\int_0^T \langle\cdot|\,|\cdot\rangle\,dt. \tag{5.22}$$

For some orthonormal basis set in $\mathcal{H}$, $\{|0\rangle\,,\ldots,|n\rangle\}$, this inner product trivially maintains the orthonormality. The Fourier exponentials form a complete orthonormal basis for the time-coordinate, and we can combine these to form our states

$$|\alpha m\rangle\!\rangle = e^{im\Omega t}\,|\alpha\rangle\,. \tag{5.23}$$

For the inner product given above, then

$$\langle\langle \alpha m| \, |\beta p\rangle\rangle = \frac{1}{T}\int_0^T \langle\alpha| \, e^{-im\Omega t} e^{ip\Omega t} \, |\beta\rangle = \frac{1}{T}\int_0^T e^{i(p-m)\Omega t} \, \langle\alpha| \, |\beta\rangle \tag{5.24}$$

$$= \delta_{\alpha,\beta}\delta_{m,p}. \tag{5.25}$$

K acting in this basis is then

$$K \, |\alpha m\rangle\rangle = He^{im\Omega t} \, |\alpha\rangle - i\hbar \frac{d}{dt} e^{im\Omega t} \, |\alpha\rangle = He^{im\Omega t} \, |\alpha\rangle + m\hbar\Omega \, |\alpha\rangle \, ,$$

which means the matrix elements for K are

$$\langle\langle \beta p| \, K \, |\alpha m\rangle\rangle = \langle\beta| \, H_{p-m} \, |\alpha\rangle \, \delta_{p,m} + m\hbar\Omega\delta_{p,m} \, \langle\beta| \, |\alpha\rangle \, , \tag{5.26}$$

where H_ℓ stands for the ℓ^{th} Fourier component of the Hamiltonian operator.

Having found a matrix representation for K, if diagonalized, its eigenvectors and associated eigenvalues can be obtained. Through Eq. (5.18) we have thus identified the quasienergies and periodic components of the Floquet states. These can then be combined via Eq. (5.16) to write down the full Floquet state, and thus have access to the evolution of the system.

5.2 Time-dependent Unitary Transformations

Occasionally the time-dependence of a system, though periodic, is not easily computable in its original form. In these cases it is sometimes useful to make a

time-dependent unitary transformation of the Hamiltonian such that the physics becomes more simple to express. For instance, to solve the periodically shaken optical lattice we transform to the "co-moving frame", trading a time-dependent lattice potential for a uniform on-site time dependent force. The time dependence of the transformation introduces some extra terms, as we show in general below.

The TDSE describes the dynamics of a state $|\Psi\rangle$ under the influence of the Hamiltonian operator H, and is

$$i\hbar\frac{d}{dt}|\Psi\rangle = H|\Psi\rangle\,, \tag{5.27}$$

where both H and $|\Psi\rangle$ may carry time dependence. It is sometimes convenient, because the form of either (or both) is difficult computationally, to make a formal transformation to a related Hamiltonian H' acting on a new state $|\Psi'\rangle$. The transformation must be norm-preserving, which restricts us to using a unitary operator U. The class of operations we are considering are called unitary transformations, and we find our desired transformation by inserting the identity and premultiplying by U in Eq. (5.27).

$$\begin{aligned} U i\hbar\frac{d}{dt}|\Psi\rangle &= UHU^\dagger U|\Psi\rangle \\ i\hbar\left[\frac{d}{dt}\left(U|\Psi\rangle\right) - \frac{dU}{dt}|\Psi\rangle\right] &= UHU^\dagger U|\Psi\rangle \\ i\hbar\frac{d}{dt}(U|\Psi\rangle) &= \left(UHU^\dagger + i\hbar\dot{U}U^\dagger\right)(U|\Psi\rangle) \end{aligned} \tag{5.28}$$

which is the TDSE again, but after the desired transformation

$$i\hbar\frac{d}{dt}\left|\Psi\right\rangle = H\left|\Psi\right\rangle \rightarrow i\hbar\frac{d}{dt}\left|\Psi'\right\rangle = H'\left|\Psi'\right\rangle$$
$$H' = UHU^{\dagger} + i\hbar\dot{U}U^{\dagger} \quad \left|\Psi'\right\rangle = U\left|\Psi\right\rangle . \tag{5.29}$$

Note that while a time-independent unitary will transform the same way as any other operator, a time-dependent one gives rise to another term in the new effective Hamiltonian.

Once the transformed problem is solved, it is trivial to recover the untransformed wavefunction by applying $U^{\dagger}$. Further, expectation values for operators in the original are easily computed. For example a generic operator O has an expectation value

$$\left\langle\Psi\right| O\left|\Psi\right\rangle = \left\langle\Psi\right| U^{\dagger}UOU^{\dagger}U\left|\Psi\right\rangle = \left\langle\Psi'\right| O'\left|\Psi'\right\rangle . \tag{5.30}$$

5.3 Breathing Hamiltonian

The single-particle Hamiltonian for atoms in a breathing lattice has the form

$$H = \frac{p^2}{2m} + \left(\frac{k(t)}{k_0}\right)^2 V_0 \cos\left(k(t)x\right) \tag{5.31}$$

and the specific form of the time-varying spacing is

$$k(t) = k_0\left[1 + \gamma\cos(\Omega t)\right] \tag{5.32}$$

where k_0 gives the mean potential k-vector, γ the amplitude of the variation, Ω the drive frequency, and V_0 the potential depth. The additional factor of $[k(t)/k_0]^2$ fixes the lattice depth in lattice recoil energies constant, isolating any effects from the breathing from amplitude-modulation based modification of the tunneling.

This form for the Hamiltonian is particularly unfriendly to deal with. The temporally-varying period of the lattice prevents the decoupling into separate subspaces. This can be made more explicit by expanding the cosine term and invoking the Jacobi-Anger identity for each resulting term:

$$\begin{aligned}
&\cos[k_0(1+\gamma\cos(\Omega t))x] \\
&\quad = \cos(k_0 x)\cos\left[\gamma k_0 x\cos(\Omega t)\right] - \sin(k_0 x)\sin\left[\gamma k_0 x\cos(\Omega t)\right] \qquad (5.33)\\
&\quad = \cos(k_0 x)\left[\mathcal{J}_0(\gamma k_0 x) + 2\sum_{n=1}^{\infty}(-1)^n\mathcal{J}_{2n}(\gamma k_0 x)\cos(2n\Omega t)\right] \\
&\qquad + 2\sin(k_0 x)\sum_{n=1}^{\infty}(-1)^n\mathcal{J}_{2n-1}(\gamma k_0 x)\cos\left[(2n-1)\Omega t\right]. \qquad (5.34)
\end{aligned}$$

While Bessel functions often arise as *solutions* to problems, they are not well-studied as forms for a potential. Ordinarily plane waves are used as a basis for problems related to a lattice, but here the $\mathcal{J}_n$ have a continuous (though still compact) Fourier transform, as shown in Fig. 5.3. It is expressed as

$$\mathcal{F}(\mathcal{J}_n) = \sqrt{\frac{2}{\pi}}\frac{(-i)^n T_n(k)\,\mathrm{rect}(k/2)}{\sqrt{1-k^2}}. \qquad (5.35)$$

where $\mathrm{rect}(x)$ is 1 for $|x| < 1/2$, 1/2 for $|t| = 1/2$, and 0 otherwise, and T_n are the Chebyshev polynomials[114, Ch. 18]. This causes individual plane waves to couple

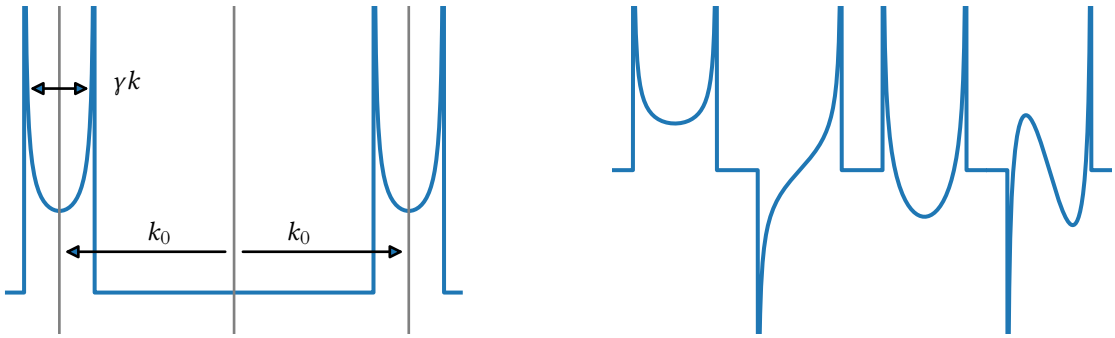

Figure 5.3: The Fourier transform of the time-averaged term of the potential is show to the left. The width of each portion is γk_0 and are centered around $\pm k_0$. To the right are the Fourier transforms of (from left to right) $\mathcal{J}_0$ through $\mathcal{J}_3$, illustrating they each approach $\pm\infty$ at the edges of the nonzero region.

to a continuous range of plane waves, which keeps the systems from decoupling into quasimomentum manifolds as it would for a static lattice, even in the time-averaged limit.

The finite extent in momentum space suggests basis states that are similarly compact in momentum space. For instance the Legendre polynomials[114, Ch. 18] $P_n(x)$ form an orthogonal basis for $-1 \leq x \leq 1$, and may be suitable scaled and shifted to form a complete orthonormal basis for all momentum space. However, the convolution (as occurs in the Schrodinger equation (SE) in momentum space) of $T_n(x)$ and $P_m(x)$ does not have a simple expression. Methods to convolve $P_m(x)$ amongst themselves exist[124], but would require the above Fourier transform to be written as a series in P_m, which is non-trivial because of the radical in the denominator. The Chebyshev polynomials are orthogonal with respect to a weight function that we must include with the states if want to use them as an orthonormal basis to span the space. This complicates the use of recursion formulas within the polynomial family, as now the weight function will also need to be written as a Chebyshev series. These

difficulties suggested we take a different approach toward investigating this system.

5.4 Effective Hamiltonian

Dilation

The first transformation we make is a dilation $\mathcal{D}_\kappa$ chosen to stretch synchronously with the changing lattice spacing. It is defined as

$$\mathcal{D}_\kappa = \exp\left[\frac{i}{\hbar}\ln(\kappa)\frac{xp+px}{2}\right] \tag{5.36}$$

where κ is a (possibly time-dependent) scale factor. To find the transformed Hamiltonian we'll need to find how $\mathcal{D}_\kappa$ acts on x and p, in addition to the time derivative.

$$\mathcal{D}_\kappa x \mathcal{D}_\kappa^\dagger = \kappa x \tag{5.37}$$

$$\mathcal{D}_\kappa p \mathcal{D}_\kappa^\dagger = \frac{p}{\kappa} \tag{5.38}$$

$$\dot{\mathcal{D}}_\kappa \mathcal{D}_\kappa^\dagger = \frac{i}{\hbar}\frac{\dot{\kappa}}{\kappa}\frac{xp+px}{2} \tag{5.39}$$

This yields the transformed Hamiltonian

$$H' = \frac{p^2}{2m\kappa^2} + \left(\frac{k(t)}{k_0}\right)^2 V_0 \cos\left(k(t)\kappa x\right) - \frac{\dot{\kappa}}{\kappa}\frac{xp+px}{2} \tag{5.40}$$

which becomes, after completing the square,

$$H' = \frac{(p - m\dot{\kappa}\kappa x)^2}{2m\kappa^2} + \left(\frac{k(t)}{k_0}\right)^2 V_0 \cos\left(k(t)\kappa x\right) - \frac{1}{2}m\dot{\kappa}^2 x^2. \tag{5.41}$$

x-Dependent Momentum Shift

The preceding dilation operation compensates for the shifting optical lattice, whose specific form we'll discuss later. It also leaves a position-dependent momentum shift corresponding to the momentum required to move with the stretching lattice. We define a unitary operator

$$\Upsilon_\alpha = \exp\left(-\frac{i}{\hbar}\alpha\frac{x^2}{2}\right) \tag{5.42}$$

where α is some x-independent (but possibly time-dependent) factor determining the magnitude of the shift. Using

$$[p, \Upsilon_\alpha] = -i\hbar\partial_x\Upsilon_\alpha = -\alpha x\Upsilon_\alpha \tag{5.43}$$

we can show

$$\Upsilon_\alpha x\Upsilon_\alpha^\dagger = x \tag{5.44}$$

$$\Upsilon_\alpha p\Upsilon_\alpha^\dagger = (p + \alpha x) \tag{5.45}$$

$$\dot{\Upsilon}_\alpha\Upsilon_\alpha^\dagger = -\frac{i}{\hbar}\frac{\dot{\alpha}}{2}x^2 \tag{5.46}$$

For our case we take $\alpha = m\dot{\kappa}\kappa$, yielding

$$H'' = \frac{p^2}{2m\kappa^2} + \left(\frac{k(t)}{k_0}\right)^2 V_0\cos(k(t)\kappa x) + \frac{1}{2}m\kappa\ddot{\kappa}x^2 \tag{5.47}$$

Thus far we have avoided giving an explicit form for κ, but to proceed further we must do so. To produce a lattice with static spacing it must have the form $\kappa = k_{\text{eff}}/k(t)$, but there is some additional freedom available in the choice of k_{eff}. One option would be to set it to be k_0, the mean lattice spacing, but the factor of κ^{-2} on the kinetic energy term leads us to make another choice:

$$\kappa = \frac{k_0\sqrt{1+\gamma^2/2}}{k(t)} = \frac{\sqrt{1+\gamma^2/2}}{1+\gamma\cos(\Omega t)}. \tag{5.48}$$

This form conveniently results in

$$\kappa^{-2} = 1 + \frac{4\gamma}{2+\gamma^2}\cos(\Omega t) + \frac{\gamma^2}{2+\gamma^2}\cos(2\Omega t)\,, \tag{5.49}$$

which has unity for the constant term. Substituting Eq. (5.48) into Eq. (5.47) yields the final form for the transformed Hamiltonian.

$$\begin{aligned} H'' &= \frac{1}{\kappa^2}\left[\frac{p^2}{2m} + V_\gamma\cos(k_{\text{eff}}x)\right] + \frac{1}{2}m\kappa\ddot{\kappa}x^2 \\ V_\gamma &= \left(1+\frac{\gamma^2}{2}\right)V_0 \quad k_{\text{eff}} = \sqrt{1+\frac{\gamma^2}{2}}k_0 \end{aligned} \tag{5.50}$$

Effective Harmonic Potential

The effective harmonic potential turns out to time-average to be anti-trapping for all drive strengths and frequencies. To see this, consider that κ is an even periodic

function, and thus can be written as a Fourier series with real coefficients

$$\kappa = \sum_n \kappa_n e^{in\Omega t} \qquad \kappa_n = \kappa_{-n}, \tag{5.51}$$

and thus the second time derivative is

$$\ddot{\kappa} = -\Omega^2 \sum_n \kappa_n n^2 e^{in\Omega t}. \tag{5.52}$$

The product $\kappa\ddot{\kappa}$ can be written as the product of the two series

$$\kappa\ddot{\kappa} = \left(\sum_{n'} \kappa_{n'} e^{in'\Omega t}\right)\left(-\Omega^2 \sum_n \kappa_n n^2 e^{in\Omega t}\right) \tag{5.53}$$

$$= -\Omega^2 \sum_{m,\Delta_m} \kappa_{-\Delta_m}\kappa_{m+\Delta_m}(m+\Delta_m)^2 e^{im\Omega t}. \tag{5.54}$$

This form suggests we write the product as

$$\kappa\ddot{\kappa} = -\Omega^2\Xi = -\Omega^2 \sum_n \Xi_n e^{in\Omega t} \tag{5.55}$$

$$\Xi_n = \sum_{\Delta_n} \kappa_{-\Delta_n}\kappa_{n+\Delta_n}(n+\Delta_n)^2 \tag{5.56}$$

In this form it is easy to see that the time-averaged term (corresponding to $n = 0$)

$$-\Omega^2\Xi_0 = -\Omega^2 \sum_{\Delta_n} \kappa_{\Delta_n}^2 \Delta_n^2 \tag{5.57}$$

is trivially always negative, being a negative value times the sum of strictly positive terms. Without the addition of some external trap, this would cause all atoms in the

system to run towards the edges. Fortunately, there is an external harmonic trap present experimentally with trapping frequency ω_T. We can add this term to our effective Hamiltonian. While this trap is static in the lab frame, in our transformed frame it carries its own time depenence. Performing the same transformations yields

$$V_{\text{ext}} = \Upsilon_{m\kappa\dot{\kappa}} \mathcal{D}_\kappa \left(\frac{1}{2} m\omega_T^2 x^2 \right) \mathcal{D}_\kappa^\dagger \Upsilon_{m\kappa\dot{\kappa}}^\dagger = \frac{1}{2} m\omega_T^2 \kappa^2 x^2. \tag{5.58}$$

Adding this term to Eq. (5.50) produces

$$H''' = \frac{1}{\kappa^2} \left[\frac{p^2}{2m} + V_\gamma \cos(k_{\text{eff}} x) \right] + \frac{1}{2} m(\omega_T^2 \kappa^2 + \kappa\ddot{\kappa}) x^2. \tag{5.59}$$

In this form, all the time dependence is carried by combinations of κ and its time derivatives. We anticipate using the Fourier components of this Hamiltonian in the Floquet extended-zone formalism, so isolating time-dependent parts will help illuminate the relevant Floquet couplings. To ease notation, the relevant combinations will be represented by their own symbols, one of which was already introduced above. For our chosen harmonic modulation of the spacing, these are:

$$\chi = \frac{1}{\kappa^2} = \frac{[1 + \gamma \cos(\Omega t)]^2}{1 + \gamma^2/2} \tag{5.60}$$

$$\xi = \kappa^2 = \frac{1 + \gamma^2/2}{[1 + \gamma \cos(\Omega t)]^2} \tag{5.61}$$

$$\Xi = -\frac{\kappa\ddot{\kappa}}{\Omega^2} = -(1 + \gamma^2/2) \frac{[2\gamma^2 + \gamma \cos(\Omega t) + \gamma^2 \cos^2(\Omega t)]}{[1 + \gamma \cos(\Omega t)]^4} \tag{5.62}$$

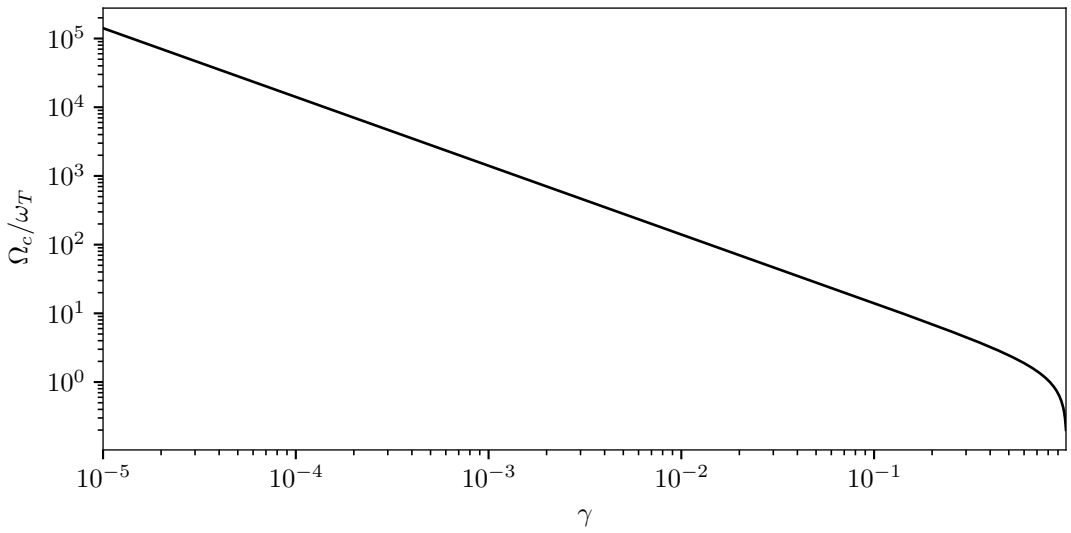

Figure 5.4: The ratio of the critical drive frequency Ω_c to the external trap frequency ω_T for a given breathing amplitude γ.

We then can rewrite our effective Hamiltonian as

$$H''' = \chi\left[\frac{p^2}{2m} + V_\gamma \cos(k_{\text{eff}}x)\right] + \frac{1}{2}m(\xi\omega_T^2 - \Xi\Omega^2)x^2. \tag{5.63}$$

i

One can also find the critical drive frequency Ω_c at which the time-averaged trap vanishes

$$\Omega_c = \frac{\sqrt{2(1-\gamma^2)}}{\gamma}\omega_T. \tag{5.64}$$

For faster drives than this, the time averaged potential becomes anti-trapping, which suggests that, for drives fast enough to reach the time averaged limit, atoms will be forcibly ejected from the center of the trap. Of course Eq. (5.64) can be inverted to find the critical drive amplitude γ_c that will cancel the trap for some fixed drive

frequency Ω:

$$\gamma_c = \frac{1}{\sqrt{1 + \frac{1}{2}\left(\frac{\Omega}{\omega}\right)^2}}. \tag{5.65}$$

These are plotted in the left side of Fig. 5.4. The right side shows the scaling of the harmonic trapping term with γ; Ξ and ξ are discussed further in the next section.

5.5 Floquet Approach

We will require the Fourier components for the various parts of the potential, which have been derived in App. C. We only require the exponential version (as opposed to the trigonometric version)

$$f(t) = \sum_{n=-infty}^{\infty} e^{in\Omega t}, \quad f_n = \frac{\Omega}{2\pi}\int_{-\pi/\Omega}^{\pi/\Omega} f(t)e^{-in\Omega t}\,dt \tag{5.66}$$

and for our chosen drive all the time-varying functions are even, so $f_n = f_{-n}$. The terms for each function are as follows:

$$\chi_0 = 1, \quad \chi_1 = \frac{2\sqrt{1-y^2}}{3-y^2}, \quad \chi_2 = \frac{1-y^2}{2(3-y^2)}, \quad \chi_{n\geq 3} = 0 \tag{5.67}$$

$$\xi_n = (-1)^n(1+ny)\frac{3-y^2}{2y^3}\left(\frac{1-y}{1+y}\right)^{n/2} \tag{5.68}$$

$$\Xi_n = (-1)^n\frac{3-y^2}{12y^5}\left(\frac{1-y}{1+y}\right)^{n/2}\left[3+3ny+3(n^2-1)y^2+2n(n^2-1)y^3\right] \tag{5.69}$$

$$y = \sqrt{1-\gamma^2}, \tag{5.70}$$

where y was introduced to ease the notation of ξ and Ξ. These expressions are derived in App. C.

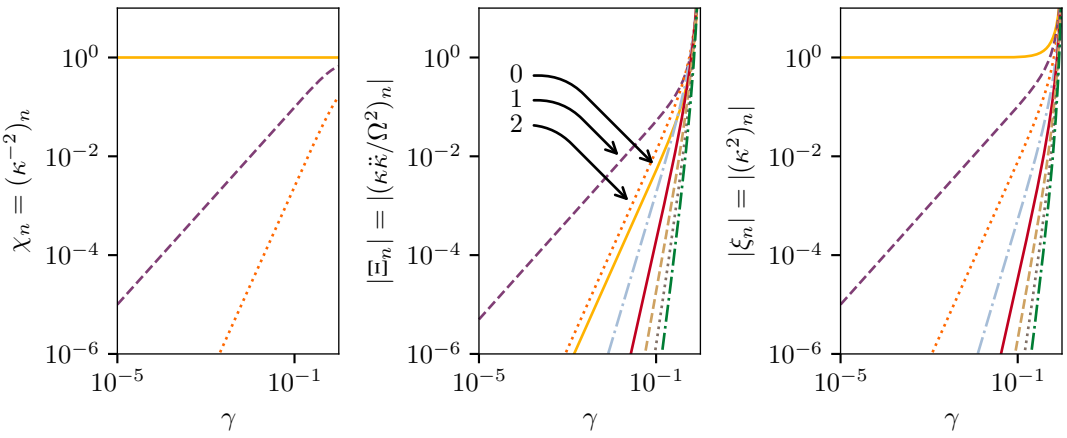

Figure 5.5: The magnitudes of the Fourier components of the drive, as described in the text. Note that, for Ξ the 0th order term is suppressed to the level of the 2nd order term, leaving the 1st order term as the leading contribution to the function. All components fall off quickly in the range of γ chosen, scaling as $f_n \approx \gamma^n$.

While not obvious in this form, the magnitudes of the higher-frequency components of ξ and Ξ fall off quite quickly. These magnitude are plotted in Fig. 5.5, but to make this more explicit, a power series may be constructed for the n^{th} term of the Fourier series. The leading terms are:

$$\xi_n = \left(-\frac{1}{2}\right)^n (n+1)\,\gamma^n + O\left(\gamma^{n+2}\right) \tag{5.71}$$

$$\Xi_0 = \gamma^2 + O\left(\gamma^4\right) \tag{5.72}$$

$$\Xi_{n>0} = \left(-\frac{1}{2}\right)^n \frac{(n+3n^2+2n^3)}{6}\,\gamma^n + O\left(\gamma^{n+2}\right). \tag{5.73}$$

Since the first sub-leading order terms is smaller by γ^2 relative to the leading term, this captures almost all the behavior for the small-γ limit that will be experimentally relevant.

As noted above, a critical drive frequency exists at which the effective anti-

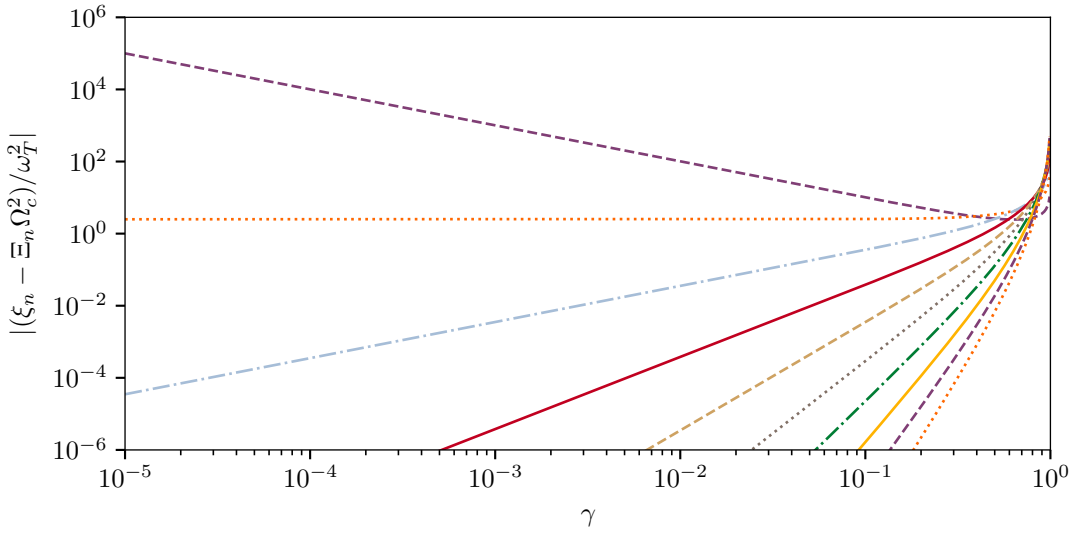

Figure 5.6: The scaling of the remaining quadratic in space terms with $\Omega = \Omega_c$ chosen to cancel the time-averaged harmonic trap. The 0th term has been canceled, so the largest is the $n = 1$ dashed purple curve. The remaining terms decrease in magnitude for small values of γ, so one may count along the outer edge of the plot to identify any other desired amplitude.

confinement from the drive can exactly cancel the external trap when averaged over a full driving period. Shown in Fig. 5.6 is the combined higher-order terms that are quadratic in space for such a drive. Note that the leading order term is very large for small γ.

With these components in hand, we need only determine the basis set $|n\rangle$. One natural approach would use Rey et al.'s result[125] for a tight binding model for a sinusoidal lattice plus a harmonic external confinement. This would provide a convenient basis to use for typical, unmodified external trapping potentials, however, we will want to also explore the critical drive limit. In that limit at least the time averaged terms will have no harmonic confinements, and for that case such a basis is difficult to form. We will still follow the general approach, forming a tight binding

model in the co-breathing space before diagonalizing the system.

First, we insert offsetting terms into the $-$2nd through the 2nd terms to allow us to write H''' as five terms proportional to the time averaged term plus a sum of harmonic trapping terms. Explicitly (and dropping the primes from Eq. (5.59)),

$$\begin{aligned} H &= \chi\left[\frac{p^2}{2m} + V_\gamma\cos(k_{\text{eff}}x)\right] + \frac{1}{2}m\left(\xi\omega_T^2 - \Xi\Omega^2\right)x^2 \\ &= \chi\left[\frac{p^2}{2m} + V_\gamma\cos(k_{\text{eff}}x)\right] + \sum_n \frac{1}{2}m\left[\xi_n\omega_T^2 - \Xi_n\Omega^2\right]x^2 e^{in\Omega t} \\ &= \chi\left[\frac{p^2}{2m} + V_\gamma\cos(k_{\text{eff}}x) + \frac{1}{2}m\left(\xi_0\omega_T^2 - \Xi_0\Omega^2\right)x^2\right] \\ &\quad + \sum_{n\neq 0}\frac{1}{2}m\left[\left(\xi_n\omega_T^2 - \Xi_n\Omega^2\right) - \chi_n\left(\xi_0\omega_T^2 - \Xi_0\Omega^2\right)\right]x^2 e^{in\Omega t} \end{aligned} \tag{5.74}$$

where we've left the time dependence of χ of the first line implicit for the time being.

This form makes the general structure of the problem more apparent. The χ term describes a static lattice plus harmonic trap for our original atom, but the *overall* energy scale is oscillating in time. The sum describes couplings from a time-varying harmonic potential. The bracketed term can go to zero for special values of the drive, and because ξ_n and Ξ_n both scale as γ^n we can almost entirely suppress the sum by balancing just the $n = 1$ term. The drive frequency that accomplishes this decoupling is

$$\Omega_d = \sqrt{\frac{(1-\gamma^2)(4+\gamma^2)}{1+\frac{3}{2}\gamma^2}}\omega_T, \tag{5.75}$$

which has a maximum of $2\omega_T$. This puts it, generally, at much lower frequencies than an experimentalist would like to drive. For example in our system $\omega_T/2\pi = 20\,\text{Hz}$, meaning the shorted drive period is 25 ms. In additional to restricting the total

number of drive periods possible in an experimental cycle, this places the drive energy scales close to other energy scales already in the problem, meaning the single-band approximation we'll be making in our tight binding model will likely be violated. We will not discuss this decoupling frequency any further.

Instead, we will move forward with the tight binding model. For this the lattice and kinetic terms will form the hopping potential, and the harmonic trap will become an on-site energy offset. That is,

$$H_0 = \frac{p^2}{2m} + V_\gamma \cos(k_{\text{eff}} x) + \frac{1}{2} m \left(\xi_0 \omega_T^2 - \Xi_0 \Omega^2\right) x^2 \tag{5.76}$$

$$\Downarrow$$

$$H_{tb} = -J \sum_j (a_j^\dagger a_{j+1} + a_{j+1}^\dagger a_j) + \Theta j^2 n_j \tag{5.77}$$

$$\Theta = \frac{1}{2} m \left(\frac{2\pi}{k_{\text{eff}}}\right)^2 \left(\xi_0 \omega_T^2 - \Xi_0 \Omega^2\right) \tag{5.78}$$

where j indexes lattice sites, with $j = 0$ corresponding to the site at the bottom of the potential well, and a_j, $a_j^\dagger$, and n_j are the creation, annihilation, and number operators at site j. J is the usual tunneling amplitude, which depends on the depth of the lattice in recoil energies. Doing similar transformations on the rest of the Fourier components proceeds similarly. Putting this all together gives the matrix form for our K in the extended Hilbert space scheme.

There are some complications in determining where exactly the high-frequency and single-band approximation limits are in our system. The remainder of this work will press forward with each, leaving an exploration of these limits for future work.

5.6 Numerics

The extended Hilbert space method will produce a set of physically equivalent (and thus redundant) states for every state in the original Hilbert space; therefore, a successful computation will have at minimum at least one numerically-converged state from every set. Practically, this means first making a pass to separate out converged states from those with edge effects, followed by using some method to group together the sets of physically equivalent states.

Checking Convergence

The full K-matrix is infinite in the Floquet m-index direction, even if the original Hilbert space is finite in extent. Diagonalization of the K matrix requires determining where in m to truncate the matrix. For our case, the couplings between the blocks of H fall off very quickly with increasing $|m' - m|$, so it is tempting to suppose not many m's need to be kept. Unfortunately, the first set of off-diagonal blocks have large amplitude. This combines with the quadratic scaling of the harmonic terms within individual blocks to cause truncation effects in the m direction that extend deep into the system. We reveal such states by examining the total probability

for an atom to be at *any* site at any point in a single drive cycle, that is

$$p_{\text{tot}}(t) = \sum_n |\langle n|\psi(t)\rangle|^2 \tag{5.79}$$

$$= \sum_n \left[c^*_{n,m'} e^{-im'\Omega t}\right] \left[c_{n,m} e^{im\Omega t}\right] \tag{5.80}$$

$$= \sum_n \sum_{m,m'} c^*_{n,m'} c_{n,m} e^{i(m-m')\Omega t} \tag{5.81}$$

which trivially must be 1 for states that correspond to reality.

Note that this is different from having a state that is normalized in the extended Floquet basis

$$1 = \sum_{n,m} |c_{n,m}|^2 \tag{5.82}$$

for any particular Floquet state, which only restricts the average total population over a cycle to be 1.

States near the truncation point of m of the system cannot access the artificially truncated m-components that enable unity $p_{\text{tot}}(t)$, necessarily placing some excess population into some other m-states that would not be populated in the infinite matrix case. This causes $p_{\text{tot}}(t)$'s diversions away from 1. This suggests we base a numerical test on p_{tot} that will let us distinguish those states that have converged from those that have not. One possible measure is the root mean square (RMS) deviations averaged over one cycle of the drive

$$\overline{\Delta}_{\text{rms}} = \sqrt{T^{-1} \int_T [1 - p_{\text{tot}}(t)]^2 dt}. \tag{5.83}$$

Considering first the expanded form of the integral, containing an integral with $p^2_{\rm tot}(t)$ and the remainder

$$\begin{aligned}\frac{1}{T}\int_T 1-2p_{\rm tot}(t)dt &= 1-\frac{2}{T}\int_T \sum_n \sum_{m,m'} c^*_{n,m'}c_{n,m}e^{i(m-m')\Omega t}dt \\ &= 1-2\sum_{n,m} c^*_{n,m}c_{n,m} = -1 \end{aligned} \tag{5.84}$$

where we've used the normalization condition Eq. (5.82) in the final line. The other term is

$$\begin{aligned}\frac{1}{T}\int_T p^2_{\rm tot}(t)dt &= \frac{1}{T}\int_T \left(\sum_{n,m,m'} c^*_{n,m'}c_{n,m}e^{i(m-m')\Omega t}\right)\left(\sum_{p,q,q'} c^*_{p,q'}c_{p,q}e^{i(q-q')\Omega t}\right)dt \\ &= \sum_{\substack{n,m,m'\\p,q,q'}} c^*_{n,m'}c_{n,m}c^*_{p,q'}c_{p,q} \text{ for } (m-m') = -(q-q'). \end{aligned} \tag{5.85}$$

Setting $l = m - m'$ and $r = q - q'$ and eliminating the primed indices from the equation yields

$$\frac{1}{T}\int_T p^2_{\rm tot}(t)dt = \sum_{\substack{n,m,p,q\\l,r}} c^*_{n,m-l}c_{n,m}c^*_{p,q-r}c_{p,q} \text{ for } l=-r \tag{5.86}$$

$$= \sum_{\substack{n,m\\l,p,q}} c^*_{n,m-l}c_{n,m}c^*_{p,q+l}c_{p,q}. \tag{5.87}$$

Selecting just the $l = 0$ term to evaluate separately gives

$$\sum_{\substack{n,m\\p,q}} c^*_{n,m}c_{n,m}c^*_{p,q}c_{p,q} = \sum_{n,m}|c_{n,m}|^2\sum_{p,q}|c_{p,q}|^2 = 1, \tag{5.88}$$

which cancels the -1 from Eq. (5.84). The only part remaining is thus the $l \neq 0$ part of the sum. Following the suggestion from the notation $c_{n,m}$, we consider these factors a matrix, allowing us to write the sum as

$$\sum_{m,q,l} (c^\dagger c)_{m-l,m} (c^\dagger c)_{q+l,q} \tag{5.89}$$

by converting the sums over n and p into matrix multiplications. This is the cumulative sum of the sums of products of components from opposite diagonals of the $c^\dagger c$ matrix. We arrive at the result

$$\overline{\Delta}_{\text{rms}} = \sqrt{\sum_{m,q,l} (c^\dagger c)_{m-l,m} (c^\dagger c)_{q+l,q}} \tag{5.90}$$

which is straightforward to evaluate numerically. Though this result is exact, numerical errors intrinsic to 32-bit floating point computations[126] (both those occurring in the input state and those that occur during the evaluation of Eq. (5.90)) place a lower bound on this quantity of $\sim 10^{-8}$. Values above this are accurate, but to further refine them we turn to the brute force numerical integration. For clarity we will refer to the RMS deviations calculated this way as $\widetilde{\Delta}_{\text{rms}}$, reserving $\overline{\Delta}_{\text{rms}}$ for the form from Eq. (5.90). Though much slower, even a simplistic numerical integration method reaches a lower bound of $\sim 10^{-16}$, consistent with the floating point accuracy for numbers ~ 1.

A comparison of the results for a sample simulation are shown in Fig. 5.7, showing excellent agreement for higher values. They diverge where the lower bound

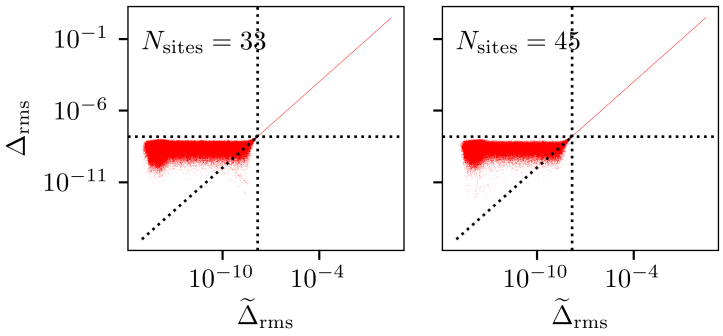

Figure 5.7: A comparison of the two methods of computing the root mean squared deviations from 1 for a simulation with $n = 33$ sites and m's covering the range ± 100. The vertical axis is $\overline{\Delta}_{\text{rms}}$ evaluated from the occupations coefficient $c_{n,m}$. The horizontal axis is $\widetilde{\Delta}_{\text{rms}}$, evaluated through numerical integration. They are plotted together on a log log scale, with a dotted box showing the cutoff threshold of 1.5×10^{-8} used to select states for further refinement.

behavior discussed above sets in. The numerically integrated version clearly extends to much lower values.

Grouping Equivalent States

Every group of physically equivalent states has only one representative per quasienergy Brillouin zone, with every representative having the same quasienergy modulo the drive energy quanta. This suggests a convenient algorithm; find the quasienergy modulo $\hbar\Omega$ for every converged state, sort them (and their corresponding states), and find the quasienergy differences between neighbors in the sorted list. Differences above some manually adjusted threshold indicate a transition to the next group of states.

There may be cases where some degeneracy (exact or quasienergy difference below the threshold) cause two or more states to be grouped together by this method. We detect this by checking for multiple states in the same Brillouin zone, which

is a clear indication of a group containing two different states. To separate out degenerate states into their separate groups, we investigate the states' overlaps at $t = 0$. States have overlaps of 1 with other equivalent representations, and 0 with any other state.

For the results presented in this paper this was all that was necessary fully group the converged states. If any states were missing, the solution was increasing m, not working harder to separate out the groups.

Implementation

We implemented this procedure in Python3 using Scipy[127] and Numpy[128, 129] for the numerics. For careful calculation of Fourier coefficients, mpmath[130] provided arbitrary precision arithmetic. During early experimentation we used GNU Parallel[131] extensively to coordinate and balance many small simulation batches.

We present results from two simulations, one with $N_{\text{sites}} = 33$ and $m = [-100, 100]$, and the other with $N_{\text{sites}} = 45$ and $m = [-160, 160]$. The the 45-site version was chosen because it nearly doubles the energy offset for the edge sites compared to the 33-site version. Each scans along the critical values of the drive that cancels the time averaged trap, that is, for a scan varying γ, the corresponding value of Ω_c was chosen as the drive frequency. For comparison results we sometimes present results for the time-averaged Hamiltonian in each case. These we generated with the same code, by restricting it to $m = 0$, guaranteeing good correspondence to the full simulation.

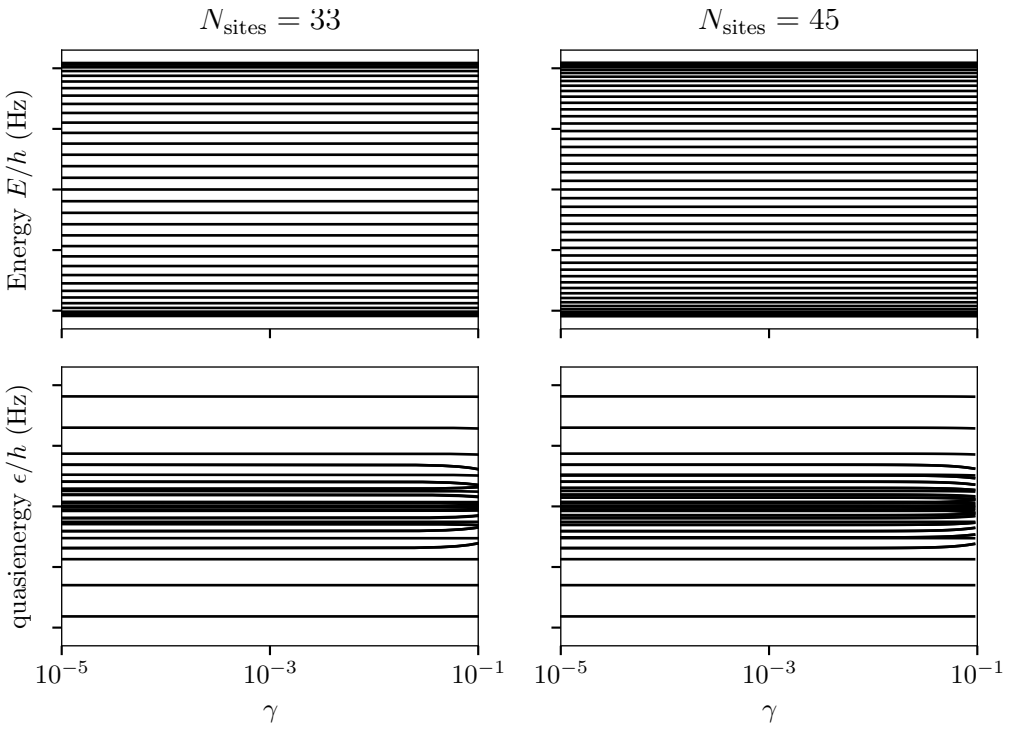

Figure 5.8: Energy levels for the time-averaged Hamiltonian are shown in the top row, with the quasienergies for the full Floquet treatment in the bottom row. At the left the (quasi)energy levels in the first Brillouin zone are plotted as γ varies for the critical drive condition for the smaller length lattice. At the right the same quantities are plotted for the larger lattice. To maintain the critical drive condition the drive frequency is varied as in Eq. (5.64) to cancel the external trap. Each shows constant quasienergy until the drive frequency approaches the lattice depth, just before $\gamma \approx 10^{-1}$.

5.7 Results

The first quantity of interest is the distribution of quasienergies as the parameters vary, which Fig. 5.8 displays. The time-averaged case shows the expected sampling of a cosine band structure, with energies grouped at the upper and lower edges of the band, but the density of states slowly varying. In stark contrast the quasienergy structure appears to collapse toward the center, leaving the upper and lower regions sparsely occupied while densely packing the center. Comparing the 33

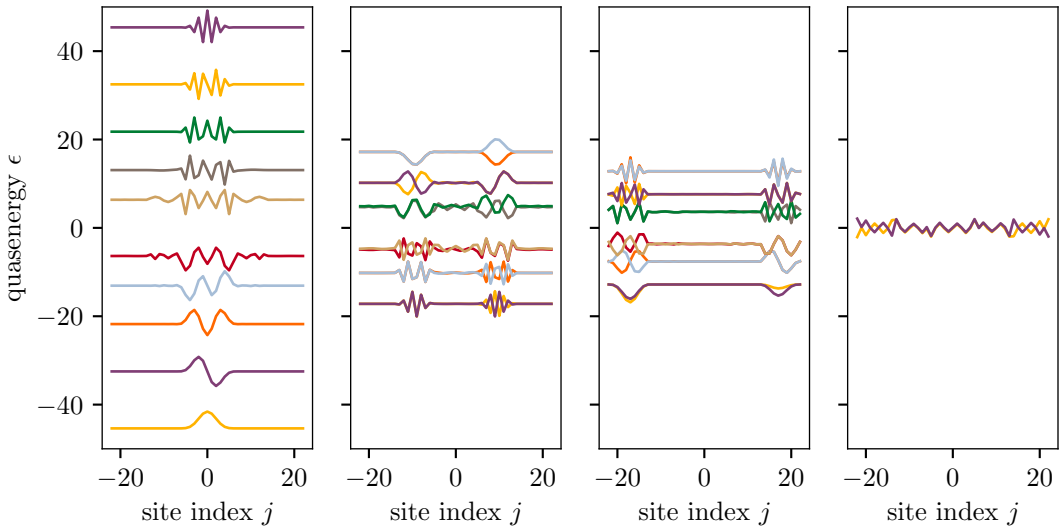

Figure 5.9: The on-site amplitudes for the shorter $N_{\text{sites}} = 33$ lattice eigenstates, offset so the zero level for each state is at the corresponding quasienergy. They are grouped together to emphasize the spatial isolation apparent in each set.

and 45 cases shows the additional states have all appeared near the center, while the outer edges have not shifted. Additionally, the quasienergies remain constant for values of the drive approaching 10^{-1}, at which point some (but not all) begin to shift. Note, low γ is not a weak drive, as the drive frequency is greatly increased for small γ, so this is not a consequence of a weak-drive limit. Rather, for larger γ the corresponding $\hbar\Omega_c$ approaches the lattice depth from above, states in nearby quasienergy Brillouin zone close enough to influence the states.

Next, we investigate the corresponding eigenstates for each lattice. Shown in Fig. 5.9 is each eigenstate, split into intentionally suggestive groups. Note each grouping has pairs of states equidistant from quasienergy zero, that the states in each grouping are localized is space, that those state pairs differ by an alternating sign from site to site, and that the overall ordering inverts for some groups compared to the other. The more delocalized set(s) are all near-zero quasi energy, and seem to

concentrate at the boundaries between the other states. This is true for both lattice sizes, with the larger lattice having more groups.

Figure 5.10 returns to these groups, showing the $|n_j|^2$ and $|\psi(p)|^2$ for each. Again the isolated sets of states appear in position space, but they are much less easily separated in momentum space.

To investigate where the apparent decoupling of regions of the lattice comes from, we use the obtained eigenvectors and quasienergies to reconstruct an effective Hamiltonian for stroboscopic evolution times. Figure 5.11 shows this for each lattice, and the reason for the decoupling is immediately obvious. The nearest neighbor tunneling terms vary along the lattice, including some zero crossings. At the zero crossings, tunneling between regions will be strongly suppressed. The apparent flipping of some groups is also explained due to the sign change of the tunneling term. The Hamiltonian is otherwise a constant, with no trace of the harmonic trap remaining (as expected).

To further investigate this, we plot in Fig. 5.12 the tunneling matrix elements, with the horizontal position labeled as the point equidistant between the lattice sites it connects. They appear to vary as $\mathcal{J}_0$ from the center with appropriate scaling. A fit confirms this, finding the tunneling goes as $-25.9\mathcal{J}_0(0.41j)$. Note that all we have directly modulated here is the global lattice spacing, but we have produced a very local spatial modulation of the tunneling amplitudes. As far as we are aware this is the first demonstration of a spatially-modulated tunneling.

While it is tempting to identify these Bessel function tunnelings with the time-averaged Hamiltonian in the lab frame from the beginning of the chapter, this

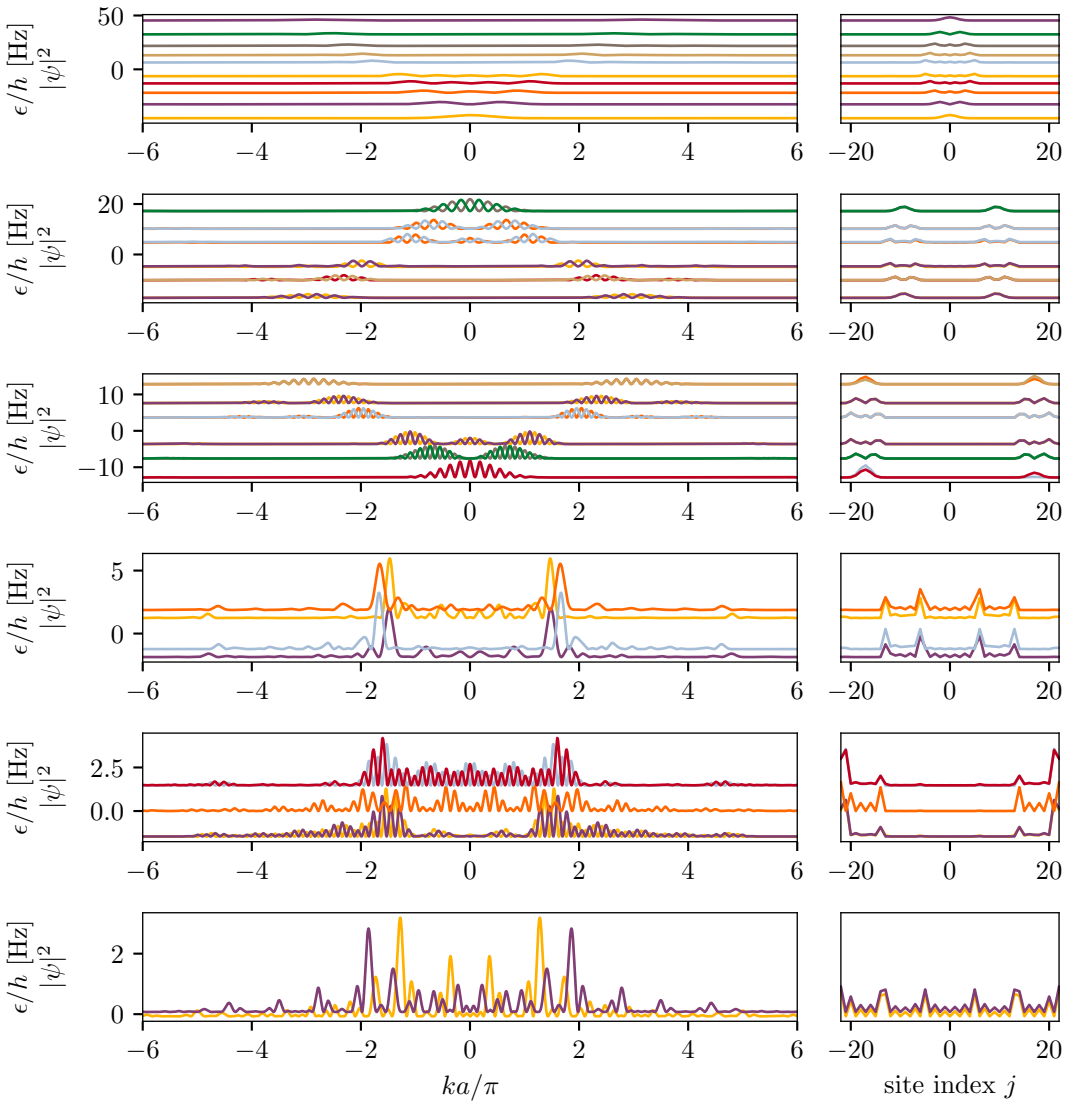

Figure 5.10: (Left) the $|\psi(p)|^2$ of states from the $N_{\text{states}} = 45$ longer lattice, with the baseline offset by the quasienergy of the state. (Right) the $|\psi(j)|^2$ of the same states with the same offsets. The left axis is quasienergy, and the vertical scaling of the wavefunction is arbitrary. The sites are grouped into rows by similar character as in Fig. 5.9, but the longer lattice has more total groups.

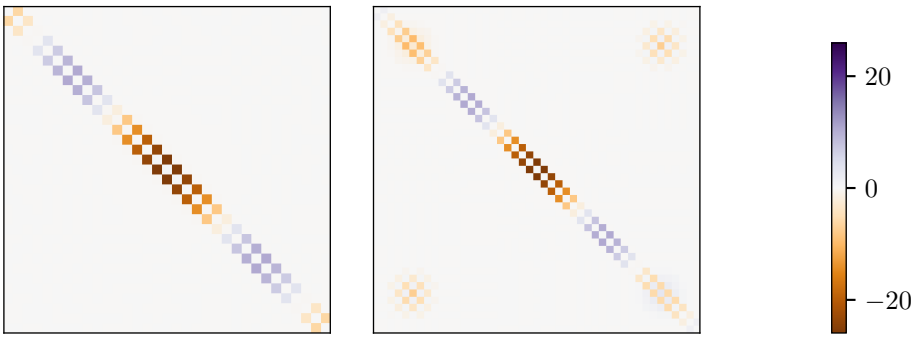

Figure 5.11: The effective Hamiltonian for both the shorter (left) and longer (right) length lattice. All entries are real, so plotted are the actual values for each entry. Both show the same size regions with positive of negative tunneling term, with zeros at the same locations along the lattice.

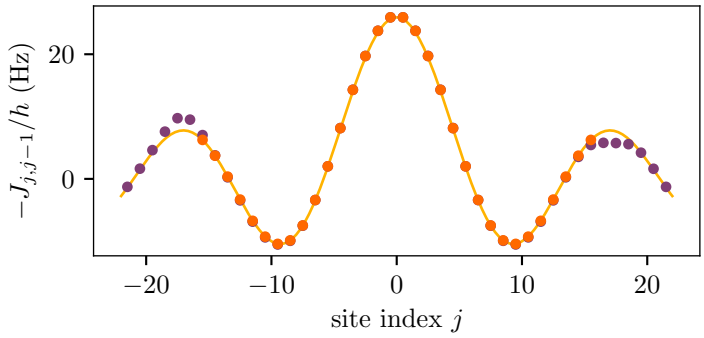

Figure 5.12: Shown is the effective tunneling term for nearest-neighbors across the short (orange dots) lattice and the longer (purple dots) lattice for each coupling pair. A fit to the orange points, shown in the orange line, has the equation $-J_{j,j-1} = 25.9\mathcal{J}_0(0.41j)$.

would not explain the tunneling amplitudes we see here. First, the magnitude of the tunneling peaks at the central site, but the time-averaged potential has its largest barriers between sites there, which would tend to maximally suppress the tunneling. Second, the next order in time scales with $\mathcal{J}_1$-like dependence in space, and so on for higher order terms. Third, in any case, the barrier between adjacent sites always remains finite, so zeros in the tunneling cannot occur from these time-averaged effects. This means the must some other mechanism driving the suppression of tunneling there.

There is a local behavior that differs from site-to-site as we drive the spacing; sites further from the center of the lattice move further in the lab frame. We consider this a "local shaking" and apply the shaken lattice tunneling renormalization result site-by-site. Madison et al. give the scaling of tunneling with drive amplitude[132], suitably translated to our quantities, as

$$J \propto \mathcal{J}_0\left(\frac{M\lambda_s a\Omega^2}{k_{\text{eff}}\hbar\Omega}\right) = \mathcal{J}_0\left(\frac{j\pi\gamma\hbar\Omega\sqrt{1+\gamma^2/2}}{4E_R}\right). \tag{5.91}$$

where the modulation index λ_s is now site-dependent $\lambda_s \approx j\gamma$ in the small-drive limit. Using the critical drive from Eq. (5.64) this yields

$$\mathcal{J}_0\left(\frac{\sqrt{2}\pi\sqrt{(1-\gamma^2)(1+\gamma^2/2)}}{4}\frac{\hbar\omega_T}{E_R}j\right). \tag{5.92}$$

In the small-γ limit (approximating the final radical as 1), this becomes for the presented simulations $\mathcal{J}_0(0.41j)$, in excellent agreement with our fit.

These simulations thus show that, in the single-band tight-binding limits, a lattice that is periodically stretched and compressed experiences a site-dependent modulation of the tunneling amplitudes. These are characterized by a "local-shaking" parameter, which relates the global tunneling renormalization of a shaken-lattice systems to the shaking that atoms in an individual lattice site experience.

5.8 Future Directions

There are a many immediately interesting directions to look from the numeric point side of things. The simulations thus far have all the information to study the micromotion, but we have not yet considered it beyond the total probability filter described above. In addition, we constrained this work to the critical drive condition. For weaker drives, the "local shaking" should still renormalize the tunneling, but it is unclear how this might interact with the residual harmonic trapping potential. For instance, Wannier-Stark tunneling should exist between the ground and first excited band for some pair of sites, but the changing energy offset would restrict this to only a few locations in the lattice. An interesting regime is then where this localized interband coupling happen at, say, a node in the ground band tunneling amplitudes. It would be interesting to study how the system approaches the Bessel-function tunneling amplitudes from the no-drive case, for instance, at fixed moderate drive frequency from $\gamma = 0$ to γ_c. Furthermore, zeros in the tunneling suggest that it may not be catastrophic to have small but non-zero antitrapping in the time-averaged case.

The lack of changing structure in the scans presented in this work are apparently due to working in the small-γ limit, where the tunneling renormalization only very weakly depends on the drive parameters. The strong-drive limit was not studied due to the experimentally prohibitively low drive frequencies required. Nonetheless checking for agreement computationally would still be interesting.

Experimentally, the very similar momentum distributions for the isolated state dynamics presents a challenge to observation of this system. However, we have not yet studied the long-period evolution. There may be some momentum space structure that emerges as the various states dephase from one another. Additionally, Eq. (5.92) suggests we can tune the size of connected regions by adjusting E_R via the spacing. Beyond the usual difficulties in applying single-particle models to interacting systems, work using Feschbach resonances has shown that oscillating interaction strength causes site-occupation dependent tunneling terms[133–135]. Squeezing and relaxing the lattice sites will certainly drive changes in the interaction parameter through the changing density of the Wannier state in the lab frame, possibly incorporating those same effects.

Chapter 6: Summary

This thesis introduced the background theory behind the operation of our lab, and discussed the main features of the experimental apparatus. Following that, two studies were presented.

The first (Chapter 4) demonstrated the existence of a Griffiths phase in an experimental implementation of a disordered stack of 2D atomic pancakes. Measurement of momentum fluctuations agrees with the existance of a sliding phase in this system. Further theory support would help provide quantitative confirmation.

The second (Chapter 5) showed a single-band tight-binding model for a breathing (or accordion) optical lattice system. Theory calculations showed that the breathing lattice system produces a spatially-modulated tunneling rate. Taking a "local-shaking" approximation connects the breathing lattice result to the Bessel function form of this site-dependent hopping term, correctly predicting the spatial scale of the tunneling variations. There are many possibilities for future work in this system, both experimentally and theoretically.

Appendix A: Essential Parts Lists

As a supplement to Chapter 3 a collection of parts lists is presented here. None of the provided lists is intended to be exhaustive, but rather to highlight the key components of each item. Each table contains a source with part number as well as a description of the component. The source is the manufacturer where available, otherwise it a vendor where the component can be obtained. The vendor is provided only as a reference for a possible source, and not necessarily as a recommendation of any particular vendor.

Line	Source	Part Number	Description
A.1.1	Kimball Physics	MCF600-SO200800-A	6.0 inch Spherical Octagon - Vacuum Chamber
A.1.2	Varian	9191580	150 L/s Double-ended StarCell ion pump
A.1.3	Varian	9191340	55 L/s StarCell ion pump
A.1.4	SAES	CapaciTorr D 400-2	Non-evaporable getter vacuum pump
A.1.5	Granville-Phillips	274042	Dual filament nude Bayard-type ion guage
A.1.6	Kurt Lesker	SG0150MCCF	Manual gate valve
A.1.7	Kimball Physics	MCF450-SS20400-A	Spherical square vacuum chamber
A.1.8	StarnaCells	3-Q-20	Glass cell

Table A.1: Essential components for constructing the vacuum system

Line	Source	Part Number	Description
A.2.1	IXYS	IXFN520N075T2	750 V 480 A 1.9 mΩ Power MOSFET
A.2.2	HP	6269B	Adjustable current supply, min 30A, 8V
A.2.3	ThermoTek	T255P	Recirculating chiller, 210 W Dissapation, 1.0 GPM
A.2.4	McMaster	35035K42	Aluminum cold plate
A.2.5	White & Rogers	70-111224	SPNO Continuous Duty contactor

Table A.2: Essential electrical parts for constructing the Zeeman slower and its current controls

Line	Source	Part Number	Description
A.3.1	S&W Wire	0.158SQ	Square copper tubing with Kapton insulation
A.3.2	King Instruments	7520-2-1-1-3C-02	1 GPM flow meter with control valve
A.3.3	Proteus	01004BN1	Flow switch
A.3.4	McMaster	82395K83	220 p.s.i., 2.2 GPM rotary vane pump
A.3.5	McMaster	7913A4 or A3	Welding cable lugs
A.3.6	Agilent	6671A	220 A, 8 V adjustable power supply
A.3.7	STMicroelectronics	STE250NS10	100 V 220 A 5.5 mΩ n-Channel Power MOSFET
*	IXYS	IXFN340N07	*(Alternate for A.3.7)* 70 V 340 A n-Channel MOSFET
A.3.8	LittleFuse	V18ZA40P	18 V, 20 mm varistor
A.3.9	Danfysik	UltraStab 867-2001HF	200A current transducer with 1:1000 ratio
A.3.10	New Focus	LB1005	PI controller
A.3.11	King Instruments	7520-2-1-1-3C-04	2 GPM flow meter with control valve

Table A.3: Essential components for construction the quadrupole field coils and their controlling electronics.

Line	Source	Part Number	Description
A.4.1	IPG Photonics	ELR-15K-LP-SF	Single mode 15 W 1550 nm Erbium-doped fiber laser
A.4.2	Toptica GMBH	DLX 110	Grating stabilized single mode tunable diode laser at 780 nm
A.4.3	Toptica GMBH	DL Pro	Grating stabilized single mode tunable diode laser at 780 nm
A.4.4	Coherent	Verdi V-10	10 W 532 nm pump laser
A.4.5	TekhnoScan	TIS-SF-07	continuous wave (CW) single-frequency ring Ti:Sapphire laser
A.4.6	ThermoTek	T255P	Recirculating chiller, 210 W Dissipation, 1.0 GPM

Table A.4: Lasers used in the apparatus.

Line	Source	Part Number	Description
A.5.1	Delta RF	LA10-1-525-40	10 W Class A Amplifier, 40 dB gain, 525 MHz
A.5.2	Agilent	3320A	Function generator
A.5.3	Mini-Circuits	ZS90-2-50-S+	Passive Frequency Doubler
A.5.4	Mini-Circuits	VHF-5500+	6 GHz high pass filter
A.5.5	Analog Devices	ADF4350EB1Z	Phase Locked Loop evaluation board
A.5.6	Mini-Circuits	ZX60-8008E-S+	Wideband amplifier 20 MHz to 8 GHz
A.5.7	Programmed Test Sources, Inc.	PTS160	0.1 to 160 MHz programmable frequency synthesizer
A.5.8	SpinCore	PB24-100-4k-USB	24 channel digital pulse generator
A.5.9	Narda	903N	Microwave double stub tuner
A.5.10	HP	493A	Travelling Wave Tube microwave amplifier, 4.0 to 8.0 GHz
A.5.11	Microtech	206476	Waveguide to coax adapter, 5.85 to 8.20 GHz

Table A.5: Essential parts for microwave and RF generation.

Line	Source	Part Number	Description
A.6.1	Point Grey Research	FL2-14S3M	1348×1032 monochrome CCD camera with 4.65 µm pixels
A.6.2	Point Grey Research	FL2G-13S2M	1288×964 monochrome CCD camera with 3.75 µm pixels
A.6.3	Semrock	NF03-785E-25	785 nm StopLine single-notch filter
A.6.4	Semrock	FF01-709/167-25	709/167 nm BrightLine single-band bandpass filter

Table A.6: Essential parts for the imaging systems used in the apparatus.

Line	Source Part Number	Description
A.7.1	ConOptics Model 360-40	Electro-optic modulator
A.7.2	IntraAction ATM-802FA49	80 MHz AOM
A.7.3	Aerotech ABL20040-10-LT40AS-NC	1-axis air bearing translation stage
A.7.4	NKT Photonics LMA-PM-15	Single mode 1.5 µm polarization maintaining fiber
A.7.5	NEOS Technologies 23080-2-1.55-LTD	2 mm aperture 1.5 µm AOM

Table A.7: Essential parts for the main and cross dipole traps.

Line	Source Part Number	Description
A.8.1	National Instruments PCI-6713	12-bit 8 Channel 1 MS/s analog output device
A.8.2	National Instruments NI USB-6353	X Series DAQ 1.25 MS/s
A.8.3	SpinCore PBUSB-RM-24-100-4k	24 Channel Rack-mount 10 ns resolution

Table A.8: Essential parts for computer control in the apparatus.

Appendix B: Publication: Griffiths Physics in an Ultracold Bose Gas

Note: The following is the text of work published by our group in PRA[111] adjusted in format only *to comply with style requirements.*

B.1 Abstract

Coupled XY model systems consisting of three-dimensional (3D) systems with disordered interlayer physics are of significant theoretical interest. We realize a set of coupled quasi-2D layers of ^{87}Rb in the presence of disordered interlayer coupling. This is achieved with our high bandwidth arbitrary optical lattice to obviate restrictions on the dimensionality of disorder with speckle-generated optical fields. We identify phase crossover regions compatible with the existence of a pair of intermediate Griffiths phases between a thermal state and the emergence of bulk 3D superfluidity.

B.2 Introduction

The intersection of dimensionality and disorder is a rich area of study in condensed-matter physics. The precise control of disorder available with optical potentials enables the realization of well characterized disordered systems with quantum degenerate atomic gases. Optical speckle has been used to generate

disorder for one-, two-, and three-dimensional systems [64, 136, 137], exhibiting Anderson localization, a disordered Berezinskii-Kosterlitz-Thouless (BKT) transition [14], mobility edges in three dimensions [138], and emergence of a Bose glass [139]. Similarly, quasidisorder provided by incommensurate lattices has been used to realize the Aubry-André model in the presence of interactions [140], the role of quasi-disorder in adiabaticity [141], to study many-body localization [142], and has been contrasted against uncorrelated disorder in transport [143].

While two-dimensional (2D) Bose gases in isolation are well described by BKT physics [8] (approximated by the XY model), recent theoretical work [103–105] suggests rich behavior when layers of such systems (including stacks of 2D superfluids, cuprate superconductors, and planar magnets) are randomly coupled to one another. They are predicted to exhibit Griffiths physics [107, 108, 144] when the interlayer couplings or layer thicknesses are subject to uncorrelated disorder. A pair of phases of matter emerge as the temperature is lowered from a nondegenerate state to bulk 3D order (Bose-Einstein condensate, magnetization, or superconduction). Each intermediate phase is a Griffiths phase, with properties dominated by the most extreme local deviation in the disordered system. The first is an anomalous Griffiths phase, a class of sliding phase [106] that exhibits 2D order (superfluidity, magnetic susceptibility, or superconduction). The second is a semiordered Griffiths phase where order appears in the third dimension. (Magnetic Griffiths phases have recently been observed in bulk metal alloy systems [145, 146], but not in anisotropic systems.)

References [103–105] employ the phase stiffness ρ_s^x along a direction e_x to characterize the Griffiths phases. Phase stiffness is a measure of the energy required

to impose a phase difference ϕ_x between two ends of a finite system. As a function of system size L and system energy E, the phase stiffness is defined as

$$\rho_s^x = \frac{1}{L}\frac{d^2E(\phi_x)}{d\phi_x^2}. \tag{B.1}$$

While a computationally convenient parameter, it is not easily measurable in experimental atomic systems. Although it is possible to measure the critical velocities of superfluids [147], these disordered systems are predicted to have very small superfluid fractions and critical velocities over much of the phase diagram. Instead we use an analysis of the fluctuations in large data sets of time-of-flight (TOF) momentum distributions to gain information about the phases as a function of temperature and lattice depth.

We associate the appearance of a Thomas-Fermi-like distribution in the two in-plane dimensions ($p_\parallel$) paired with a thermal distribution in the third ($p_\perp$) with a 2D superfluid transition at $\sim$200 nK. As we decrease the temperature we observe the emergence of discrete modes in fluctuation correlations along $p_\perp$ [148], which may characterize the expanding length-scales of superfluid puddles in the anomalous Griffiths phase. Finally we interpret the suppression of zero momentum atomic density fluctuations at our lowest temperatures with the Bose statistics of macroscopically occupied non-local state, an observation consistent with 3D superfluidity.

B.3 Experimental Approach

We study this system using optical potentials generated for a cloud of ultracold ^{87}Rb. After initial loading and cooling, the atoms are held in vacuum by a pair of optical tweezers. There they are subjected to a disordered 1D optical potential from an optical lattice generation system. They are further cooled via optical evaporation to temperatures from 10 to 250 nK. This temperature range spans both thermal and degenerate states of the atomic cloud. After some evolution time in the lattice, we release the atoms from all optical fields to expand ballistically. They form a position distribution determined by their momentum distribution at the time of release. This is repeated many times, allowing us to study statistics of the measured momentum distributions. Each part of this process is discussed in more detail below.

We create degenerate gases of ^{87}Rb using a hybrid magnetic trap-optical dipole trap [149], which then loads into a dipole trap whose waist is translated 30 cm into a science chamber. The atoms are finally loaded into a crossed 1550 nm dipole trap and disordered optical lattice, and evaporatively cooled in the $F = 1$, $m_F = -1$ state. Final trapping frequencies ($\nu_\parallel$, $\nu_\perp$) are $E/2\pi\hbar = (100.0, 20.0)$ Hz at our lowest temperatures and (126.5, 25.3) Hz at our highest.

Evaporation begins with a nondegenerate cloud in the presence of our high bandwidth arbitrary lattice (HiBAL) (see Fig. B.1). (Disorder generated using optical speckle necessarily includes variations along the propagation direction [1], so

[1]For 1D speckle disorder to be feasible, the Rayleigh range must be much larger than the cloud size. Our clouds are on the order of ≈10–100 µm, whereas for a speckle with features and wavelength ≈1 µm, the Rayleigh range ($z_R = \pi w^2/\lambda$) is 4 µm.

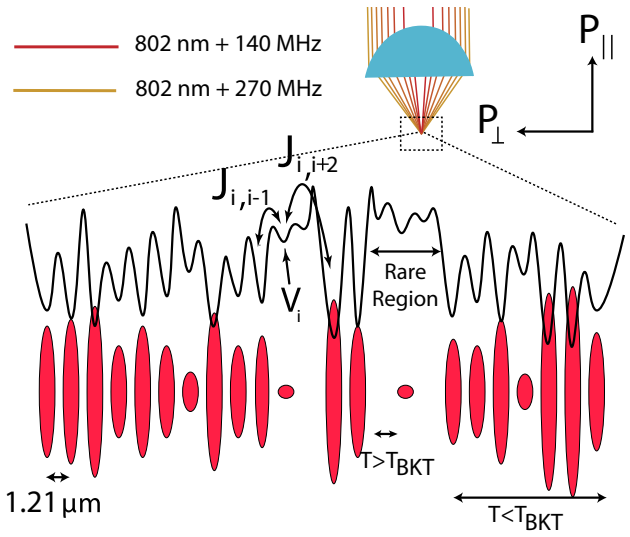

Figure B.1: We engineer a stack of superfluid pancakes with a set of phase-stabilized shallow-angle lattices formed by our HiBAL. Its set of phase-stabilized parallel beams is focused through an aspheric lens to create the 1D disordered optical potential. The local minima have different depths, which generates a local phase space density for each pancake. Interplane hopping $J_{i,j}$ is subject to disorder as well, matching our system most closely with Ref. [103].

the HiBAL was developed to provide the desired potentials.) We Fourier synthesize a potential $U = \sum_j A_j \sin(k_j x + \phi_j)$ from multiple optical lattices spanning two octaves of spatial frequencies. We produce a time-averaged disordered 1D optical potential using 802 nm light with a set of seven shallow angle lattices of incommensurate period ranging from 1.21 to 4.70 µm. The 1.21 µm (base) lattice is phase stabilized to an rms of (6 ± 1) mrad with a Mach-Zehnder interferometer and a piezoelectric transducer-mounted mirror. We confirm the costability of the other optical lattices to our base lattice and our atoms through our diffraction limited 0.5-NA, 22.8× microscope to (19 ± 3) mrad rms. Each lattice pulse is 300 ns in duration. The longest delay between base lattice pulses is 600 ns, and the pulse sequence repetition rate is 3 µs. We use two disordered lattice depths, labeled by the base lattice depth (2.8 and 5.6 kHz). The summed average depth of all seven lattices is 3 times deeper,

with an rms deviation equal to the base lattice depth. Our deeper base lattice depth corresponds to 14 effective recoil energies ($E_R/2\pi\hbar = 0.4\,\mathrm{kHz}$). The rapid pulse rates of our lattices compared to their energy gaps puts us well within the time-averaged potential limit. We observe no differences in heating or TOF images between constant and stroboscopic lattices, thus do not need to consider Floquet physics effects. Shot-to-shot variation in the position of our harmonic 1550 nm trap is sub-µm, and the fastest systematic drift during evaporation is 6 µm/s, which corresponds to energies too small to drive excitations.

The quasi-2D regime in cold gases is reached when the fractional occupation of out-of-plane excited states in an effective, local harmonic oscillator is small. This occurs when the thermal energy scale k_BT is smaller than the harmonic oscillator level spacing $\hbar\omega$, or alternatively when the thermal deBroglie wavelength λ_{dB} is larger than the spatial extent $\sqrt{2\pi}a_z$ where a_z is the harmonic oscillator length [8]. As described above, our disordered lattice has sites with varying depths. For our mean site depth of the shallow lattice ($3 \times 2.8\,\mathrm{kHz} = 8.4\,\mathrm{kHz}$) together with the base lattice spacing, we have $k_BT/(\hbar\omega_\perp) \leq 1$ for $T \leq 250\,\mathrm{nK}$, putting us in the quasi-2D regime throughout.

In this regime, our time-averaged Hamiltonian under the local density approximation is

$$\hat{H} = \sum_i \left[\frac{\hat{p}_\parallel^2}{2m} + V_i - \left(\sum_j \frac{1}{2} J_{i,j} \psi_i^\dagger \psi_j \right) + \tilde{g}_i \psi_i \psi_i^\dagger + \frac{1}{2} m\omega_i^2 \left(x^2 + y^2 \right) \right], \qquad \text{(B.2)}$$

where $\hat{p}_\parallel^2/2m$ is the in-plane kinetic energy, V_i is the lattice well depth, $J_{i,j}$ is the

hopping strength between two lattice sites i and j, $\tilde{g}_i$ is the scaled quasi-2D self-energy term for each pancake, ω_i is the in-plane trapping frequency, which includes small variations due to the disorder [2].

We prepare gases ranging in temperature from 250 nK down to 25 nK in our lattice potentials. The relative phases of our component lattices are arbitrarily tunable. We chose two sets of relative phases to create two different optical potentials with similar statistics. We observe no difference in the results between the two potentials, confirming that our atom cloud is large enough (greater than 70 pancakes) to average over the disorder. Each data set contains two different hold times, 200 ms and 4 s, which show no statistical difference, indicating equilibrium.

We levitate our atoms during 47 ms of TOF with the use of a gravity-canceling magnetic coil with a microsecond switching time to resolve the momentum distributions $n(p_\parallel, p_\perp)$. Gross-Pitaevskii simulations show that our distributions along the disordered direction, $p_\perp$, are minimally distorted by interactions during the expansion due to the rapid expansion of each atomic plane. We conclude that our TOF distributions faithfully represent the momentum distribution along the disordered direction.

B.4 Analysis

The trapping energies along the disorder and in plane differ by over a factor of 85, causing each direction to expand at very different rates. The expansion from the tightest direction of confinement will quickly reduce the local density,

[2] The out-of-plane momentum $p_\perp$ is contained in the $J_{i,j}$ and $\tilde{g}_i$ terms of the Hamiltonian.

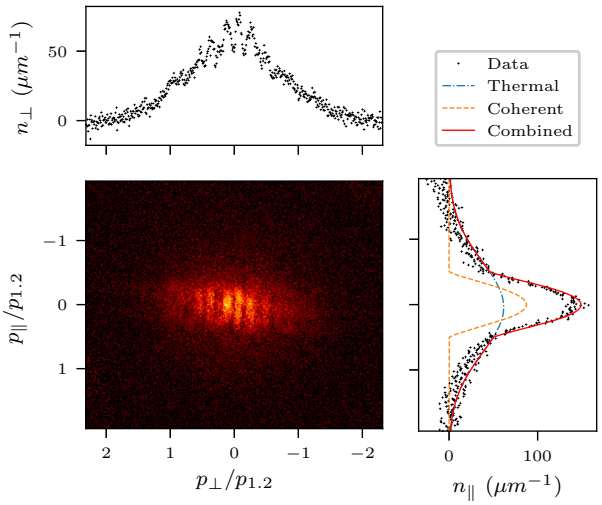

Figure B.2: An example image from a 112 nK cloud in our 2.8 kHz lattice, shown together with the distributions $n_\perp$ and $n_\parallel$ for that image. Momenta are given in units of the recoil momentum of our shortest period lattice, $p_{1.2}$. The bimodal fit to $n_\parallel$ is displayed as a solid red line, with the thermal and coherent parts of the fit displayed separately as a blue dot dashed and orange dotted lines, respectively.

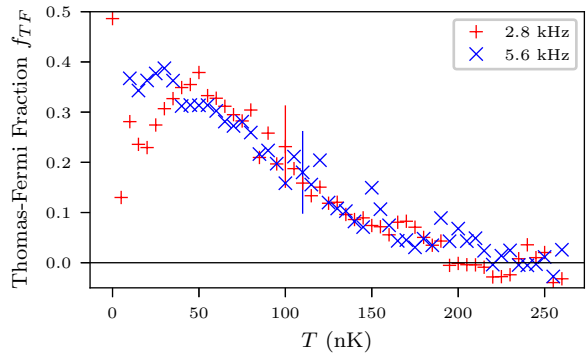

Figure B.3: The fraction of atoms in the Thomas-Fermi distribution, f_{TF}, is plotted as a function of temperature. The shallow lattice is plotted with red +'s, and the deep lattice with blue ×'s. Error bars are the standard deviations of the fractions in each bin, and a typical bar is shown near the center for each lattice depth. We remove a baseline value of 0.054, a fit artifact, from the Thomas-Fermi fraction. f_{TF} is consistent with zero at high temperatures, but increases to finite values as early as 200 nK, establishing $\rho_s^{\parallel} > 0$ below 200 nK.

preventing any interactions that might have otherwise coupled $p_\parallel$ and $p_\perp$ during the ballistic expansion phase. Therefore we treat their momentum distributions as separable. We focus on the in-plane and longitudinal momentum distributions, $n_\parallel(p) = \sum_{p_\perp} n(p_\parallel, p_\perp)$ and $n_\perp(p) = \sum_{p_\parallel} n(p_\parallel, p_\perp)$. At high temperatures $n(p_\parallel)$ is a Gaussian. As the temperature drops a bimodal distribution emerges, a thermal distribution plus a Thomas-Fermi-like distribution as expected after expansion [150]. An example image is shown in Fig. B.2. We apply a bimodal fit to $n(p_\parallel)$ for every cloud, from which we can extract the total number in the distribution N and the number in the Thomas-Fermi part N_{TF}. The Thomas-Fermi fraction (Fig. B.3) is then computed as $f_{\mathrm{TF}} = N_{\mathrm{TF}}/N - 0.054$, corrected for an experimentally determined fit offset. At low temperatures, the thermal distribution becomes comparable in size to the Thomas-Fermi part, causing the fit to underestimate f_{TF}. Both lattice depths show the emergence of a Thomas-Fermi fraction in $n(p_\parallel)$ near 200 nK. This corresponds to a coherent part and finite in-plane phase stiffness. We identify this as the onset of the BKT transition in isolated pancakes. We expect little difference in the BKT transition temperature between the two lattice depths; the band gap and the compression of the planes scale weakly with lattice depth in our relatively shallow lattices.

At lower temperatures coherence between planes emerges in the form of interference effects in $n_\perp(p)$. Identically prepared clouds look radically different from one another in TOF (see Fig. B.4 for example images). The average of images at the same conditions is featureless, as shown in Fig. B.5, so useful information is contained in the fluctuations. Inspired by Fang *et al.*'s success in

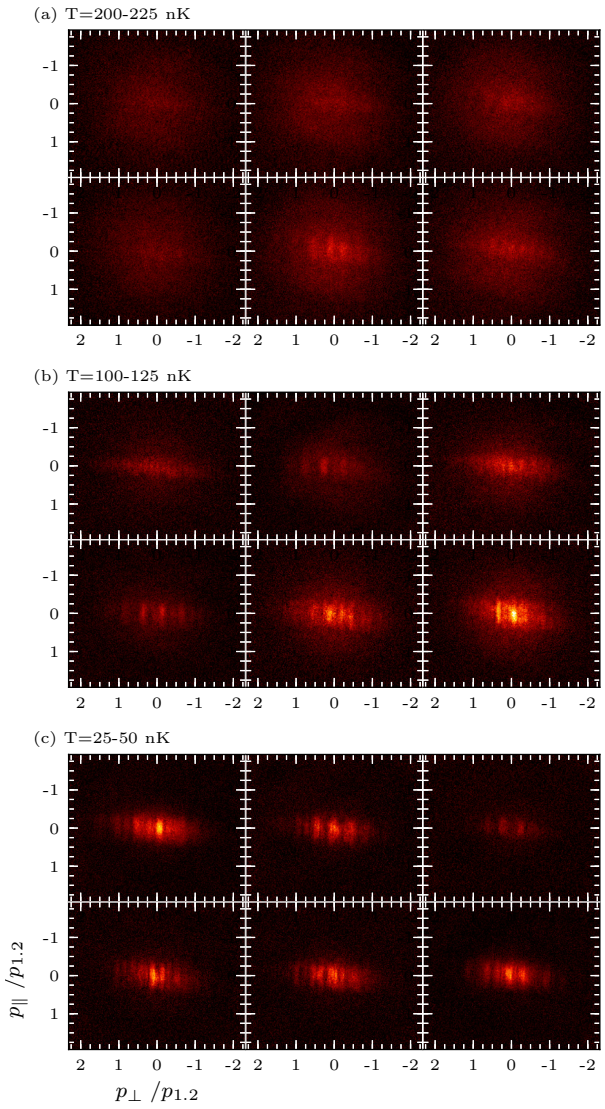

Figure B.4: A random sampling of images at a few temperature ranges in our 2.8 kHz lattice. Top: 200–225 nK; middle: 100–125 nK; bottom: 25–50 nK.

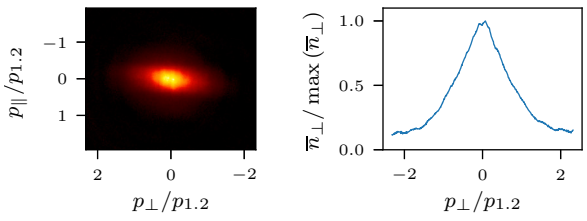

Figure B.5: The (left) average density profile for shots in the 2.8 kHz potential with temperatures between 25 and 50 nK, and (right) $\overline{n}_\perp$ for the same conditions. Neither shows any structure, despite the wide variation seen in Fig. B.4.

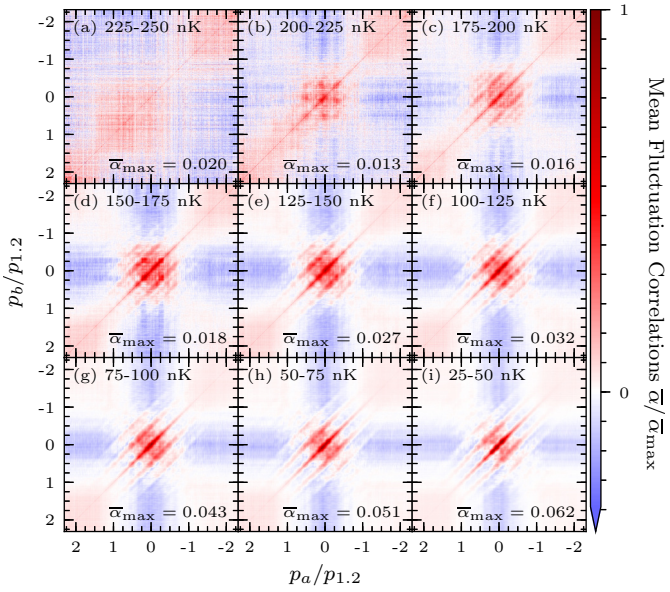

Figure B.6: We display the mean fluctuation correlations of the momentum, $\overline{\alpha}(p_a, p_b, T)$, at decreasing temperatures in panels (a)–(i), with the color scale in each panel normalized to the maximum $\overline{\alpha}_{\max}$. The features at the edge of the panels are artifacts of our normalization scheme. The temperature bins are 25 nK wide, and range monotonically from 225–250 nK in panel (a) to 25–50 nK in panel (i). Note the emergence of distinct momentum peaks in opposite momenta, which do not correspond to the sublattice recoil momenta. The longest length scale resolved is 10.9 µm.

identifying phases of matter in 1D Bose gases [151], which exhibit strong phase fluctuations, we apply a similar analysis to our data. We normalize our distributions to $\sum_p n_\perp(p) = 1$, sort them into 25 nK bins and calculate the average distributions $\overline{n}_\perp(p,T)$. We then calculate the deviation of each cloud from the average for its bin, $\delta n_{\perp,i}(p,T) = n_{\perp,i}(p,T) - \overline{n}_\perp(p,T)$, and calculate the two-body fluctuation correlation function $\alpha_i(p_a,p_b,T) = \delta n_{\perp,i}(p_a,T)\delta n_{\perp,i}(p_b,T)$. The averages of those quantities, $\overline{\alpha}(p_a,p_b,T)$, are displayed in Fig. B.6. Along a line from lower left to upper right is the fluctuation power spectrum $\overline{\alpha}(p,p,T)$. From upper left to lower right is the opposite-momentum power spectrum $\overline{\alpha}(p,-p,T)$. Fig. B.7 normalizes the latter by the former, and is a measure of fractional correlations of opposite momenta, $\beta = 2\overline{\alpha}(p,-p,T)/[\overline{\alpha}(p,p,T) + \overline{\alpha}(-p,-p,T)]$. Together these show qualitative changes as a function of temperature and lattice depth. In concert with our measurement of in-plane coherent fraction, we identify those differences with a set of phases of matter.

Our atomic gases are finite in size and harmonically trapped in all three dimensions. While disorder plays a strong role in the onset of superfluidity in each pancake, our harmonic trap favors emergence of order from its center. Consequently there are likely multiple phases of matter in most of our temperature bins. The 2.8 kHz lattice exhibits several competing varieties of correlation in $\overline{\alpha}$ as a function of temperature. Isotropic thermal correlations dominate along the lattice between 250 and 175 nK as seen in Fig. B.6(a)–(c), when the coherent fraction in plane is insufficient to give rise to interference effects. The lack of any structure in the normalized correlations β is apparent in Fig. B.7(a). The apparent nonzero

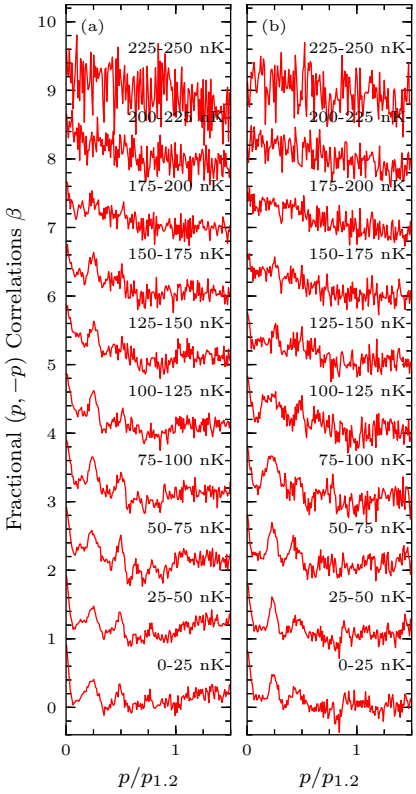

Figure B.7: Normalized $p,-p$ correlations $\beta = 2\overline{\alpha}(p,-p,T)/[\overline{\alpha}(p,p,T) + \overline{\alpha}(-p,-p,T)]$ for (a) the 2.8 kHz and (b) the deeper 5.6 kHz lattice. Thermal correlations persist to lower temperatures in (b) than (a), despite similar coherent fraction as seen in Fig. B.3.

correlations in the thermal state derive from the finite width of the temperature bins. Colder clouds have smaller rms widths, and vice versa, so fluctuation amplitudes are symmetric about $p_\perp = 0$ and nonzero. The thermal nature of the correlations imply that $\rho_s^\perp = 0$. Below 200 nK, we begin to see the growth of a coherent fraction in Fig. B.3, implying that $\rho_s^\parallel > 0$. Concurrent $\rho_s^\perp = 0$ and $\rho_s^\parallel > 0$ constitute evidence of a sliding phase, a phase exhibiting 2D superfluidity in a 3D bulk, consistent with an anomalous Griffiths phase [103–105].

Correlations in our 2.8 kHz lattice begin to exhibit structure below 175 nK as seen in Fig. B.6(d). We use a multi peak Gaussian fit as a generic localized distribution to analyze our β distributions. Strong positive correlations in $(p_\perp,-p_\perp)$ emerge around $p_\perp = 0$, and momenta corresponding near wavelengths of 2.4, 3.0, 4.9 and 10.8 µm. The 4.9 and 10.8 µm modes blend together into one broad peak at temperatures below 50 nK, as do those at 2.4 and 3.0 µm, and at our lowest temperatures 3.0 µm correlations are suppressed. These emergent length scales are distinct from the periods composing our disordered potential (1.21, 1.37, 1.58, 2.02, 2.50, 2.79 and 4.70 µm). Both the momenta peaks in the correlation spectra and the lattice recoil momenta were measured with the same optical system, thus there is no scale-factor uncertainty between the two. There is a peak in β nearby the 2.50 µm lattice. However, there is nothing special in our potential about this component, for it is neither the shortest nor the longest period in the potential, and its amplitude and phase are chosen in the same manner as every other component. The correlations on the 4.9 and 10.8 µm length scales are larger than any imposed by our disorder. We do not see any peaks in $\overline{\alpha}$ corresponding to the recoil momenta of the four lattices

with the smallest periods.

While correlation peaks may emerge in completely incoherent lattice systems due to uncorrelated phase noise [152, 153], this does not explain our results. We confirmed this with a simple 1D single-particle simulation of noninteracting thermal distributions in our disordered lattice, which did not match our results. The simulations show correlations at low temperature, which depend on choice of relative phases, exist for each sub-lattice below 50 nK, and emerge first in high momentum states. In contrast, experimentally observed correlation peaks are evident at higher temperatures (~ 175 nK), only occur at a few momenta, and emerge first at low momentum.

The length scales of fluctuations depend on two factors. First, the lattice imposes structure on the coherent fraction; second, the temperature determines the size of coherently connected lattice sites ("puddles") and the distances between them. As the temperature is lowered, the system transitions to a fully connected puddle and lowering the temperature further has no effect. We attribute this transition to the population of many-body phonon modes as more pancakes undergo the BKT transition, leading to larger superfluid puddles and increasing overall coherent fraction. This is the process described by [103], as the anomalous Griffiths phase proceeds towards the superfluid transition with decreasing temperature.

This structure first emerges as peaks in Fig. B.6(d), and then settles to its final forms in Fig. B.7(a) below 100 nK. As mentioned, we interpret the settled form of β below 100 nK as the establishment of complete connectivity. This suggests that below 100 nK the system has crossed over to a Griffiths superfluid phase from an

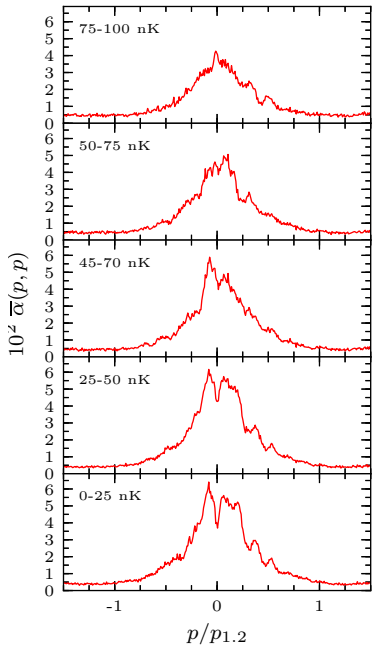

Figure B.8: Displayed are the square fluctuations $\overline{\alpha}(p,p)$ for a few choices of temperature in our 2.8 kHz lattice. A drop in fluctuations at $p = 0$ emerges below 70($\pm$2.5)nK.

anomalous Griffiths phase. While we cannot measure phase stiffness directly, we expect it to be quite small in this regime [103, 104].

The same trend can be seen in the 5.6 kHz lattice data in Fig. B.7(b), but at much lower temperatures, despite the coherent fraction's concurrent growth with the 2.8 kHz lattice. The disordered lattice in this data set is twice as deep, so we would expect the most depleted pancake's phase-space density, and thus transition temperature, to drop by $1/e$, and we see no evidence it ever leaves the sliding phase.

At temperatures below 70 nK, in our 2.8 kHz lattice, we observe a drop in the fluctuation power spectrum $\overline{\alpha}(p,p)$ at $p = 0$, as shown in Fig. B.8. Its contrast increases with decreasing temperature. We take this as evidence of the suppression of fluctuations due to Bose statistics of a macroscopically occupied, nonlocal state. This is consistent with the onset of finite phase stiffness along the disorder. We

find it difficult to draw a clear line between a superfluid Griffiths phase and a full 3D superfluid. The literature does not discriminate between the two phases using parameters accessible with our system [103, 105], and Ref. [104] does not identify a distinction. If there are two such distinct phases, this macroscopically ordered region is likely the latter.

B.5 Conclusion

Using our HiBAL we engineered an optical field isotropic in two dimensions and disordered in the third dimension. We explored the phase diagram of a previously unrealized class of disordered system. The momentum distributions of individual realizations vary wildly, thus we examined noise correlations as our experimental measure. Although we cannot directly measure phase stiffness (the primary parameter calculated theoretically), we observe trends with temperature consistent with the predictions of this Griffiths system. At high temperatures, distributions show no coherent (low momentum) features in plane and no correlations out of plane. As the temperature lowers, a low momentum (Thomas-Fermi-like) feature appears in plane, suggesting superfluidity in plane, while the out-of-plane correlations are still absent. At even lower temperatures, coherence between planes becomes apparent as a $p_\perp = 0$ peak in the out-of-plane correlations appears along with correlation features at nonzero momenta. Notably we observe discrete momentum peaks in the correlations unrelated to the momentum components of the disordered lattice. This suggests local correlations as some regions within the disordered potential become

phase coherent, which is characteristic of the anomalous Griffiths phase. Finally, below 100 nK the noise correlations change little, suggesting full three-dimensional superfluidity (or at least coherence), although the correlation function is still quite different than a superfluid in a lattice without disorder. At a deeper lattice potential, similar phenomena are observed although the onsets are at lower temperatures, as might be expected as the disorder is better able to prevent coherence buildup. Direct comparison with theory is needed to fully understand this disordered system, and given experimental limitations, would require calculations beyond phase stiffness.

Our HiBAL is a flexible platform capable of generating arbitrary sets of optical lattices over two spatial octaves with phase, amplitude, and wave-vector control at MHz frequencies. It will enable a large set of experiments, from transport measurements in disordered systems and the production of Hamiltonians for the study of Floquet physics, simultaneous with Bragg spectroscopy of all of the above.

Acknowledgements

We would like to thank I. Spielman for the extensive discussions during the preparation of this manuscript.

Appendix C: Breathing Lattice Fourier Components

The driving terms we see in Chapter 5 are rational polynomials in $\cos(\Omega t)$. This suggests a closed form power series representation is possible, and the commonly applied power-reduction formulas for cos imply this can be re-expressed directly as a Fourier cosine series. In our case this is indeed possible, as we show below.

A note on (un)originality of these results

The results presented in this appendix were arrived at independently; however, they are straightforward enough that it is not the first derivation. Unfortunately, a search of both mathematics and physics literature yielded only recent work on, for example, power series of cosines of fractional argument with constant coefficients. As such, in the hope that it may prove useful to others the result is still presented here.

C.1 Power Series in Cosines

Before we begin, a quick note on notation here. Since we will be deriving two differing series for the same function, it will be necessary to represent coefficients in each representation. Throughout this appendix we will use a tilde (e.g. $\tilde{f}_n$) to represent coefficients in the power series representation, a breve accent (e.g. $\breve{f}_n$) for

the Fourier cosine series coefficients, and the complex Fourier series coefficients are unadorned (f_n).

Suppose there is a function $f(x)$ that can be expressed as the sum

$$f(x) = \sum_{n=0}^{\infty} \tilde{f}_n \cos^n \theta. \tag{C.1}$$

We would like to find the equivalent expression as a Fourier cosine series, and eventually a complex Fourier series

$$f(x) = \frac{1}{2}\breve{f}_0 + \sum_{j=1}^{\infty} \breve{f}_j \cos j\theta \tag{C.2}$$

$$= \sum_{j=-\infty}^{\infty} f_j e^{ij\theta} \tag{C.3}$$

where the coefficients $\breve{f}_j$ and f_j can be expressed in terms of the (known) set of $\tilde{f}_n$. We start with the power reduction formula for general n

$$\cos^n \theta = \begin{cases} 2^{-2m}\binom{2m}{m} + 2^{-2m+1}\sum_{k=0}^{m-1}\binom{2m}{k}\cos\left[2(m-k)\theta\right] & n = 2m \\ 2^{-2m}\sum_{k=0}^{m}\binom{2m+1}{k}\cos\left[(2m+1-2k)\theta\right] & n = 2m+1 \end{cases}, \tag{C.4}$$

noting that odd (even) powers of cos produce only odd (even) multiple angles, and that $\cos^m \theta$ is the smallest power of cos that produces $\cos m\theta$. Next, we substitute Eq. (C.4) into Eq. (C.1) and gather terms like $\cos(\ell\theta)$. The $\ell = 0$ term corresponds

to the $\breve{f}_0/2$ term, and is given by

$$\frac{1}{2}\breve{f}_0 = \sum_{m=0}^{\infty} \frac{\tilde{f}_{2m}}{4^m}\binom{2m}{m}. \tag{C.5}$$

For the remaining terms, we take $\ell = 2p+1$ or $\ell = 2p$ as appropriate, and find after further manipulation that for both even and odd ℓ

$$\breve{f}_\ell = \sum_{\substack{n=\ell \\ (n+\ell)\text{ even}}}^{\infty} \tilde{f}_n 2^{1-n}\binom{n}{\frac{n-\ell}{2}} \tag{C.6}$$

$$= 2\sum_{j=0}^{\infty} \frac{\tilde{f}_{2j+\ell}}{2^{2j+\ell}}\binom{2j+\ell}{j} \tag{C.7}$$

where we've made the substitution $j = (n-\ell)/2$. Comparison with Eq. (C.5) reveals that this holds for the $\ell = 0$ case as well.

C.2 Power Series for Lattice Drive

Now we turn to writing the two terms of the drive, ξ and Ξ, as a power series in cos. To do so, we'll be making the substitution $x = \cos\Omega t$, and introducing a related function with an overall factor removed for each,

$$\underline{f} = \frac{f}{1+\gamma^2/2}. \tag{C.8}$$

Recall from Eqs. (5.61) and (5.62) the definitions for ξ and Ξ to write down their counterparts

$$\underline{\xi} = \frac{1}{(1+\gamma x)^2} = \sum_{n=0}^{\infty} \underline{\tilde{\xi}}_n x^n \tag{C.9}$$

$$\underline{\Xi} = \frac{-2\gamma^2 - \gamma x + \gamma^2 x^2}{(1+\gamma x)^4} = \sum_{n=0}^{\infty} \underline{\tilde{\Xi}}_n x^n. \tag{C.10}$$

We'll focus first on $\underline{\xi}$, first finding a recurrence relation for the power series coefficients along with the first two terms

$$\underline{\tilde{\xi}}_0 = 1, \quad \underline{\tilde{\xi}}_1 = -2\gamma, \quad \underline{\tilde{\xi}}_{n\geq 2} = -\gamma(2\underline{\tilde{\xi}}_{n-1} + \gamma\underline{\tilde{\xi}}_{n-2}). \tag{C.11}$$

Standard mathematical technique allow us to use this to compute a closed-form expression for $\underline{\tilde{\xi}}_n$.

$$\underline{\tilde{\xi}}_n = (n+1)(-\gamma)^n \tag{C.12}$$

Similarly for $\underline{\Xi}$, a recursion relationship for the coefficients is

$$\underline{\tilde{\Xi}}_{n\geq 4} = -\left(4\gamma\underline{\tilde{\Xi}}_{n-1} + 6\gamma^2\underline{\tilde{\Xi}}_{n-2} + 4\gamma^3\underline{\tilde{\Xi}}_{n-3} + \gamma^4\underline{\tilde{\Xi}}_{n-4}\right) \tag{C.13}$$

with initial terms

$$\underline{\tilde{\Xi}}_0 = -2\gamma^2,\ \underline{\tilde{\Xi}}_1 = 8\gamma^3 - \gamma,\ \underline{\tilde{\Xi}}_2 = -20\gamma^4 + 5\gamma^2,\ \underline{\tilde{\Xi}}_3 = 40\gamma^5 + -14\gamma^3. \tag{C.14}$$

From this the closed form for each term can be found.

$$\tilde{\Xi}_n = -\frac{n+1}{6}(-\gamma)^n \left[12\gamma^2 - \left(1-10\gamma^2\right) n - 2\left(1-\gamma^2\right) n^2\right] \tag{C.15}$$

C.3 Fourier Components

We begin finding the Fourier coefficients by substituting Eq. (C.12) into Eq. (C.7)

$$\breve{\xi}_\ell = 2\sum_{j=0}^{\infty} \frac{(2j+\ell+1)(-\gamma)^{2j+\ell}}{2^{2j+\ell}} \binom{2j+\ell}{j} \tag{C.16}$$

$$= 2(\ell+1)(-\gamma/2)^\ell \sum_{j=0}^{\infty} (-\gamma/2)^{2j} \frac{2j+\ell+1}{\ell+1} \binom{2j+\ell}{j}, \tag{C.17}$$

where we've factored out the zeroth order term antcipiating its representation as a hypergeometric series. To that end we take the ratio of successive terms

$$\begin{aligned} \frac{(k+1)^{\text{th}} \text{ term}}{k^{\text{th}} \text{ term}} &= \frac{(-\gamma/2)^{2k+2}}{(-\gamma/2)^{2k}} \frac{2k+\ell+3}{2k+\ell+1} \frac{\binom{2k+\ell+1}{k+1}}{\binom{2k+\ell}{k}} \\ &= \gamma^2 \frac{\left(k+\frac{\ell+3}{2}\right)\left(k+\frac{\ell+2}{2}\right)}{(k+1)(k+\ell+1)} \end{aligned} \tag{C.18}$$

which allows us to write the sum as a hypergeometric function ${}_2F_1(a,b;c;z)$.

$$\breve{\xi}_\ell = 2(\ell+1)(-\gamma/2)^\ell \, {}_2F_1\left(\frac{\ell+2}{2}, \frac{\ell+3}{2}; \ell+1; \gamma^2\right) \tag{C.19}$$

$$\tag{C.20}$$

Noting that the final line has the form ${}_2F_1(a, a+1/2; c; z)$, we can find a closed form solution for all ℓ [114, Eq. 15.9.17]. After further manipulation we obtain

$$\breve{\underline{\xi}}_\ell = 2(-1)^\ell \frac{\left(1+\ell\sqrt{1-\gamma^2}\right)}{(1-\gamma^2)^{3/2}} \left(\frac{1-\sqrt{1-\gamma^2}}{1+\sqrt{1-\gamma^2}}\right)^{\ell/2}. \tag{C.21}$$

The process to find the same kind of expression for $\underline{\Xi}$ is similar but more involved, because the higher number of terms leads us to write it as a sum of hypergeometric functions, and each one must be reduced separately. Alternatively, a computer algebra system such as Mathematica[154] can do the tedious manipulations for you. Using either method the result it

$$\begin{aligned}\breve{\underline{\Xi}}_\ell = (-1)^\ell \frac{1}{3\left(1-\gamma^2\right)^{5/2}} \left(\frac{1-\sqrt{1-\gamma^2}}{1+\sqrt{1-\gamma^2}}\right)^{\ell/2} \times \\ \left[3+3\ell\sqrt{1-\gamma^2} - 3(\ell^2-1)(1-\gamma^2) - 2\ell(\ell^2-1)(1-\gamma^2)^{3/2}\right].\end{aligned} \tag{C.22}$$

From here we make a final notation-simplifying substitution, and use Eq. (C.8) to write ξ_n and Ξ_n, taking care to include the factors of 1/2 that arise from going from the cosine series to the complex exponential one. This yields the forms shown earlier in Chapter 5:

$$\xi_n = (-1)^n(1+ny)\frac{3-y^2}{2y^3}\left(\frac{1-y}{1+y}\right)^{n/2} \tag{5.68}$$

$$\Xi_n = (-1)^n \frac{3-y^2}{12y^5}\left(\frac{1-y}{1+y}\right)^{n/2}\left[3+3ny+3(n^2-1)y^2+2n(n^2-1)y^3\right] \tag{5.69}$$

$$y = \sqrt{1-\gamma^2} \tag{5.70}$$

As a check for the accuracy of the above, explicit cosine integrals were performed using Rubi[155], a rule-based integration system. Terms for $n = 0$ through 32 gave expressions equivalent to the above for both ξ_n and Ξ_n. This required significantly more processing time than evaluating the series expression above.

Appendix D: SetList Feedback

Finer-grained control of an experiment can be achieved by actively responding to measurement taken, for instance, by rerunning a failed point in a scan automatically, or by adjusting some operating parameter during a scan based on the measurement you take. This feedback type system can even be leveraged to create computer-controller optimization routines

We have added this capability to SetList using a JavaScript object notation (JSON)-based interface to a dynamically chosen Transmission Control Protocol (TCP) port. The port is looked up by your client via the NI Service Locator. This interface is available since SetList version v2.0.0[1].

D.1 NI Service Locator

The NI Service Locator is available at port 3580 on any machine with an active LabView installation. Visiting the link `http://localhost:3580/dumpinfo?` takes you to a page listing the services currently being broadcast on the local machine. When SetList is running, it will create a named service "SetList/JSON".

[1]Previously we used a custom protocol over fixed TCP ports to do this. It was too clunky given the existence of standard data exchange formats like JSON, so it has been discontinued. Documentation is still available with the rest of the SetList documentation

The service locator will be informed and the port number will be available at [[http://localhost:3580/SetList/JSON]] on the computer running SetList. Other system should be able to access it from another computer by replacing "localhost" with the Internet Protocol (IP) address of the computer running SetList.

The response should be easily parse-able by whatever software is initiating the feedback. This port is static over individual runs of "SetList.vi", so it is wise to cache it and only look it up at startup or when communication fails.

D.2 Protocol

Once you have the port number, you can initiate a TCP connection with that port on the SetList computer. SetList is expecting a JSON object string preceded by its length in binary. That is four bytes representing the integer number of bytes in the string being sent, followed by the string itself. JSON syntax was chosen because it is both widespread and standardized[156, 157].

When it finishes processing the data you've sent, SetList will send a response (formatted as above) and then close the connection. If more information needs to be sent, open a new connection to the same port.

SetList parses the top level of the JSON object for its "members". It assumes each member's name (The first part of a "name:value" pair) is a string matching to some internal command. The "value" part of the pair is passed to the command as a string. If a matching command is not found, SetList will respond with an error and skip that member.

SetList's response is formatted as a JSON object as well, usually containing an array for responses that are normal and a separate array for errors.

Variable Format

Representing a variable as a JSON object works as follows:

```
{
    "name": <string (required)>,
    "defaultValue": <number>,
    "sequenceFunction": <string>,
    "informIgor": <bool>,
    "sequence": <bool>
}
```

Where:

- All members' names correspond to their function in the SetList Variable manager.
- The "name" member has a *required* string value.
- All other members may be given the value "null" (e.g. "informIgor":null) to indicate the variable should retain the previous (or, if creating a new variable, the default) value.

Variables can also be grouped into "Variable Sets" using JSON arrays:((with optional white space added for legibility))

```
[<variable 1>, <variable 2>, ..., <variable N>]
```

Command Formats

Immediately Apply Variables

This command has SetList update the values of the variables right away, regardless of the status of a running sequence. The format is:

```
"instantVariables":<variable set>
```

where "<variable set>" is a single variable set object as specified above.

Sequence Set Variables

This command has SetList update the values of the variables after the end of the currently-running sequence. SetList maintains an ordered first-in first-out (FIFO) list of variable sets, and applies the next set at the end of a sequence just before re-starting the sequence. The full command JSON is then:

```
"sequenceSets":[
    <variable set 1>,
    <variable set 2>,
    ...,
    <variable set N>
]
```

Where "<variable set i>" is a variable set as defined above.

Mulligans

Mulligans have the simplest format:

```
"mulligan":[<number>,...]
```

where "<number>" is the file number of an element you are trying to mulligan.

SetList will only check if the elements of the array are numbers, not if they are in the history (and thus mulligan-able). It reports the total count of numbers it finds, and sends errors for the non-numbers.

Bibliography

[1] M. H. Anderson, J. R. Ensher, M. R. Matthews, C. E. Wieman, and E. A. Cornell, "Observation of Bose-Einstein Condensation in a Dilute Atomic Vapor", Science **269**, 198 (1995).

[2] E. A. Cornell and C. E. Wieman, "Nobel Lecture: Bose-Einstein Condensation in a Dilute Gas, the First 70 Years and Some Recent Experiments", Reviews of Modern Physics **74**, 875 (2002).

[3] C. J. Pethick and H. Smith, *Bose–Einstein Condensation in Dilute Gases*, 2nd ed. (Cambridge University Press, 2008).

[4] N. D. Mermin and H. Wagner, "Absence of Ferromagnetism or Antiferromagnetism in One- or Two-Dimensional Isotropic Heisenberg Models", Physical Review Letters **17**, 1133 (1966).

[5] V. L. Berenzinskiĭ and A. Y. Blank, "Thermodynamics of Layered Isotropic Magnets at Low Temperatures", Soviet Journal of Experimental and Theoretical Physics **37**, 369 (1973).

[6] S. T. Bramwell and P. C. W. Holdsworth, "Magnetization and Universal Sub-Critical Behaviour in Two-Dimensional XY Magnets", Journal of Physics: Condensed Matter **5**, L53 (1993).

[7] S. T. Bramwell and P. C. W. Holdsworth, "Magnetization: A Characteristic of the Kosterlitz-Thouless-Berezinskii Transition", Physical Review B **49**, 8811 (1994).

[8] Z. Hadzibabic and J. Dalibard, "Two-Dimensional Bose Fluids: An Atomic Physics Perspective", Rivista del Nuovo Cimento **34**, 389 (2011).

[9] Z. Hadzibabic, P. Krüger, M. Cheneau, B. Battelier, and J. Dalibard, "Berezinskii–Kosterlitz–Thouless Crossover in a Trapped Atomic Gas", Nature **441**, 1118 (2006).

[10] M. Mondal, S. Kumar, M. Chand, A. Kamlapure, G. Saraswat, G. Seibold, L. Benfatto, and P. Raychaudhuri, "Role of the Vortex-Core Energy on the Berezinskii-Kosterlitz-Thouless Transition in Thin Films of NbN", Physical Review Letters **107**, 217003 (2011).

[11] T. Plisson, B. Allard, M. Holzmann, G. Salomon, A. Aspect, P. Bouyer, and T. Bourdel, "Coherence Properties of a Two-Dimensional Trapped Bose Gas around the Superfluid Transition", Physical Review A **84**, 061606 (2011).

[12] M. Holzmann, M. Chevallier, and W. Krauth, "Universal Correlations and Coherence in Quasi-Two-Dimensional Trapped Bose Gases", Physical Review A **81**, 043622 (2010).

[13] Z. Hadzibabic, P. Krüger, M. Cheneau, S. P. Rath, and J. Dalibard, "The Trapped Two-Dimensional Bose Gas: From Bose–Einstein Condensation to Berezinskii–Kosterlitz–Thouless Physics", New Journal of Physics **10**, 045006 (2008).

[14] M. C. Beeler, M. E. W. Reed, T. Hong, and S. L. Rolston, "Disorder-Driven Loss of Phase Coherence in a Quasi-2D Cold Atom System", New Journal of Physics **14**, 073024 (2012).

[15] P. Cladé, C. Ryu, A. Ramanathan, K. Helmerson, and W. D. Phillips, "Observation of a 2D Bose Gas: From Thermal to Quasicondensate to Superfluid", Physical Review Letters **102**, 170401 (2009).

[16] T. Yefsah, R. Desbuquois, L. Chomaz, K. J. Günter, and J. Dalibard, "Exploring the Thermodynamics of a Two-Dimensional Bose Gas", Physical Review Letters **107**, 130401 (2011).

[17] I. Bloch, J. Dalibard, and W. Zwerger, "Many-Body Physics with Ultracold Gases", Reviews of Modern Physics **80**, 885 (2008).

[18] C. J. Foot, *Atomic Physics (Oxford Master Series in Physics)* (Oxford University Press, Feb. 2005).

[19] H. J. Metcalf and P. van der Straten, *Laser Cooling and Trapping* (Springer, New York, 1999).

[20] W. D. Phillips, "Nobel Lecture: Laser Cooling and Trapping of Neutral Atoms", Reviews of Modern Physics **70**, 721 (1998).

[21] S. Stenholm, "Laser Cooling and Trapping", European Journal of Physics **9**, 242 (1988).

[22] W. D. Phillips and H. Metcalf, "Laser Deceleration of an Atomic Beam", Physical Review Letters **48**, 596 (1982).

[23] E. L. Raab, M. Prentiss, A. Cable, S. Chu, and D. E. Pritchard, "Trapping of Neutral Sodium Atoms with Radiation Pressure", Physical Review Letters **59**, 2631 (1987).

[24] V. S. Bagnato, G. P. Lafyatis, A. G. Martin, E. L. Raab, R. N. Ahmad-Bitar, and D. E. Pritchard, "Continuous Stopping and Trapping of Neutral Atoms", Physical Review Letters **58**, 2194 (1987).

[25] S. Chu, L. Hollberg, J. E. Bjorkholm, A. Cable, and A. Ashkin, "Three-Dimensional Viscous Confinement and Cooling of Atoms by Resonance Radiation Pressure", Physical Review Letters **55**, 48 (1985).

[26] Y. Castin, H. Wallis, and J. Dalibard, "Limit of Doppler Cooling", JOSA B **6**, 2046 (1989).

[27] S. Stenholm, "The Semiclassical Theory of Laser Cooling", Reviews of Modern Physics **58**, 699 (1986).

[28] J. Dalibard and C. Cohen-Tannoudji, "Laser Cooling below the Doppler Limit by Polarization Gradients: Simple Theoretical Models", JOSA B **6**, 2023 (1989).

[29] P. D. Lett, R. N. Watts, C. I. Westbrook, W. D. Phillips, P. L. Gould, and H. J. Metcalf, "Observation of Atoms Laser Cooled below the Doppler Limit", Physical Review Letters **61**, 169 (1988).

[30] A. L. Migdall, J. V. Prodan, W. D. Phillips, T. H. Bergeman, and H. J. Metcalf, "First Observation of Magnetically Trapped Neutral Atoms", Physical Review Letters **54**, 2596 (1985).

[31] O. J. Luiten, M. W. Reynolds, and J. T. M. Walraven, "Kinetic Theory of the Evaporative Cooling of a Trapped Gas", Physical Review A **53**, 381 (1996).

[32] P. Bouyer, V. Boyer, S. Murdoch, G. Delannoy, Y. Le Coq, A. Aspect, and M. Lécrivain, in *Bose-Einstein Condensates and Atom Lasers*, edited by S. Martellucci, A. N. Chester, A. Aspect, and M. Inguscio (Springer US, Boston, MA, 2002), pp. 165–186.

[33] W. Ketterle and N. J. V. Druten, in *Advances In Atomic, Molecular, and Optical Physics*, Vol. 37, edited by B. Bederson and H. Walther (Academic Press, Jan. 1, 1996), pp. 181–236.

[34] H. F. Hess, "Evaporative Cooling of Magnetically Trapped and Compressed Spin-Polarized Hydrogen", Physical Review B **34**, 3476 (1986).

[35] D. E. Pritchard, "Cooling Neutral Atoms in a Magnetic Trap for Precision Spectroscopy", Physical Review Letters **51**, 1336 (1983).

[36] N. Masuhara, J. M. Doyle, J. C. Sandberg, D. Kleppner, T. J. Greytak, H. F. Hess, and G. P. Kochanski, "Evaporative Cooling of Spin-Polarized Atomic Hydrogen", Physical Review Letters **61**, 935 (1988).

[37] I. D. Setija, H. G. C. Werij, O. J. Luiten, M. W. Reynolds, T. W. Hijmans, and J. T. M. Walraven, "Optical Cooling of Atomic Hydrogen in a Magnetic Trap", Physical Review Letters **70**, 2257 (1993).

[38] T. Kinoshita, T. Wenger, and D. S. Weiss, "All-Optical Bose-Einstein Condensation Using a Compressible Crossed Dipole Trap", Physical Review A **71**, 011602 (2005).

[39] A. J. Olson, R. J. Niffenegger, and Y. P. Chen, "Optimizing the Efficiency of Evaporative Cooling in Optical Dipole Traps", Physical Review A **87**, 053613 (2013).

[40] M. D. Barrett, J. A. Sauer, and M. S. Chapman, "All-Optical Formation of an Atomic Bose-Einstein Condensate", Physical Review Letters **87**, 010404 (2001).

[41] K. M. O'Hara, M. E. Gehm, S. R. Granade, and J. E. Thomas, "Scaling Laws for Evaporative Cooling in Time-Dependent Optical Traps", Physical Review A **64**, 051403 (2001).

[42] S. Chu, J. E. Bjorkholm, A. Ashkin, and A. Cable, "Experimental Observation of Optically Trapped Atoms", Physical Review Letters **57**, 314 (1986).

[43] R. Grimm, M. Weidemüller, and Y. B. Ovchinnikov, in *Advances In Atomic, Molecular, and Optical Physics*, Vol. 42, edited by B. Bederson and H. Walther (Academic Press, Jan. 1, 2000), pp. 95–170.

[44] D. Jaksch, C. Bruder, J. I. Cirac, C. W. Gardiner, and P. Zoller, "Cold Bosonic Atoms in Optical Lattices", Physical Review Letters **81**, 3108 (1998).

[45] D. Jaksch and P. Zoller, "The Cold Atom Hubbard Toolbox", Annals of Physics, Special Issue **315**, 52 (2005).

[46] S. Friebel, C. D'Andrea, J. Walz, M. Weitz, and T. W. Hänsch, "${\mathrm{CO}}_{2}$-Laser Optical Lattice with Cold Rubidium Atoms", Physical Review A **57**, R20 (1998).

[47] P. S. Jessen and I. H. Deutsch, in *Advances In Atomic, Molecular, and Optical Physics*, Vol. 37, edited by B. Bederson and H. Walther (Academic Press, Jan. 1, 1996), pp. 95–138.

[48] D. A. Steck, *Rubidium 87 D Line Data* (Jan. 13, 2015).

[49] M. Gajdacz, P. L. Pedersen, T. Mørch, A. J. Hilliard, J. Arlt, and J. F. Sherson, "Non-Destructive Faraday Imaging of Dynamically Controlled Ultracold Atoms", Review of Scientific Instruments **84**, 083105 (2013).

[50] M. R. Andrews, M.-O. Mewes, N. J. van Druten, D. S. Durfee, D. M. Kurn, and W. Ketterle, "Direct, Nondestructive Observation of a Bose Condensate", Science **273**, 84 (1996).

[51] J. E. Lye, J. J. Hope, and J. D. Close, "Nondestructive Dynamic Detectors for Bose-Einstein Condensates", Physical Review A **67**, 043609 (2003).

[52] L. M. Bennie, P. T. Starkey, M. Jasperse, C. J. Billington, R. P. Anderson, and L. D. Turner, "A Versatile High Resolution Objective for Imaging Quantum Gases", Optics Express **21**, 9011 (2013).

[53] E. E. Edwards, "CONSTRUCTION OF APPARATUS AND FIRST EXPERIMENTS INVESTIGATING DYNAMICS OF BOSE-EINSTEIN CONDENSATES IN DISORDERED OPTICAL LATTICES", PhD thesis (University of Maryland (College Park, Md.), 2009).

[54] J. E. Robinson, "Explorations of Variable Interactions in a Cold Rubidium Rydberg Gas", PhD thesis (University of Maryland (College Park, Md.), 2012).

[55] M. Beeler, "Disordered Ultracold Two-Dimensional Bose Gases", PhD thesis (University of Maryland (College Park, Md.), 2010).

[56] M. E. W. Reed, "An Experimental Realization of a Griffiths Phase in 87Rb in Three Dimensions", PhD thesis (University of Maryland (College Park, Md.), 2017).

[57] V. D. Vaidya, "Degenerate Mixtures of Rubidium and Ytterbium for Engineering Open Quantum Systems", PhD thesis (University of Maryland (College Park, Md.), 2015).

[58] C. D. Herold, "Ultracold Mixtures of Rubidium and Ytterbium for Open Quantum System Engineering", PhD thesis (University of Maryland (College Park, Md.), 2014).

[59] D. S. Barker, "Degenerate Gases of Strontium for Studies of Quantum Magnetism", PhD thesis (University of Maryland (College Park, Md.), 2016).

[60] DSB and Z. Smith, *JQIamo/Bipolar-Mosfet-Board: External Componenets and Bugfixes*, Zenodo, July 20, 2019, `https://zenodo.org/record/3344794` (visited on 07/20/2019).

[61] T. Weber, J. Herbig, M. Mark, H.-C. Nägerl, and R. Grimm, "Bose-Einstein Condensation of Cesium", Science **299**, 232 (2003).

[62] C.-L. Hung, X. Zhang, N. Gemelke, and C. Chin, "Accelerating Evaporative Cooling of Atoms into Bose-Einstein Condensation in Optical Traps", Physical Review A **78**, 011604 (2008).

[63] D. J. Han, M. T. DePue, and D. S. Weiss, "Loading and Compressing Cs Atoms in a Very Far-off-Resonant Light Trap", Physical Review A **63**, 023405 (2001).

[64] S. S. Kondov, W. R. McGehee, J. J. Zirbel, and B. DeMarco, "Three-Dimensional Anderson Localization of Ultracold Matter", Science **334**, 66 (2011).

[65] F. Jendrzejewski, K. Müller, J. Richard, A. Date, T. Plisson, P. Bouyer, A. Aspect, and V. Josse, "Coherent Backscattering of Ultracold Atoms", Physical Review Letters **109**, 195302 (2012).

[66] F. Jendrzejewski, A. Bernard, K. Müller, P. Cheinet, V. Josse, M. Piraud, L. Pezzé, L. Sanchez-Palencia, A. Aspect, and P. Bouyer, "Three-Dimensional Localization of Ultracold Atoms in an Optical Disordered Potential", Nature Physics **8**, 398 (2012).

[67] S. Donadello, S. Serafini, M. Tylutki, L. P. Pitaevskii, F. Dalfovo, G. Lamporesi, and G. Ferrari, "Observation of Solitonic Vortices in Bose-Einstein Condensates", Physical Review Letters **113**, 065302 (2014).

[68] M. Farhadi and O. Mohammed, "Energy Storage Technologies for High-Power Applications", IEEE Transactions on Industry Applications **52**, 1953 (2016).

[69] J. C. Beardsall, C. A. Gould, and M. Al-Tai, "Energy Storage Systems: A Review of the Technology and Its Application in Power Systems", in 2015 50th International Universities Power Engineering Conference (UPEC) (Sept. 2015), pp. 1–6.

[70] M. Ristic, Y. Gryska, J. V. M. McGinley, and V. Yufit, "Supercapacitor Energy Storage for Magnetic Resonance Imaging Systems", IEEE Transactions on Industrial Electronics **61**, 4255 (2014).

[71] M. Inomoto, K. Abe, T. Yamada, A. Kuwahata, S. Kamio, Q. H. Cao, M. Sakumura, N. Suzuki, T. Watanabe, and Y. Ono, "Development of Effective Power Supply Using Electric Double Layer Capacitor for Static Magnetic Field Coils in Fusion Plasma Experiments", Review of Scientific Instruments **82**, 023502 (2011).

[72] F. Jiang, T. Peng, H. Xiao, J. Zhao, Y. Pan, F. Herlach, and L. Li, "Design and Test of a Flat-Top Magnetic Field System Driven by Capacitor Banks", Review of Scientific Instruments **85**, 045106 (2014).

[73] S. S. Gorthi and P. Rastogi, "Fringe Projection Techniques: Whither We Are?", Optics and Lasers in Engineering, Fringe Projection Techniques **48**, 133 (2010).

[74] C. Zuo, S. Feng, L. Huang, T. Tao, W. Yin, and Q. Chen, "Phase Shifting Algorithms for Fringe Projection Profilometry: A Review", Optics and Lasers in Engineering **109**, 23 (2018).

[75] X. Su and W. Chen, "Fourier Transform Profilometry:: A Review", Optics and Lasers in Engineering **35**, 263 (2001).

[76] S. Van der Jeught and J. J. J. Dirckx, "Real-Time Structured Light Profilometry: A Review", Optics and Lasers in Engineering, Digital Optical & Imaging Methods in Structural Mechanics **87**, 18 (2016).

[77] B. Tan, N. R. Sivakumar, and K. Venkatakrishnan, "Direct Grating Writing Using Femtosecond Laser Interference Fringes Formed at the Focal Point", Journal of Optics A: Pure and Applied Optics **7**, 169 (2005).

[78] S. Indrišiūnas, B. Voisiat, M. Gedvilas, and G. Račiukaitis, "Two Complementary Ways of Thin-Metal-Film Patterning Using Laser Beam Interference and Direct Ablation", Journal of Micromechanics and Microengineering **23**, 095034 (2013).

[79] G. M. Burrow and T. K. Gaylord, "Multi-Beam Interference Advances and Applications: Nano-Electronics, Photonic Crystals, Metamaterials, Subwavelength Structures, Optical Trapping, and Biomedical Structures", Micromachines **2**, 221 (2011).

[80] A. Parashar, J. S. Mann, A. Shah, and N. Sivakumar, "Numerical and Experimental Study of Interference Based Micromachining of Stainless Steel", Journal of Laser Micro/Nanoengineering **4**, 124 (2009).

[81] J. L. Ville, T. Bienaimé, R. Saint-Jalm, L. Corman, M. Aidelsburger, L. Chomaz, K. Kleinlein, D. Perconte, S. Nascimbène, J. Dalibard, and J. Beugnon, "Loading and Compression of a Single Two-Dimensional Bose Gas in an Optical Accordion", Physical Review A **95**, 013632 (2017).

[82] T. C. Li, H. Kelkar, D. Medellin, and M. G. Raizen, "Real-Time Control of the Periodicity of a Standing Wave: An Optical Accordion", Optics Express **16**, 5465 (2008).

[83] L. Fallani, C. Fort, J. E. Lye, and M. Inguscio, "Bose-Einstein Condensate in an Optical Lattice with Tunable Spacing: Transport and Static Properties", Optics Express **13**, 4303 (2005).

[84] J. Tao, Y. Wang, Y. He, and S. Wu, "Wavelength-Limited Optical Accordion", Optics Express **26**, 14346 (2018).

[85] R. A. Williams, J. D. Pillet, S. Al-Assam, B. Fletcher, M. Shotter, and C. J. Foot, "Dynamic Optical Lattices: Two-Dimensional Rotating and Accordion Lattices for Ultracold Atoms", Optics Express **16**, 16977 (2008).

[86] S. Al-Assam, R. A. Williams, and C. J. Foot, "Ultracold Atoms in an Optical Lattice with Dynamically Variable Periodicity", Physical Review A **82**, 021604 (2010).

[87] W. S. Bakr, J. I. Gillen, A. Peng, S. Fölling, and M. Greiner, "A Quantum Gas Microscope for Detecting Single Atoms in a Hubbard-Regime Optical Lattice", Nature **462**, 74 (2009).

[88] J. I. Gillen, W. S. Bakr, A. Peng, P. Unterwaditzer, S. Fölling, and M. Greiner, "Two-Dimensional Quantum Gas in a Hybrid Surface Trap", Physical Review A **80**, 021602 (2009).

[89] M. Miranda, A. Nakamoto, Y. Okuyama, A. Noguchi, M. Ueda, and M. Kozuma, "All-Optical Transport and Compression of Ytterbium Atoms into the Surface of a Solid Immersion Lens", Physical Review A **86**, 063615 (2012).

[90] S. Dupont, J. C. Kastelik, and F. Causa, "Wide-Band Acousto-Optic Deflectors with High Efficiency for Visible Range Fringe Pattern Projector", Review of Scientific Instruments **78**, 105102 (2007).

[91] S. Dupont and J. C. Kastelik, "Demonstration of a Tunable Two-Frequency Projected Fringe Pattern with Acousto-Optic Deflectors", Review of Scientific Instruments **79**, 056101 (2008).

[92] S. H. Dupont, J. Kastelik, and M. Pommeray, "Structured Light Fringe Projection Setup Using Optimized Acousto-Optic Deflectors", IEEE/ASME Transactions on Mechatronics **15**, 557 (2010).

[93] E. B. Li, X. Peng, J. Xi, J. F. Chicharo, J. Q. Yao, and D. W. Zhang, "Multi-Frequency and Multiple Phase-Shift Sinusoidal Fringe Projection for 3D Profilometry", Optics Express **13**, 1561 (2005).

[94] E. Li, J. Yao, D. Yu, J. Xi, and J. Chicharo, "Optical Phase Shifting with Acousto-Optic Devices", Optics Letters **30**, 189 (2005).

[95] K.-A. B. Soderberg, N. Gemelke, and C. Chin, "Ultracold Molecules: Vehicles to Scalable Quantum Information Processing", New Journal of Physics **11**, 055022 (2009).

[96] A. Klinger, S. Degenkolb, N. Gemelke, K.-A. Brickman Soderberg, and C. Chin, "Optical Lattices for Atom-Based Quantum Microscopy", Review of Scientific Instruments **81**, 013109 (2010).

[97] T. C. Briles, D. C. Yost, A. Cingöz, J. Ye, and T. R. Schibli, "Simple Piezoelectric-Actuated Mirror with 180 kHz Servo Bandwidth", Optics Express **18**, 9739 (2010).

[98] N. C. Pisenti, A. Restelli, B. J. Reschovsky, D. S. Barker, and G. K. Campbell, "An Ultra-Low Noise, High-Voltage Piezo-Driver", Review of Scientific Instruments **87**, 124702 (2016).

[99] *Igor Pro*, version 6.3, WaveMetrics, June 15, 2015, `https://www.wavemetrics.com/`.

[100] Z. Smith, C. Herold, jqi-sr-lab, J. Tiamsuphat, breschovsky, RbDisorderLab, and N. Pisenti, *JQIamo/SetList: DMD Bugfix, Zenodo DOI*, Zenodo, July 20, 2019, `https://zenodo.org/record/3344809` (visited on 07/20/2019).

[101] *LabVIEW*, National Instruments, `http://www.ni.com`.

[102] *Git*, `https://git-scm.com/`.

[103] D. Pekker, G. Refael, and E. Demler, "Finding the Elusive Sliding Phase in the Superfluid-Normal Phase Transition Smeared by c-Axis Disorder", Physical Review Letters **105**, 085302 (2010).

[104] N. Laflorencie, "Sliding Phase in Randomly Stacked 2d Superfluids/Superconductors", EPL (Europhysics Letters) **99**, 66001 (2012).

[105] P. Mohan, P. M. Goldbart, R. Narayanan, J. Toner, and T. Vojta, "Anomalously Elastic Intermediate Phase in Randomly Layered Superfluids, Superconductors, and Planar Magnets", Physical Review Letters **105**, 085301 (2010).

[106] C. S. O'Hern, T. C. Lubensky, and J. Toner, "Sliding Phases in XY Models, Crystals, and Cationic Lipid-DNA Complexes", Physical Review Letters **83**, 2745 (1999).

[107] R. B. Griffiths, "Nonanalytic Behavior Above the Critical Point in a Random Ising Ferromagnet", Physical Review Letters **23**, 17 (1969).

[108] M. Randeria, J. P. Sethna, and R. G. Palmer, "Low-Frequency Relaxation in Ising Spin-Glasses", Physical Review Letters **54**, 1321 (1985).

[109] A. J. Bray and M. A. Moore, "On the Eigenvalue Spectrum of the Susceptibility Matrix for Random Spin Systems", Journal of Physics C: Solid State Physics **15**, L765 (1982).

[110] A. J. Bray, "Nature of the Griffiths Phase", Physical Review Letters **59**, 586 (1987).

[111] M. E. W. Reed, Z. S. Smith, A. Dewan, and S. L. Rolston, "Griffiths Physics in an Ultracold Bose Gas", Phys. Rev. A **99**, 063611 (2019).

[112] D. T. Colbert and W. H. Miller, "A Novel Discrete Variable Representation for Quantum Mechanical Reactive Scattering via the S-matrix Kohn Method", The Journal of Chemical Physics **96**, 1982 (1992).

[113] G.-W. Li, S.-J. Huang, H.-S. Wu, S. Fang, D.-S. Hong, T. Mohamed, and D.-J. Han, "A Michelson Interferometer for Relative Phase Locking of Optical Beams", Journal of the Physical Society of Japan **77**, 024301 (2008).

[114] "NIST Digital Library of Mathematical Functions", F. W. J. Olver, A. B. Olde Daalhuis, D. W. Lozier, B. I. Schneider, R. F. Boisvert, C. W. Clark, B. R. Miller and B. V. Saunders, eds.

[115] G. H. Wannier, "The Structure of Electronic Excitation Levels in Insulating Crystals", Physical Review **52**, 191 (1937).

[116] W. Kohn, "Analytic Properties of Bloch Waves and Wannier Functions", Physical Review **115**, 809 (1959).

[117] J. D. Cloizeaux, "Orthogonal Orbitals and Generalized Wannier Functions", Physical Review **129**, 554 (1963).

[118] N. Marzari, A. A. Mostofi, J. R. Yates, I. Souza, and D. Vanderbilt, "Maximally Localized Wannier Functions: Theory and Applications", Reviews of Modern Physics **84**, 1419 (2012).

[119] M. Holthaus, "Floquet Engineering with Quasienergy Bands of Periodically Driven Optical Lattices", Journal of Physics B: Atomic, Molecular and Optical Physics **49**, 013001 (2015).

[120] A. Eckardt, "Colloquium: Atomic Quantum Gases in Periodically Driven Optical Lattices", Reviews of Modern Physics **89**, 011004 (2017).

[121] A. Eckardt and M. Holthaus, "Dressed Matter Waves", Journal of Physics: Conference Series **99**, 012007 (2008).

[122] H. Sambe, "Steady States and Quasienergies of a Quantum-Mechanical System in an Oscillating Field", Physical Review A **7**, 2203 (1973).

[123] J. H. Shirley, "Solution of the Schr\"odinger Equation with a Hamiltonian Periodic in Time", Physical Review **138**, B979 (1965).

[124] N. Hale and A. Townsend, "An Algorithm for the Convolution of Legendre Series", SIAM Journal on Scientific Computing **36**, A1207 (2014).

[125] A. M. Rey, G. Pupillo, C. W. Clark, and C. J. Williams, "Ultracold Atoms Confined in an Optical Lattice plus Parabolic Potential: A Closed-Form Approach", Physical Review A **72**, 033616 (2005).

[126] D. Goldberg, "What Every Computer Scientist Should Know About Floating-Point Arithmetic", ACM Comput. Surv. **23**, 5 (1991).

[127] E. Jones, T. Oliphant, P. Peterson, et al., "SciPy: Open Source Scientific Tools for Python", [Online; accessed <today>] (2001).

[128] T. Oliphant, "NumPy: A Guide to NumPy", [Online; accessed <today>] (2006).

[129] S. van der Walt, S. C. Colbert, and G. Varoquaux, "The NumPy Array: A Structure for Efficient Numerical Computation", Computing in Science & Engineering **13**, 22 (2011).

[130] F. Johansson et al., *Mpmath: A Python Library for Arbitrary-Precision Floating-Point Arithmetic (Version 0.18)*, http://mpmath.org/ (Dec. 2013).

[131] O. Tange, "GNU Parallel - The Command-Line Power Tool", ;login: The USENIX Magazine **36**, 42 (2011).

[132] K. W. Madison, M. C. Fischer, R. B. Diener, Q. Niu, and M. G. Raizen, "Dynamical Bloch Band Suppression in an Optical Lattice", Physical Review Letters **81**, 5093 (1998).

[133] S. Greschner, G. Sun, D. Poletti, and L. Santos, "Density-Dependent Synthetic Gauge Fields Using Periodically Modulated Interactions", Physical Review Letters **113**, 215303 (2014).

[134] F. Meinert, M. J. Mark, K. Lauber, A. J. Daley, and H.-C. Nägerl, "Floquet Engineering of Correlated Tunneling in the Bose-Hubbard Model with Ultracold Atoms", Physical Review Letters **116**, 205301 (2016).

[135] Á. Rapp, X. Deng, and L. Santos, "Ultracold Lattice Gases with Periodically Modulated Interactions", Physical Review Letters **109**, 203005 (2012).

[136] J. Billy, V. Josse, Z. Zuo, A. Bernard, B. Hambrecht, P. Lugan, D. Clément, L. Sanchez-Palencia, P. Bouyer, and A. Aspect, "Direct Observation of Anderson Localization of Matter Waves in a Controlled Disorder", Nature **453**, 891 (2008).

[137] B. Allard, T. Plisson, M. Holzmann, G. Salomon, A. Aspect, P. Bouyer, and T. Bourdel, "Effect of Disorder Close to the Superfluid Transition in a Two-Dimensional Bose Gas", Physical Review A **85**, 033602 (2012).

[138] G. Semeghini, M. Landini, P. Castilho, S. Roy, G. Spagnolli, A. Trenkwalder, M. Fattori, M. Inguscio, and G. Modugno, "Measurement of the Mobility Edge for 3D Anderson Localization", Nature Physics **11**, 554 (2015).

[139] C. Meldgin, U. Ray, P. Russ, D. Chen, D. M. Ceperley, and B. DeMarco, "Probing the Bose Glass-Superfluid Transition Using Quantum Quenches of Disorder", Nature Physics **12**, 646 (2016).

[140] B. Deissler, M. Zaccanti, G. Roati, C. D'Errico, M. Fattori, M. Modugno, G. Modugno, and M. Inguscio, "Delocalization of a Disordered Bosonic System by Repulsive Interactions", Nature Physics **6**, 354 (2010).

[141] E. E. Edwards, M. Beeler, T. Hong, and S. L. Rolston, "Adiabaticity and Localization in One-Dimensional Incommensurate Lattices", Physical Review Letters **101**, 260402 (2008).

[142] M. Schreiber, S. S. Hodgman, P. Bordia, H. P. Lüschen, M. H. Fischer, R. Vosk, E. Altman, U. Schneider, and I. Bloch, "Observation of Many-Body Localization of Interacting Fermions in a Quasirandom Optical Lattice", Science **349**, 842 (2015).

[143] B. Gadway, D. Pertot, J. Reeves, M. Vogt, and D. Schneble, "Glassy Behavior in a Binary Atomic Mixture", Physical Review Letters **107**, 145306 (2011).

[144] T. Vojta, "Quantum Griffiths Effects and Smeared Phase Transitions in Metals: Theory and Experiment", Journal of Low Temperature Physics **161**, 299 (2010).

[145] S. Ubaid-Kassis, T. Vojta, and A. Schroeder, "Quantum Griffiths Phase in the Weak Itinerant Ferromagnetic Alloy Ni1-xVx", Physical Review Letters **104**, 066402 (2010).

[146] R. Wang, A. Gebretsadik, S. Ubaid-kassis, A. Schroeder, T. Vojta, P. J. Baker, F. L. Pratt, S. J. Blundell, I. Franke, S. M. Johannes, and K. Page, "Supplemental Material for Quantum Griffiths Phase inside the Ferromagnetic Phase of Ni 1 - x V x", Phys. Rev. Lett. **118**, 10 (2017).

[147] R. Desbuquois, L. Chomaz, T. Yefsah, J. Léonard, J. Beugnon, C. Weitenberg, and J. Dalibard, "Superfluid Behaviour of a Two-Dimensional Bose Gas", Nature Physics **8**, 645 (2012).

[148] L. Mathey, A. Vishwanath, and E. Altman, "Noise Correlations in Low-Dimensional Systems of Ultracold Atoms", Physical Review A - Atomic, Molecular, and Optical Physics **79**, 013609 (2009).

[149] Y. .-.-J. Lin, A. R. Perry, R. L. Compton, I. B. Spielman, and J. V. Porto, "Rapid Production of $\hat{\}$\{87\}$Rb BECs in a Combined Magnetic and Optical Potential", Physical Review A **79**, 063631 (2009).

[150] Y. Castin and R. Dum, "Bose-Einstein Condensates in Time Dependent Traps", Physical Review Letters **77**, 5315 (1996).

[151] B. Fang, A. Johnson, T. Roscilde, and I. Bouchoule, "Momentum-Space Correlations of a One-Dimensional Bose Gas", Physical Review Letters **116**, 050402 (2016).

[152] S. Filling, F. Gerbier, A. Widera, O. Mandel, T. Gericke, and I. Bloch, "Spatial Quantum Noise Interferometry in Expanding Ultracold Atom Clouds", EQEC '05. European Quantum Electronics Conference, 2005. **2005**, 232 (2005).

[153] I. B. Spielman, W. D. Phillips, and J. V. Porto, "Mott-Insulator Transition in a Two-Dimensional Atomic Bose Gas", Physical Review Letters **98**, 080404 (2007).

[154] *Mathematica, Version 12.0*, Champaign, IL, 2019, Wolfram Research, Inc., `http://www.wolfram.com/mathematica/`.

[155] A. Rich, P. Scheibe, and N. Abbasi, "Rule-Based Integration: An Extensive System of Symbolic Integration Rules", Journal of Open Source Software **3**, 1073 (2018).

[156] T. Bray, *The JavaScript Object Notation (JSON) Data Interchange Format*, STD 90 (RFC Editor, Dec. 2017).

[157] *The JSON Data Interchange Syntax*, Standard 404 (ECMA International, Dec. 2017).